

ABSTRACT

Title of Document: **MODELING OF WATER-BREATHING
PROPULSION SYSTEMS UTILIZING THE
ALUMINUM-SEAWATER REACTION AND
SOLID-OXIDE FUEL CELLS**

Daniel Francis Waters, Master of Science, 2011

Directed By: Associate Professor Christopher Cadou
Department of Aerospace Engineering

This thesis investigates the use of solid oxide fuel cells (SOFCs) to consume waste hydrogen and improve the overall performance of a Hybrid Aluminum Combustor (HAC): a novel underwater power system based on the exothermic reaction of aluminum with seawater. The system is modeled using a NASA-developed framework called Numerical Propulsion System Simulation (NPSS) by assembling thermodynamic models developed for each component. Results show that incorporating the SOFC is not beneficial in cases where venting hydrogen overboard is permissible. However, when venting hydrogen is not permissible – which is the situation for most missions – the HAC-SOFC provides a 5 to 7 fold increase in range/endurance compared to equivalent battery powered systems. The utility of NPSS was demonstrated for evaluating and optimizing underwater propulsion system performance. Methodologies for predicting how system volume and mass scale with power were also developed to enable prediction of power and energy density.

Report Documentation Page			Form Approved OMB No. 0704-0188	
Public reporting burden for the collection of information is estimated to average 1 hour per response, including the time for reviewing instructions, searching existing data sources, gathering and maintaining the data needed, and completing and reviewing the collection of information. Send comments regarding this burden estimate or any other aspect of this collection of information, including suggestions for reducing this burden, to Washington Headquarters Services, Directorate for Information Operations and Reports, 1215 Jefferson Davis Highway, Suite 1204, Arlington VA 22202-4302. Respondents should be aware that notwithstanding any other provision of law, no person shall be subject to a penalty for failing to comply with a collection of information if it does not display a currently valid OMB control number.				
1. REPORT DATE 2011	2. REPORT TYPE		3. DATES COVERED 00-00-2011 to 00-00-2011	
4. TITLE AND SUBTITLE Modeling of Water-breathing Propulsion Systems Utilizing the Aluminum-seawater Reaction and Solid-oxide Fuel Cells			5a. CONTRACT NUMBER	
			5b. GRANT NUMBER	
			5c. PROGRAM ELEMENT NUMBER	
6. AUTHOR(S)			5d. PROJECT NUMBER	
			5e. TASK NUMBER	
			5f. WORK UNIT NUMBER	
7. PERFORMING ORGANIZATION NAME(S) AND ADDRESS(ES) University of Maryland, College Park, College Park, MD, 20742			8. PERFORMING ORGANIZATION REPORT NUMBER	
9. SPONSORING/MONITORING AGENCY NAME(S) AND ADDRESS(ES)			10. SPONSOR/MONITOR'S ACRONYM(S)	
			11. SPONSOR/MONITOR'S REPORT NUMBER(S)	
12. DISTRIBUTION/AVAILABILITY STATEMENT Approved for public release; distribution unlimited				
13. SUPPLEMENTARY NOTES				
14. ABSTRACT This thesis investigates the use of solid oxide fuel cells (SOFCs) to consume waste hydrogen and improve the overall performance of a Hybrid Aluminum Combustor (HAC): a novel underwater power system based on the exothermic reaction of aluminum with seawater. The system is modeled using a NASA-developed framework called Numerical Propulsion System Simulation (NPSS) by assembling thermodynamic models developed for each component. Results show that incorporating the SOFC is not beneficial in cases where venting hydrogen overboard is permissible. However, when venting hydrogen is not permissible ??? which is the situation for most missions ??? the HAC-SOFC provides a 5 to 7 fold increase in range/endurance compared to equivalent battery powered systems. The utility of NPSS was demonstrated for evaluating and optimizing underwater propulsion system performance. Methodologies for predicting how system volume and mass scale with power were also developed to enable prediction of power and energy density.				
15. SUBJECT TERMS				
16. SECURITY CLASSIFICATION OF:			17. LIMITATION OF ABSTRACT Same as Report (SAR)	18. NUMBER OF PAGES 158
a. REPORT unclassified	b. ABSTRACT unclassified	c. THIS PAGE unclassified		

MODELING OF WATER-BREATHING PROPULSION SYSTEMS UTILIZING
THE ALUMINUM-SEAWATER REACTION AND SOLID-OXIDE FUEL CELLS

By

Daniel Francis Waters

Thesis submitted to the Faculty of the Graduate School of the
University of Maryland, College Park, in partial fulfillment
of the requirements for the degree of
Master of Science
2011

Advisory Committee:
Associate Professor Christopher Cadou, Chair
Associate Professor Gregory Jackson
Associate Professor Kenneth Yu

© Copyright by
Daniel Francis Waters
2011

Dedication

To my mother, without whom none of this is possible.

To my grandfather, whose constant support and boundless enthusiasm are sorely missed.

Acknowledgements

I would first and foremost like to thank Annie, for keeping me focused, keeping me sane, and making me smile even through the most hectic of times.

Thank you to Maria Medeiros and the Office of Naval Research for supporting this work. Also thanks to Dr. Joe Fontaine and the Naval Undersea Warfare Center for their help and guidance.

I would like to thank my advisor, Dr. Cadou. Thank you for having the confidence to let me forge my own path, but still being there to guide me when needed.

Thank you to Dr. Jackson, for your guidance and insight into the world of fuel cells.

Last but not least, I would like to thank my friends and colleagues in the lab. Thank you to Shyam, Anand, and Kiran for helping me learn the ropes, and thank you to Jeff, Daanish, and Jon for keeping the lab a fun place to be even in the midst of a construction zone.

Table of Contents

Dedication	ii
Acknowledgements	iii
Table of Contents	iv
List of Tables	vii
List of Figures	viii
Nomenclature	x
Chapter 1: Introduction	1
1.1 Motivation	1
1.1.1 Applications	1
1.1.2 Range and Endurance	3
1.1.3 Detectability	5
1.2 Existing UUV Power/Energy Options	7
1.2.1 Otto Fuel	7
1.2.2 Batteries	7
1.3 Aluminum Fuel	8
1.3.1 Benefits	8
1.3.2 Challenges	11
1.4 Aluminum Combustion Based Propulsion	12
1.4.1 Hybrid Aluminum Combustor	12
1.4.2 HAC, Solid Oxide Fuel Cell Hybrid	14
1.5 Fuel Cells	15
1.5.1 Principles of Operation	15
1.5.2 Benefits	17
1.5.3 Challenges	18
1.5.4 Solid-Oxide Fuel Cell	20
1.6 Numerical Propulsion System Simulation	21
1.6.1 Overview	21
1.6.2 Solution Method	22
1.6.3 Challenges	23
1.7 Objectives and Approach	24
Chapter 2: Component Models	27
2.1 Component Modeling in NPSS	27
2.2 Standard NPSS Components	28
2.2.1 Bleed Element – Normal Operation	28
2.2.2 Bleed Element – Combustor Operation	29
2.2.3 Bleed Element – Condenser Operation	30
2.2.4 Flow End Element	31
2.2.5 Heat Exchanger Element	31
2.2.6 Splitter Element	33
2.2.7 Shaft Element	33
2.2.8 Turbine Element	34
2.3 Customized Components	35

2.3.1 Compressor Element.....	35
2.3.2 Flow Copy Element	38
2.3.3 Flow Start Element	39
2.3.4 Fuel Seeder Element	40
2.3.5 Liquid Pump Element	41
2.3.6 Loop Start Element	42
2.3.7 Mixture Start Element.....	44
2.3.8 Separator Element.....	45
2.3.9 Solid-Oxide Fuel Cell Element.....	48
2.3.10 Water Mixer Element.....	55
Chapter 3: System Models	56
3.1 System Modeling in NPSS.....	56
3.2 Hybrid Aluminum Combustor Model.....	57
3.3 HAC-SOFC Model	59
3.4 Aluminum-H ₂ O ₂ Combustor Model	61
3.5 Hydrocarbon Fueled Combustor Model	63
Chapter 4: Analysis Methods.....	66
4.1 Scaling Methodology	66
4.1.1 Challenges and Objectives.....	66
4.1.2 HAC Scaling	67
4.1.3 SOFC Scaling.....	73
4.2 Performance Metrics	74
4.2.1 Power, Mass, Volume	74
4.2.2 Reactant Storage	75
4.2.3 Energy Density.....	76
Chapter 5: Model Performance Results	78
5.1 Objectives	78
5.2 HAC System Performance.....	78
5.3 HAC-SOFC Performance	82
5.3.1 Importance of Current Density	82
5.3.2 Effects of H ₂ Utilization.....	85
5.3.3 Cost of H ₂ Venting.....	89
5.3.4 Cost of H ₂ Storage	90
5.3.5 Effect of Water-to-Fuel Ratio	92
5.3.6 Effect of Depth.....	94
5.3.7 Effect of Turbine Pressure Ratio.....	95
5.3.8 Effect of Power Requirement.....	97
5.3.9 Effects of Component Performance Improvements.....	98
5.3.10 Effect of SOFC Scaling	101
5.3.11 Effects of Heat Rejection During Compression.....	102
5.3.12 Combined Performance Improvement.....	103
5.4 Aluminum-H ₂ O ₂ Combustor Performance	105
5.5 Hydrocarbon Fueled Combustor Performance	106
5.6 Performance Comparison.....	106
Chapter 6: Conclusions and Future Work.....	109
6.1 Conclusions.....	109

6.2 Future Work	112
Appendix A: Fuel Energy Content Calculations	114
Appendix B: Heat Exchanger Scaling Calculations	116
Appendix C: NPSS Details of HAC Model.....	118
Appendix D: NPSS Details of HAC-SOFC Model	124
Appendix E: NPSS Details of Aluminum-H ₂ O ₂ Combustor Model.....	131
Appendix F: NPSS Details of Hydrocarbon Combustor Model.....	137
Bibliography	143

List of Tables

Table 1-1: Mission requirements.	2
Table 1-2: Energy content for various undersea propulsion fuels.	9
Table 1-3: Energy content for various fuel cell fuel-oxidizer combinations.	17
Table 2-1: Fuel cell model parameters (Adapted from [32] [33]).	54
Table 4-1: Components with reference mass flow and volume fraction.	72
Table 4-2: Sample calculation of scaling.	73
Table 5-1: Baseline v. improvements comparison.	104
Table C-1: HAC system independent variables.	121
Table C-2: HAC system dependent conditions.	122
Table D-1: HAC-SOFC system independent variables.	128
Table D-2: HAC-SOFC system dependent conditions.	129
Table E-1: Aluminum-H ₂ O ₂ Combustor system independent variables.	134
Table E-2: Aluminum-H ₂ O ₂ Combustor system dependent conditions.	135
Table F-1: Hydrocarbon Fueled Combustor system independent variables.	140
Table F-2: Hydrocarbon Fueled Combustor system dependent conditions.	141

List of Figures

Figure 1-1: Vehicle endurance v. cruise velocity.	5
Figure 1-2: US Navy Mk48 Torpedo [4].	7
Figure 1-3: US Navy "MARV" battery powered UUV [7].	8
Figure 1-4: Range vs. fuel energy density and conversion efficiency [9].	10
Figure 1-5: Hybrid aluminum combustor system diagram.	12
Figure 1-6: HAC-SOFC hybrid system diagram.	14
Figure 1-7: Basic fuel cell.	15
Figure 1-8: US Navy Seahorse UUV, designed at Penn State ARL.	25
Figure 2-1: Standard Bleed element diagram.	28
Figure 2-2: Combustor Bleed element diagram.	29
Figure 2-3: Condenser Bleed element diagram.	30
Figure 2-4: Flow End element diagram.	31
Figure 2-5: Heat Exchanger element diagram.	31
Figure 2-6: Splitter element diagram.	33
Figure 2-7: Turbine element diagram.	34
Figure 2-8: Compressor element diagram.	35
Figure 2-9: Flow Copy element diagram.	38
Figure 2-10: Flow Start element diagram.	39
Figure 2-11: Fuel Seeder element diagram.	40
Figure 2-12: Liquid Pump element diagram.	41
Figure 2-13: Loop Start element diagram.	42
Figure 2-14: Mixture Start element diagram.	44
Figure 2-15: Separator element diagram.	45
Figure 2-16: SOFC element diagram.	48
Figure 2-17: Water Mixer element diagram.	55
Figure 3-1: NPSS model of HAC system.	58
Figure 3-2: NPSS model of HAC-SOFC system.	60
Figure 3-3: NPSS model of HAC-SOFC system (detail of SOFC).	61
Figure 3-4: NPSS model of Aluminum-H ₂ O ₂ Combustor system.	62
Figure 3-5: NPSS model of Hydrocarbon-H ₂ O ₂ Combustor system.	64
Figure 4-1: Straight-tube, counter-current heat exchanger.	69
Figure 4-2: Heat exchanger effectiveness v. length.	71
Figure 5-1: HAC efficiency v. aluminum flow rate.	79
Figure 5-2: HAC efficiency v. feed water flow rate.	80
Figure 5-3: HAC efficiency v. water/fuel ratio.	81
Figure 5-4: Voltage and power density v. current density (P _{NET} =15 kW, H ₂ ut.=53%)...	83
Figure 5-5: System energy density v. current density.	84
Figure 5-6: Components of power v. current density.	85
Figure 5-7: HAC-SOFC volumetric energy density v. hydrogen utilization.	89

Figure 5-8: HAC-SOFC, with H ₂ venting at 10 ft, components of net power output.	90
Figure 5-9: HAC-SOFC, with H ₂ storage to 1000 psi, variation of net power v. time.....	91
Figure 5-10: Hydrogen storage at 1000 psi volume v. H ₂ utilization.	92
Figure 5-11: Comparison of optimized water-to-fuel ratio to HS value.....	93
Figure 5-12: SOFC operating temperature v. hydrogen utilization.	94
Figure 5-13: Variable vehicle depth, HAC-SOFC energy density.	95
Figure 5-14: Effect of turbine pressure ratio on HAC-SOFC energy density.	96
Figure 5-15: Variable power requirement, HAC-SOFC energy density.	97
Figure 5-16: Improved compressor efficiency, HAC-SOFC energy density.	98
Figure 5-17: Improved turbine efficiency, HAC-SOFC energy density.....	99
Figure 5-18: Improved seed ratio, HAC-SOFC energy density.	100
Figure 5-19: Variable SOFC scaling, HAC-SOFC energy density.	102
Figure 5-20: Adiabatic and isothermal compression, HAC-SOFC energy density.	103
Figure 5-21: Combined improvements, HAC-SOFC energy density.....	104
Figure 5-22: Bar graph of energy density of various technologies.....	107

Nomenclature

A	Area
A_{O2}	Arrhenius pre-exponential
A_{des}	Desorption pre-exponential
A_{CROSS}	Cross sectional area
BPR	Bypass ratio
c_0	Constant
c_p	Specific heat capacity
C	Heat capacity
C_D	Drag coefficient
C_{RATIO}	Ratio of heat capacities in heat exchanger
D	Diameter
$D_{x,y}$	Binary diffusion coefficient
E	Voltage potential
E	Energy
E^*	Apparent activation energy
E_{des}	Desorption activation energy
E_{O2}	Arrhenius activation energy
E_S	Energy stored
ED_V	Volumetric energy density
F	Faraday constant
F_D	Drag force
F_T	Thrust force
g	Acceleration due to gravity
G	Gibbs free energy
h	Specific enthalpy
h	Heat transfer coefficient
H	Enthalpy
ΔH_{FUEL}	Fuel heating value
i	Current density
i^*	Exchange current factor
k_{SEED}	Seeding ratio
L	Length
m, M	Mass
MW	Molecular weight
n	Polytropic exponent
n	Molar quantity
N	Number, quantity
P	Power
P_{PL}	Payload power
P_T	Total pressure
PR	Pressure ratio
Q	Heat
R	Gas constant

R	Resistance
$t, \Delta t$	Time
T_T	Total temperature
v	Velocity
v_C	Cruise velocity
V	Volume
W	Work
X	Species molar fraction
Y	Species mass fraction
α	Symmetry factor
γ	Ratio of specific heats
γ_0	Sticking probability
Γ	Surface site density
ε	Heat exchanger effectiveness
η	Overpotential
η	Efficiency
η_0	Overall thermodynamic efficiency
η_S	Isentropic efficiency
η_{isoth}	Isothermal efficiency
μ	Chemical potential
ρ	Density
σ	Conductivity
τ	Tortuosity
φ	Porosity

Chapter 1: Introduction

1.1 Motivation

1.1.1 Applications

The United States Navy has a growing need for the capabilities provided by advanced Unmanned Underwater Vehicles (UUVs) that enable the Navy to complete critical missions while keeping sailors out of harm's way. In 2004, the US Navy released the UUV Master Plan (UUVMP) - a review of the requirements and recommendations for UUV technology advancement in the near and long term [1]. The UUVMP identified nine missions for which UUVs could assist in accomplishing key naval goals. These missions are:

1. Intelligence, Surveillance, and Reconnaissance (ISR)
2. Mine Countermeasures (MCM)
3. Anti-Submarine Warfare (ASW)
4. Inspection and Identification
5. Oceanography
6. Communication and Navigation Network Nodes (CN3)
7. Payload Delivery
8. Information Operations (IO)
9. Time Critical Strike (TCS)

Of these nine missions, items one through five were additionally identified as being best performed by a UUV, meaning that beginning or increasing the use of UUVs in these areas can fundamentally improve the Navy's capacity to achieve success in those missions.

All of these missions require, in some combination, the attributes of long range/endurance, powerful sensor arrays, and minimum detectability (i.e. stealth). This can be summarized in Table 1-1 below.

Table 1-1: Mission requirements.

	Range	Endurance	Sensors	Stealth
Intelligence, Surveillance, and Reconnaissance (ISR)	X	X	X	X
Mine Countermeasures (MCM)		X	X	X
Anti-Submarine Warfare (ASW)		X	X	X
Inspection and Identification	X	X	X	X
Oceanography		X	X	

The UUVMP also identifies four classes of vehicles to satisfy these missions. Matching the appropriate class of vehicle to the mission will improve success rates and reduce overall costs. The four proposed size classes are:

- Man-Portable class: 3-9 inch diameter, 25-100 pounds, 10-20 hours endurance
- Light Weight Vehicle (LWV) class: 12.75 inch diameter, ~500 pounds, 20-40 hours endurance
- Heavy Weight Vehicle (HWV) class: 21 inch diameter, ~3000 pounds, 40-80 hours endurance
- Large Vehicle class: >36 inch diameter, ~20,000 pounds

The larger vehicles have greater capabilities, of course, but will not always be the appropriate match in terms of cost, precision, and ease of deployment. Also, the order of magnitude size differences between the different vehicle classes will often require the use of different types of energy and propulsion sections.

1.1.2 Range and Endurance

Range and endurance were identified in the previous section as important performance parameters for virtually any UUV mission. For the simplified case of a mission with a constant cruise velocity, v_C , expressions for range and endurance can be derived explicitly.

Range can most generally be described as the integral of velocity with respect to time, as shown in Eq. 1-1. The trivial solution to this integral (Eq. 1-2) for constant cruise velocity merely reveals that the range is the product of cruise velocity (v_C) and mission duration ($\Delta t = \text{endurance}$).

$$Range = \int_t^{t+\Delta t} v \cdot dt \quad (1-1)$$

$$Range = \int_t^{t+\Delta t} v_C \cdot dt = v_C \cdot \Delta t \quad (1-2)$$

Because both range and endurance are unknown, more information is needed in order to solve Eq. 1-2. This additional information is obtained by considering the energy expended (i.e. work required) by the vehicle to overcome drag during the mission [2] and to supply power to the payload. The propulsive force, F_{Thrust} , of the vehicle is assumed to be equal to the drag force, F_D (Eq. 1-3). Therefore, the energy expended to propel the vehicle is equal to the integral of payload power plus propulsive power (expressed in terms of the propulsive force F_{Thrust}) with respect to time over the duration of the mission (Eq. 1-4). This energy will be equal to the total usable energy stored in the vehicle, E_S , which is the product of the total chemical energy and the cycle conversion efficiency (Eqs. 1-5 and 1-6).

$$F_{Thrust} = F_D = \left(\frac{1}{2}\rho_{seawater}v^2\right) \cdot C_D \cdot A_{cross} \quad (1-3)$$

$$E_{PL+Thrust} = \int_t^{t+\Delta t} (P_{PL} + F_D \cdot v) \cdot dt = \left[P_{PL} + \left(\frac{1}{2}\rho_{seawater}v_C^3\right) \cdot (C_D A_{cross}) \right] \cdot \Delta t \quad (1-4)$$

$$E_{PL+Thrust} = E_S = (\eta_0 \cdot \Delta H_{V,reactants}) \cdot V_{reactants} \quad (1-5)$$

$$\left[P_{PL} + \left(\frac{1}{2}\rho_{seawater}v_C^3\right) \cdot (C_D A_{cross}) \right] \cdot \Delta t = (\eta_0 \cdot \Delta H_{V,reactants}) \cdot V_{reactants} \quad (1-6)$$

Combining equations 1-2 and 1-6 and rearranging terms gives the following expressions for vehicle range and endurance respectively:

$$Range = \frac{\eta_0 \cdot \Delta H_{V,reactants} \cdot V_{reactants}}{\left(\frac{P_{PL}}{v_C}\right) + \left(\frac{1}{2}\rho_{seawater}v_C^2\right) \cdot (C_D A_{cross})} \quad (1-7)$$

$$Endurance = \Delta t = \frac{\eta_0 \cdot \Delta H_{V,reactants} \cdot V_{reactants}}{P_{PL} + \left(\frac{1}{2}\rho_{seawater}v_C^3\right) \cdot (C_D A_{cross})} \quad (1-8)$$

Equations 1-7 and 1-8 reveal that the range and endurance are proportional to the vehicle's energy storage capacity, E_S . When the total volume of the vehicle's energy section is held constant, the range and endurance are proportional to the volumetric energy density. Therefore, volumetric energy density is an important metric of energy section¹ performance. This is further discussed in Section "4.2.3 Energy Density".

Figure 1-1 is a notional plot of vehicle endurance and range as functions of cruise velocity when all other parameters are held constant. As shown in Figure 1-1, endurance is maximized when velocity is zero, as all power can be dedicated solely to the payload. Endurance drops off as velocity increases and more power is consumed to overcome

¹ The energy section is the vehicle section reserved for fuel storage and propulsion system hardware.

drag. The impact of this on range is reflected in the figure. At very low velocities, the vehicle travels for a long time but at insufficient speed to achieve a large range. At very high velocities, the energy required to overcome drag is so large that propellant is consumed so quickly that not much distance is covered. Between these extremes is an optimum cruise velocity which maximizes vehicle range.

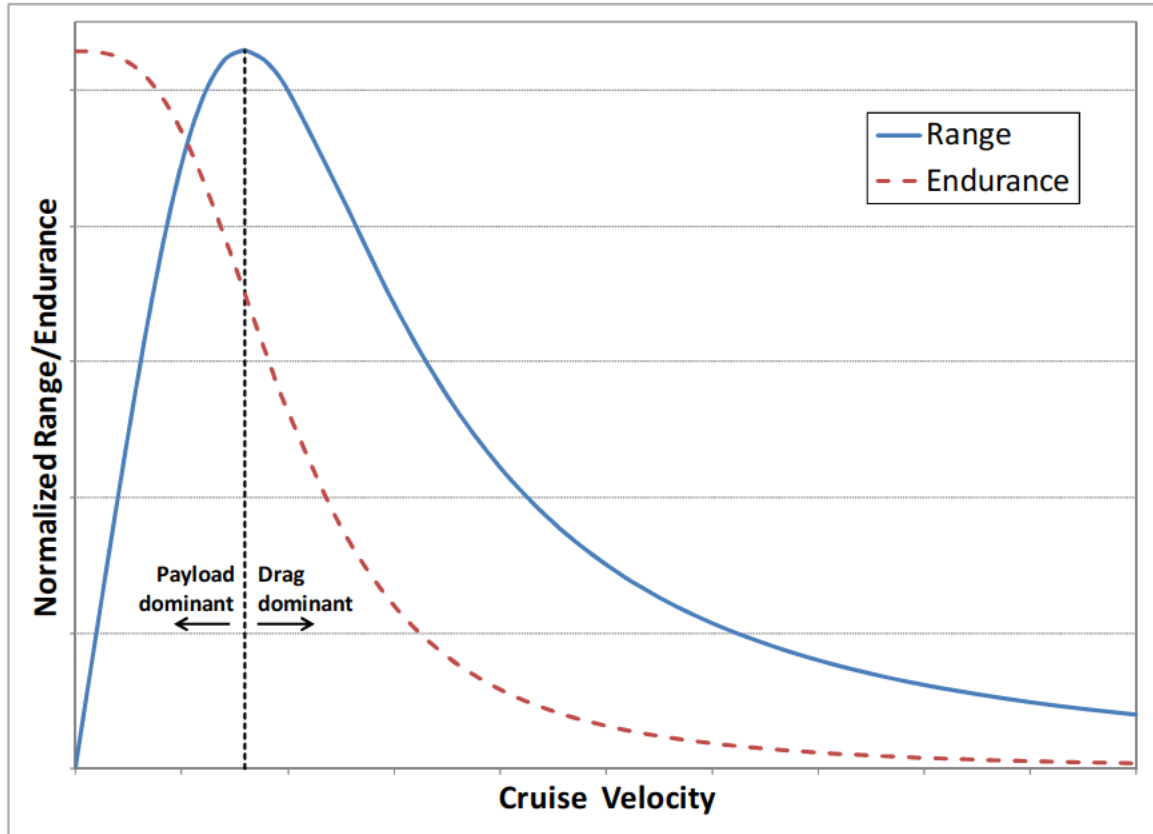


Figure 1-1: Vehicle endurance v. cruise velocity.

1.1.3 Detectability

As stated previously, maintaining low vehicle detectability is often critical to mission success. Detectability is far more difficult to quantify than endurance and range. Many factors contribute to a vehicle's ability to avoid detection including its acoustic, magnetic, electric, and pressure signatures [1]. Generally speaking, a vehicle can also be detected

by its external reflective properties (radar cross-section) and any physical/chemical trails left behind. Radar signatures are mostly irrelevant for UUVs, because they only come to the surface between missions.

Noise generation (acoustic signature) is unavoidable in conventional propeller-driven undersea vehicles. It is reduced through careful hydrodynamic design, but it cannot be eliminated completely. Engine noise depends strongly on the type of propulsion system. For example, a combustion based system will be inherently much louder than a battery powered system. A battery system itself delivers power without making any noise at all, although an electric motor driven by a battery will generate some level of noise.

Combustion engines have turbulent flows, rapidly moving parts, flames, and detonations that all contribute to high noise levels. A loud system will make the vehicle easier to detect and, and this must always be weighed against the other advantages and disadvantages of a given propulsion system – especially since many Navy missions require stealth.

Any vehicle seeking to avoid detection must minimize the physical “tracks” it leaves behind. Any visible trail left by the vehicle would of course be a significant liability. For undersea vehicles, this primarily concerns any buoyant waste products vented or dumped from the vehicle which rise to the surface leaving an easily traceable path. Gaseous waste is particularly detrimental as a large wake of bubbles (as seen with torpedoes) instantly betrays the vehicle’s location. Non-visible chemical trails are also a concern because they could be detected (either submerged or at the surface) and used to track the vehicle.

1.2 Existing UUV Power/Energy Options

1.2.1 Otto Fuel

At present, the Navy primarily utilizes two forms of underwater propulsion. The first is torpedo-borne, Otto fuel driven heat engines. Otto fuel is a relatively stable liquid monopropellant which rapidly decomposes into hot gaseous products when ignited [3].



Figure 1-2: US Navy Mk48 Torpedo [4].

US Navy torpedoes such as the Mk48 (Figure 1-2) utilize piston engines driven by Otto fuel. These systems are not highly efficient but have the advantage of delivering the very high power requirements demanded of modern weapon systems. They have the additional advantage of being based on well established piston engine technology. One major drawback of the torpedo systems is the open cycle design results in an easily identifiable trail of gaseous products. While well suited to torpedo applications, Otto fuel piston engines appear to be a poor fit for the UUV fleet at large.

1.2.2 Batteries

Batteries are primarily relied on for UUVs other than torpedoes [1]. The battery systems have the dual role of driving electric motors for propulsion and providing power to the vehicles' payload. Batteries are better suited than Otto fuel for the typical UUV role of relatively low propulsion power and a significant electrical demand for guidance, sensors,

etc. The primary drawback to battery systems is low energy density. Lithium ion batteries, which are used in the Navy's MARV UUV (Figure 1-3), are expected to deliver on the order of 180 to 315 W-hr/L [5]. The particular alkaline battery system of the Seahorse UUV (Figure 1-8) delivers approximately 120 W-hr/L [6]. These do not compare favorably with expected energy densities from chemical propellants (see Table 1-2 and Table 1-3).

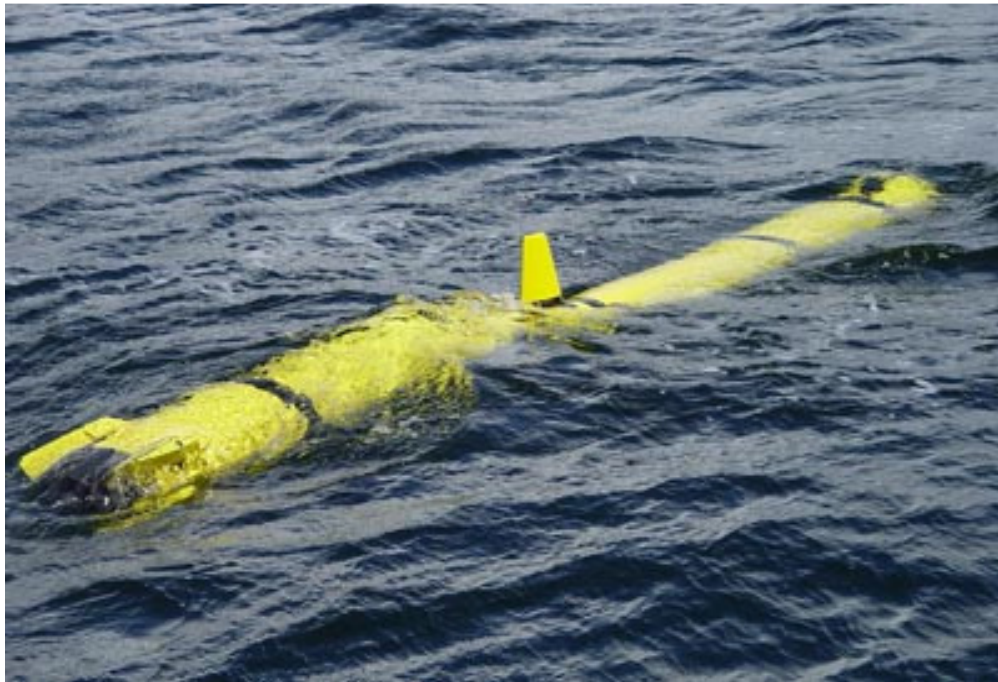
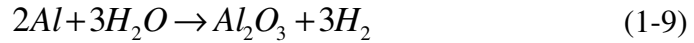


Figure 1-3: US Navy "MARV" battery powered UUV [7].

1.3 Aluminum Fuel

1.3.1 Benefits

It has been well established since as early as 1960 [3] that the most energy dense fuels for undersea propulsion are various metals reacted with seawater to form metal oxides, hydrogen, and heat. Many metals such as aluminum, magnesium, and lithium have highly exothermic reactions with water. The aluminum water reaction equation is:



The ability of a fuel to react with water is desirable in undersea applications because it provides a sort of analog to air-breathing engines where the oxidizer is harvested from the vehicle's surroundings.

Table 1-2: Energy content for various undersea propulsion fuels.

Fuel	Oxidizer	Specific Energy (W-hr/kg)	Energy Density (W-hr/L)
Al	H ₂ O	4212	11374
Zr	H ₂ O	1611	10503
Al	LiClO ₄	3523	8898
Mg	H ₂ O	3609	6273
Li	H ₂ O	7969	4256
Otto fuel [3]		705	895
Li-ion Batteries [5]		90-130	180-315

Table 1-2 summarizes the energy content of various fuel/oxidizer combinations. The method for determining these energy densities is presented in Appendix A. It is important to note that these values do not account for the mass, volume, or efficiency of the power systems needed to convert the fuel to useable work. The list does not contain combinations such as Boron-Water and Beryllium-Water which have high energy content, but are not suitable for reasons of cost and toxicity [8]. The Lithium-Water (Li-H₂O) reaction has the highest specific energy (per unit mass) of those listed, but it does not have the highest energy density (per unit volume) due to the very low density of lithium. Unlike aircraft where weight is the key restriction, UUVs are most strongly constrained by volume. This makes volumetric energy density the most important metric of fuel performance. The volumetric energy density of the aluminum-water (Al-H₂O) reaction is five times greater than Li-H₂O despite Al-H₂O's lower specific energy. Table

1-2 also shows the energy content of Otto fuel and lithium-ion batteries for reference. Both are much lower than the various metal propellants.

Higher fuel energy density generally correlates with improved range and endurance, but the efficiency with which the energy is converted to work is also extremely important. For a fixed fuel volume, the relationship between fuel energy density, efficiency, and range can be easily derived. Figure 1-4 illustrates how energy density and conversion efficiency trade against each-other to affect range. The plot shows that an aluminum fueled system can match the range of a battery system with less than 3% efficiency. A ten-fold increase in range is possible with only 26% efficiency.

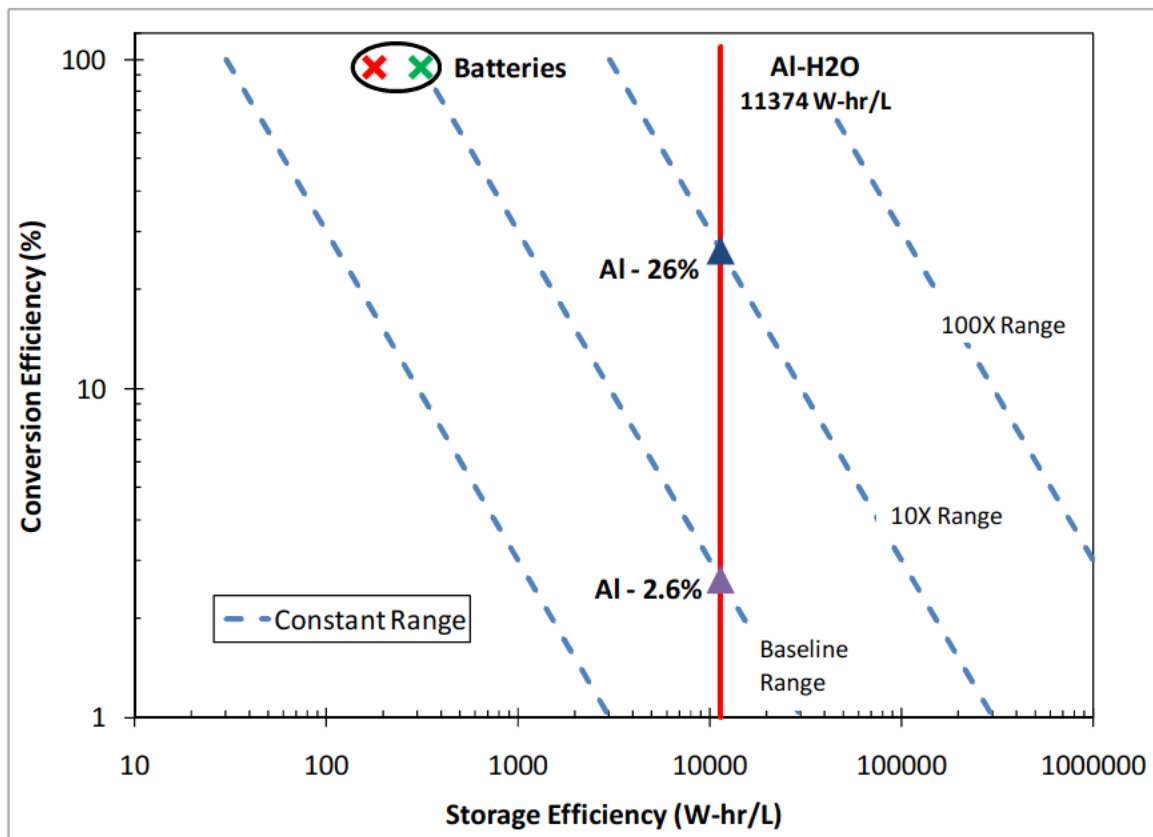


Figure 1-4: Range vs. fuel energy density and conversion efficiency [9].

1.3.2 Challenges

There are many challenges associated with the use of aluminum fuel. The most important are particle injection, ignition, flame stability, and slagging [6]. Early concepts by Greiner [3] for aluminum use in undersea vehicles considered injecting molten aluminum, but that work did not address the considerable challenges associated with operating a molten metal fuel feed system. Startup and shutdown transients would cause particular difficulty as the system attempts to operate at reduced temperatures. Fluidized beds have been studied [10] [11] and shown to be viable delivery systems for powdered propellants but the environment must be carefully controlled to avoid clogging and plugging. Ignition [10], combustion characteristics [12], and reaction thermochemistry [13] of aluminum powders have been studied extensively by a number of researchers.

The formation of liquid and solid aluminum oxide (alumina, Al_2O_3) as a product of aluminum combustion is perhaps the greatest challenge associated with aluminum fuel. If not properly dealt with, molten alumina “slag” will stick to the surfaces of the combustor and piping eventually clogging flow passages. In rocket applications the slag can be carried out by the exhaust and significant impacts on performance are outside the norm [14], but in power cycle applications requiring the hot combustion products to be passed through a turbine, the turbine can be severely damaged by solid slag particles. As a result, Penn State Applied Research Laboratory (ARL) has developed separators capable of removing the vast majority of slag from the flow prior to entering a turbine [6].

1.4 Aluminum Combustion Based Propulsion

1.4.1 Hybrid Aluminum Combustor

The hybrid aluminum combustor (HAC) is an underwater propulsion concept under development by Kiely et al. at Penn State ARL [15] [10]. It was conceived as a way to exploit the aluminum-seawater reaction to increase range and endurance of UUVs. A schematic illustration of this system is shown in Figure 1-5.

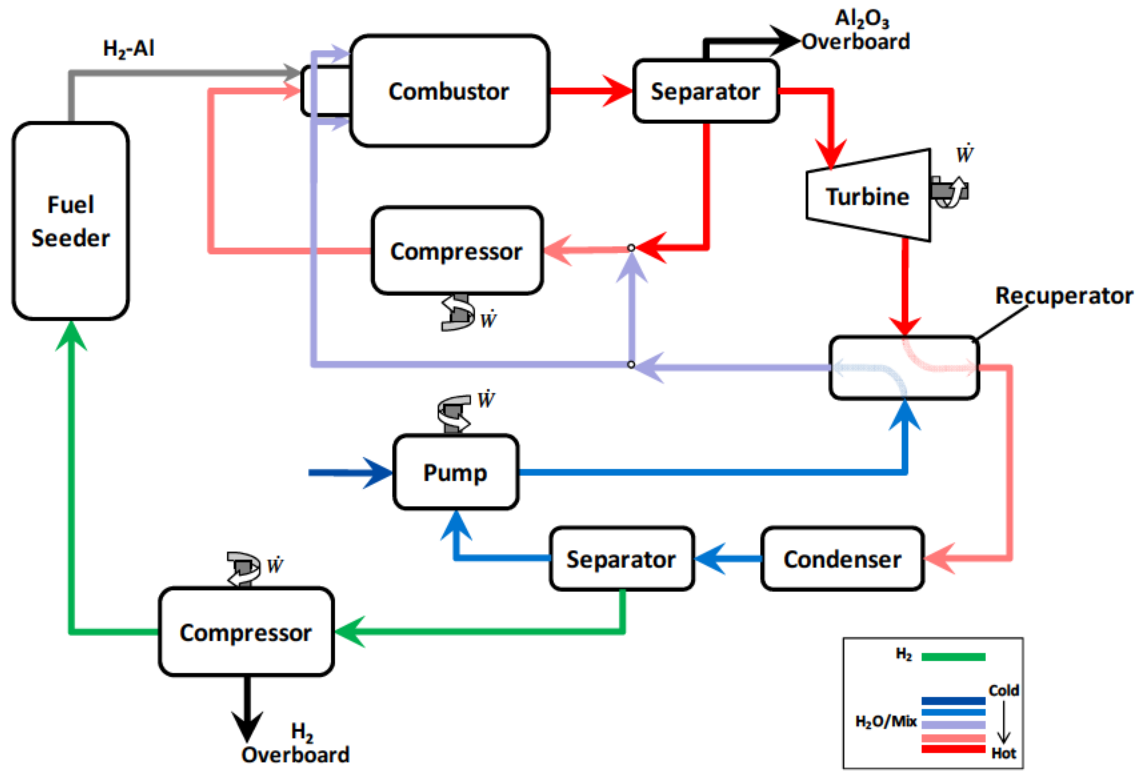


Figure 1-5: Hybrid aluminum combustor system diagram.

The HAC system has been studied by Kiely et al. [10], Hamilton Sundstrand [16], and also by Eagle et al. [9]. It has been shown to have the potential to greatly increase UUV performance. The simulations of Eagle [2] and Eagle et al. [9] demonstrate the system is capable of ten-fold increases in effective reactant energy storage ($\eta_0 \cdot \Delta H_{\text{reactants}}$) over battery technology. These analyses do not address system level energy density.

The operation of the system can be described as follows [2] [9]: The high pressure fuel system, or fuel “seeder”, produces a stream of aluminum powder suspended in a small flow of H_2 which feeds a combustor where it reacts in a near stoichiometric ratio with steam to form aluminum oxide (also known as alumina), more H_2 , and heat. The overall reaction is given in Eq. 1-9. Quenching water is injected around the internal circumference of the combustor to produce large amounts of steam and to solidify the molten alumina before it is able to stick to the walls. The flow then passes through a separator to remove the solidified alumina. The remaining flow is diverted into two streams. A small portion is recirculated to provide the superheated steam that initiates the reaction in the combustor. The remainder of the flow passes through a turbine that extracts mechanical power for the vehicle. The flow exiting the turbine passes through a heat exchanger that pre-warms the quenching water, thus recapturing some enthalpy to improve efficiency. The remaining steam is fully condensed to liquid water and supplemented with sea water to make up for what was consumed by the reaction process. The hydrogen gas is separated from the condensed water, compressed, and reused for aluminum “seeding”. The amount of hydrogen produced is much greater than the amount needed for seeding which means that the remainder must be vented overboard or compressed and stored.

Storing the hydrogen incurs an enormous performance penalty due to the volume required for storage (which displaces reactants) and the work required for compression. Venting the hydrogen overboard is often not acceptable because stealth is important in most underwater missions. Therefore, HAC operation requires a choice between poor

1.5 Fuel Cells

1.5.1 Principles of Operation

A combustion process converts chemical potential energy stored in molecular bonds directly into heat. This is accomplished via exothermic reactions which create relatively low enthalpy products from higher enthalpy reactants [17]. Combustion based power cycles must convert thermal energy into mechanical energy in order to do useful propulsive work. The additional thermal and frictional losses associated with this conversion place strong limitations on performance.

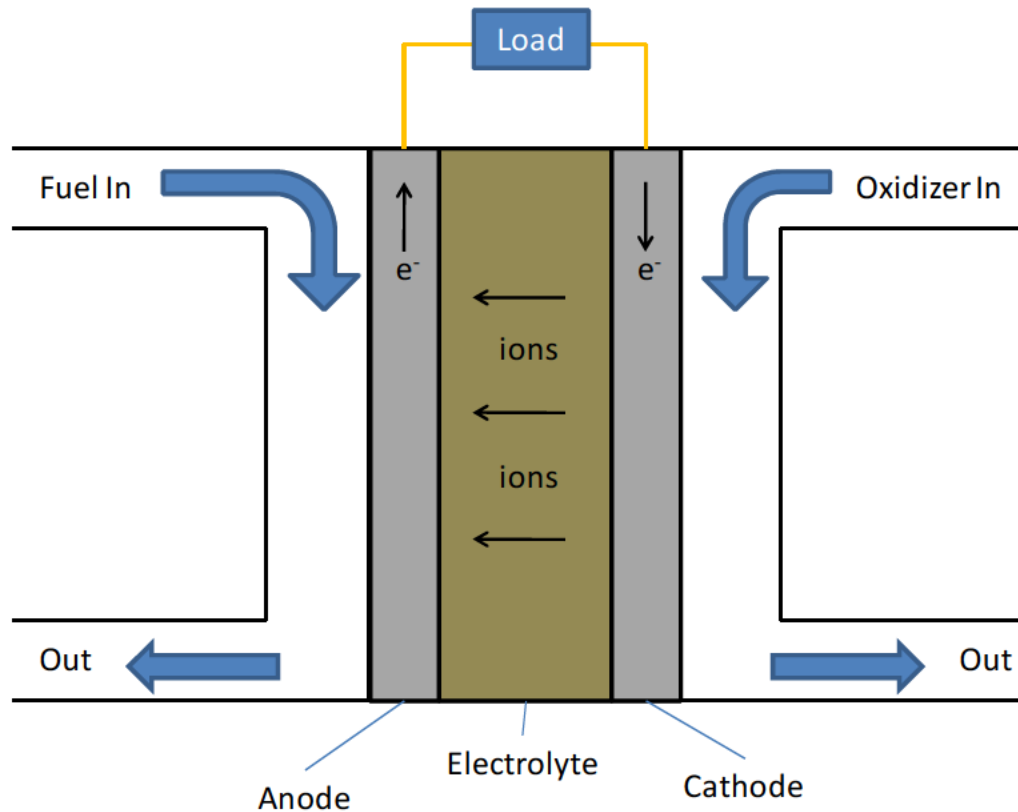
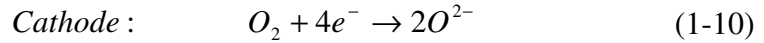


Figure 1-7: Basic fuel cell.

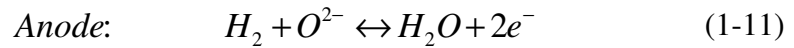
In contrast, fuel cells convert chemical energy directly into electrical energy (along with some heat due to inefficiencies). Figure 1-7 is a schematic illustration of a generic fuel cell. Hydrogen or a hydrogen carrier fuel enters at the anode side and oxidizer enters at

the cathode side. Partial reactions occur at the anode and cathode, and ions are transported across the electrolyte to complete the process. The type of ion varies among fuel cell types. For a PEM fuel cell, protons (H^+) are exchanged whereas for SOFCs it is O^{2-} . Electrons are drawn from the anode to the cathode through a load to produce the useable work of the cell. The overall reaction in a fuel cell is identical to the combustion reaction of the same reactants, and the energy release is likewise a function of the enthalpy difference between reactants and products. The fuel, the oxidizer, and the electrolyte material all vary with fuel cell type and particular application.

Consider for a moment, a solid oxide fuel cell. The following reaction occurs at the cathode [18]:



where e^- denotes an electron. The ionized oxygen diffuses across the electrolyte to the anode. The electrolyte membrane must have very specific properties that enable it to transport O^{2-} ions without transporting the reactant streams or conducting electricity [19]. The reaction at the anode side is given by:



The electrons produced by this reaction are conducted through the load attached to the cell and returned to the cathode. The power produced by the cell is the electron current times the electrical potential across the cell. All chemical potential energy not converted to electricity becomes waste heat.

1.5.2 Benefits

Fuel cells of any number of types have been growing in popularity in recent years as the technologies have developed and become feasible for a wider range of applications. Fuel cells allow the conversion of fuel directly to electrical energy at high efficiencies. For undersea applications, fuel cell systems have obvious appeal because of their quiet operation, easy and fast refueling, and significantly higher energy density than most battery technologies [1].

Table 1-3: Energy content for various fuel cell fuel-oxidizer combinations.

Fuel	Oxidizer	Specific Energy (W-hr/kg)	Energy Density (W-hr/L)
H ₂	O ₂	3728	1535
H ₂	H ₂ O ₂	2280	1551
C _X H _Y	O ₂	2730-2790	2300-2800
C _X H _Y	H ₂ O ₂	1840-1870	2100-2500
NaBH ₄	O ₂	3470	3869
NaBH ₄	H ₂ O ₂	2377	3224
CH ₃ OH	O ₂	2214	2147
Li-ion Batteries		90-130	180-315

Table 1-3 summarizes the energy content of several potential fuel-oxidizer combinations for fuel cells. The methods for determining the energy densities of these propellant combinations are summarized in Appendix A. Air is excluded as an oxidizer because it is not available in the underwater environment. Note that energy density is computed assuming that the H₂ and O₂ are in their liquid states. Therefore they represent upper boundaries on what can be achieved in practice.

It is readily apparent from Table 1-3 that fuel cells use reactant combinations that are often several times more energy dense than batteries. Many fuel cell types are capable of conversion efficiencies near 50% [18]. System level efficiencies are lower, but even at 20-30% overall efficiency, a fuel cell powered UUV might achieve as much as a double or triple the range of conventional battery powered vehicles.

Another advantage of fuel cells is the relative ease of refueling compared to batteries. Battery powered vehicles require extensive downtime between missions to either recharge the batteries or remove and replace them. Fuel cells have storage tanks for oxidizer and fuel that can be refilled easily in the same way that is currently done for conventional engines. Depending on the particular fuel and oxidizer chosen, this could potentially reduce turnaround time from hours to minutes.

1.5.3 Challenges

Despite all the potential benefits, the task of implementing fuel cell technology for vehicle applications is no simple matter. Most challenges in developing effective fuel cell systems are rooted in the very specific physical properties demanded of the anode, cathode, and electrolyte materials [20]. Ideal materials must withstand contamination, repeated duty cycles, potentially large temperature fluctuations, and various physical stresses all without experiencing significant performance degradation. These requirements are in addition to the specific electrochemical, conductive, and diffusive properties demanded of the material in order to function as an electrolyte.

The underwater environment can provide unique challenges for a fuel cell. If either reactant stream is supplied with ambient water from around the vehicle, any number of contamination sources may become a factor. Seawater contains dozens of chemical species, including very high ion content [21]. Chloride ion poisoning has been studied in relation to the presence of HCl in coal syngas [22]. HCl concentrations as low as 20 ppm were shown to degrade SOFC performance. Most other seawater contamination species have not been studied as possible fuel cell contaminants due to the rarity with which such contamination arises in normal applications. Because of the lack of research concerning this topic, the total impact of seawater contamination on fuel cell operation is difficult to predict.

As with any underwater system, a fuel cell must operate without air meaning an oxidizer must be stored. This will incur a penalty relative to a surface based system from an overall system energy/power density viewpoint. However, this does allow for the oxidizer stream content to be more closely controlled, thus avoiding the sometimes unpredictable influence of various air impurities [23].

Material choices vary by fuel cell type. In fact, fuel cells are typically classified by their electrolyte material. Alkaline fuel cells (AFC) are characterized by the alkaline solution which saturates a porous medium to form the electrolyte [24]. Proton exchange membrane fuel cells (PEMFC) utilize an electrolyte membrane permeable to hydrogen ions but not gases [25]. Solid oxide fuel cells (SOFC) employ ceramics such as yttria stabilized zirconia (YSZ) as the porous electrolyte medium to transmit oxygen ions [19].

As a result of their unique compositions and operating conditions, each cell type has its own strengths and limitations.

1.5.4 Solid-Oxide Fuel Cell

As stated above, SOFCs are characterized by the solid oxide ceramic materials used as the electrolyte. The electrolyte must transmit oxygen ions, but have very low permeability to reactant gases and very low electron conductivity. YSZ, the most common SOFC electrolyte, is composed of zirconia (ZrO_2) doped with roughly 8 to 12% by mole of yttrium (Y) [18]. The doping replaces Zr atoms in the crystalline structure with Y atoms, which creates vacancies through which O^{2-} ions may be transmitted [19]. The mechanism by which the ions are moved is only effective at high operating temperatures, and even then the ion conductivity is an order of magnitude smaller than for aqueous electrolytes used in other cell types. The ion conductivity of YSZ is approximately 0.02 S/cm at 800°C and rises to 0.1 S/cm at 1000°C [18]. Because of this, SOFCs must operate at high temperature and the electrolyte layer must be kept as thin as possible.

The cathode material must be porous to allow the diffusion of reactants and must also be a good electron conductor. The material must additionally be resistive to the highly oxidizing cathode environment, which rules out most metals. A common choice for SOFC cathodes is strontium doped lanthanum manganite, a p-type semiconductor [18]. It has the appropriate diffusive and conductive properties, and also acts as a catalyst for the reaction.

The anode material must similarly be porous and conductive, but the catalytic properties must be suitable for the fuel-side reaction. Because the anode environment is not oxidizing, metals and other materials not suitable for the cathode can be used. A popular choice for the anode material is YSZ combined with approximately 35% by volume of nickel [18]. Nickel is an effective reaction catalyst and provides for the conduction of electrons. The YSZ provides the porous structure and allows for a highly stable interface with the YSZ electrolyte [19].

Because many metals have melting points near or below the operating ranges of SOFCs, materials choices are limited. Common conductors aluminum (660°C) and copper (1084°C) [17] will melt if exposed to the temperatures in many SOFCs. Although high operating temperature presents a challenge, it also has its benefits. Carbon monoxide (CO) poisoning, a very common problem in low temperature fuel cells, is not a concern in SOFCs owing to the high temperatures. In contrast, low temperature cells require CO levels below 100 ppm [26] which can be particularly problematic when using hydrocarbon fuels. SOFCs have no such requirement.

1.6 Numerical Propulsion System Simulation

1.6.1 Overview

The analysis of this system is performed using the Numerical Propulsion System Simulation (NPSS) code developed by NASA [27]. This is an extension of earlier work by Eagle [2] toward modeling the base HAC system. The NPSS framework was chosen to evaluate this system because it well suited for analysis of complicated thermodynamic

systems. NPSS allows for the simple linking of various flow components into all sorts of system arrangements. The software comes with many standard components for common devices like turbines, compressors, heat exchangers, etc. The user also has the option of defining any new component that may be desired. Components are easily defined using a C++ based programming language. The NPSS component structure has built in data structures that pass flow information (composition, temperature, pressure, etc.) between linked components. NPSS also has several built-in thermodynamics packages which automatically perform calculations at each flow port. This work utilizes the Chemical Equilibrium with Applications (CEA) [28] thermodynamics package which performs equilibrium calculations at each flow port. The built-in solver converges stable operating points for highly non-linear systems of many linked components.

1.6.2 Solution Method

The NPSS solver allows for user definitions of independent variables and dependent conditions. Any parameter in the system can be defined as an independent variable, under the control of the solver. The solver will adjust the values of the independent variables in order to converge a solution that meets all of the dependent conditions. Dependent conditions are defined as equations that the solver will attempt to satisfy. An NPSS command will require, for example, that the mass of aluminum into the combustor be equal to the mass of steam into the combustor. The number of independents and dependents must be equal.

The solver utilizes a modified Newton-Rhapson method to find converged solutions to the system. Perturbations of the independent variables are used to form the Jacobian matrix in the solution algorithm. The Newton-Rhapson method approximates the correction to each independent variable based on the error in the dependent conditions. The method attempts to drive the residuals to zero. For computational efficiency, a new Jacobian is not formed at every iteration. A new Jacobian is formed only when certain convergence criteria are not met [27]. User controlled variables define the maximum number of iterations or Jacobians to attempt before considering the convergence failed.

1.6.3 Challenges

Solving complex and highly nonlinear systems presents formidable numerical challenges. While CFD solvers regularly handle thousands or even millions of variables simultaneously, the task is greatly facilitated by the similarity of the equations and the sparse nature of the problem [29]. The system of interest here does not have those advantages. Solving it requires simultaneously finding the zero points to 18 dissimilar functions in an 18 dimensional parameter space where the functions are highly nonlinear and strongly dependent on several parameters (i.e. the system is not sparse). This is very challenging computationally and is a research topic in its own right. Therefore, we chose to ‘farm out’ this aspect of the problem so that we could focus on the physics of the modules and the system. The NPSS solver was selected because of its proven track record in solving similar problems involving gas turbine integration. The one issue that is most difficult for the solver to overcome is the need for good initial approximations of the independent variables. Initial conditions that are not adequately close to the converged

solution will lead to divergence. To overcome this challenge, the simulations in this work utilize a single known initial state that produces a converged solution and then gradually vary parameters from the known state, using the most recent converged solution as the new initial condition.

Another key challenge arises from the method of thermodynamic calculations. NPSS supports multiple thermodynamic packages, but one the most suitable for this work involves performing chemical equilibrium (CEA) calculations for each component. This is very useful for calculating the heat release in the combustor. However, chemical equilibrium calculations can result in strong discontinuities in flow states near phase transitions. For example, problems sometimes arise near the condensing point of the steam. Such discontinuities can make convergence impossible, and the issues are sometimes difficult to resolve.

1.7 Objectives and Approach

The objective of this work is to evaluate the use of fuel cells to improve the overall efficiency of the aluminum-sea water combustion system, to provide a method for dealing with the excess hydrogen, and to provide a quieter mode of operation. This will be accomplished by developing a thermodynamic model of the baseline HAC system developed by Penn State and assessing its performance with fuel cell technologies added to it, as illustrated in Figure 1-6. A preliminary model of the HAC system has been developed by Eagle [2] using NASA's Numerical Propulsion System Simulation (NPSS). This earlier model does not account for hydrogen compression, depth effects, or

component scaling. The current work will expand on the existing model by taking these very important factors into account. The addition of component scaling will facilitate a systems level analysis of the problem and allow estimates of energy density which are much more useful than efficiency estimates alone. The HAC model will then be incorporated with a newly developed SOFC model.

The analysis will focus on the design of a power section for a nominal 38 inch diameter UUV. This choice is made to match the work of Penn State ARL [6]. The 38 inch outer diameter hull corresponds to ARL's Seahorse test bed UUV pictured in Figure 1-8.



Figure 1-8: US Navy Seahorse UUV, designed at Penn State ARL.

The analysis assumes an approximately 5 ft long power section with a 36 inch *inner* diameter for this vehicle. This is implemented by performing the design modeling for a 1000 Liter nominal power section (see Eq. 1-12).

$$V_{PWR} = \left(\frac{\pi D_{PWR}^2}{4} \right) \cdot L_{PWR} \approx 1000 L \quad (1-12)$$

The analysis will show the relative improvements in volumetric energy density that are possible from the HAC-SOFC system. The NPSS model is used to estimate pressures, temperatures, and flow rates throughout the system at various operating conditions. It also estimates the power input and output of turbines and compressors, respectively, to find the net system power. The information yielded by the model simulation is used in conjunction with various scaling laws to estimate changes in system mass and volume between operating conditions. This in turn allows the estimation of volumetric energy density, which provides the basis for comparing overall performance.

Chapter 2: Component Models

2.1 Component Modeling in NPSS

The system components were modeled in NPSS using C++ based code. Each component must satisfy the basic conservation equations for mass and energy in addition to any other equations specific to the type of component being modeled. Many models of basic components are included in the NPSS software release. Other components were developed in previous work on the aluminum-water combustion system [2]. The current work uses some of these pre-existing models, builds on and expands others, and develops new component models for additional elements.

The ‘standard’ components described in Section “2.2 Standard NPSS Components” are all included in the NPSS software release. The ten components described in Section “2.3 Customized Components” have all been created or modified specifically for this research. In particular, the ‘Compressor’, ‘Flow Copy’, ‘Liquid Pump’, and ‘Water Mixer’ elements are all original contributions of this research. The ‘Solid-Oxide Fuel Cell’ element is a modified version of an existing model [30] where the mass transport calculations are retained but a far more sophisticated representation of electrochemistry [19] [31] [32] [33] has been incorporated. The ‘Loop Start’ element was developed in earlier work [2], but has been expanded to allow for flows of more than one chemical species. This has greatly improved NPSS’s ability to model complex, recursively dependent systems. Modifications to the ‘Flow Start’, ‘Fuel Seeder’, ‘Mixture Start’, and ‘Separator’ elements have been made but represent only minor improvements over earlier work [2] [30]. More detail on each component is included in the following sections.

2.2 Standard NPSS Components

2.2.1 Bleed Element – Normal Operation

The Bleed element was designed for the separation and reintroduction of bleed flows in gas turbine engines but it is very useful for combining flows of any type because the user can add as many bleed ports as are necessary.

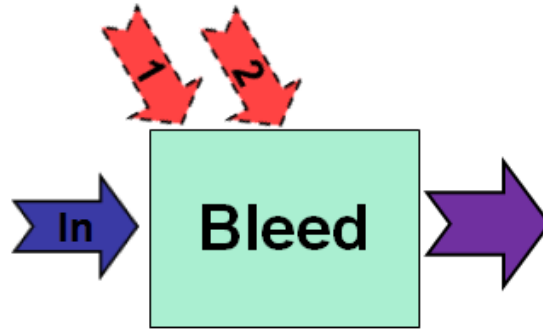


Figure 2-1: Standard Bleed element diagram.

The Bleed element will accept any number of user created bleed ports into the element in addition to the standard fluid inlet and outlet ports. Mass and energy are conserved by requiring that the total mass and enthalpy summed across all inlets to equal the values summed across all outlets. The conservation of energy additionally allows for heat transfer, \dot{Q} , in or out of the component.

$$\sum_i^{N_{IN}} \dot{m}_i = \sum_j^{N_{OUT}} \dot{m}_j \quad (2-1)$$

$$\sum_j^{N_{OUT}} (\dot{m}_j \cdot h_{T,j}) = \sum_i^{N_{IN}} (\dot{m}_i \cdot h_{T,i}) + \dot{Q} \quad (2-2)$$

where N_{IN} and N_{OUT} are the total number of inlets and outlets respectively, and h_T is the total specific enthalpy at the port. A CEA equilibrium calculation is performed to find the temperature and chemical composition of the output flow. The CEA calculation is based on a minimization of Gibbs' free energy. A summary of how this is done and what

equations are involved can be found elsewhere [28]. A constant enthalpy equilibrium calculation is performed using the NPSS command 'setTotal_hp'² at each fluid port.

There are no independent variables, dependent conditions, or input parameters for this element.

2.2.2 Bleed Element – Combustor Operation

The incorporation of chemical equilibrium means that a bleed element can be easily used as a combustor. The standard inlet flow port and one additional bleed port are used to introduce flows of fuel and oxidizer, and the Bleed element performs the necessary calculations to determine the state of the hot products. No modifications to the component are necessary. The implicit assumptions in this use are that the combustor is adiabatic and that the residence time through the combustor is long enough to allow the reaction processes to reach equilibrium. These assumptions should allow close approximations for a well designed combustor

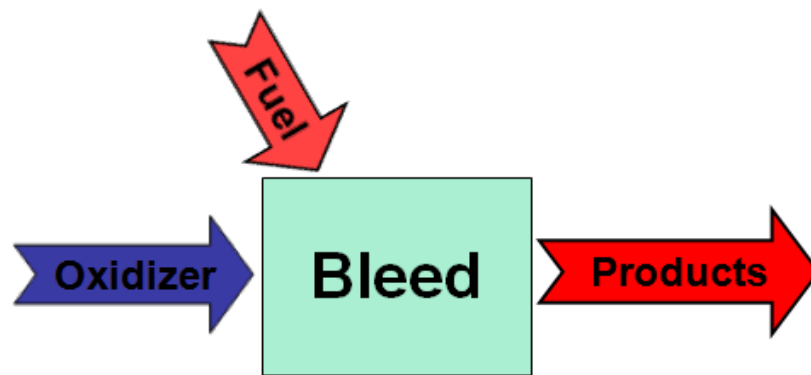


Figure 2-2: Combustor Bleed element diagram.

² setTotal_hp performs a constant enthalpy, constant pressure equilibrium calculation

2.2.3 Bleed Element – Condenser Operation

With only a slight modification, the Bleed element can be used as a simple condenser with a single flow path for heat rejection. NPSS calculates the amount of heat rejected in order to reach a target exit temperature.

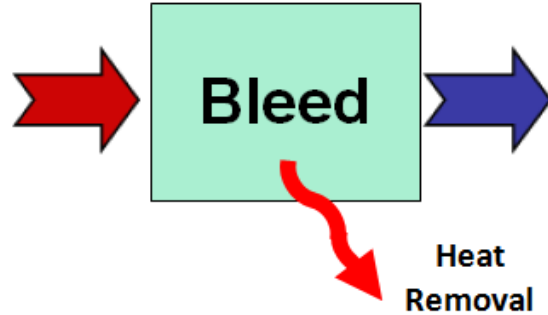


Figure 2-3: Condenser Bleed element diagram.

Any NPSS element can be modified by pre-execute and post-execute commands which are performed each time the element is called along with the standard set of element calculations. Adding a post-execute command enables one to set the Bleed element's flow outlet port to a user-specified input temperature with a user specified pressure drop. The rate of heat rejection is easily determined from the difference in enthalpy between the inlet and outlet ports.

$$T_{T,Out} = T_out \quad (2-3)$$

$$P_{T,Out} = P_{T,Inlet} \cdot (P.R.) \quad (2-4)$$

$$\dot{Q} = \dot{m} \cdot (h_{T,Out} - h_{T,Inlet}) \quad (2-5)$$

where T_out is an input parameter.

Parameters: Outlet temperature, pressure ratio.

2.2.4 Flow End Element

The Flow End element is very simple and only serves to terminate a flow path. Because every fluid port must be linked, the end of a flow path must be connected to a Flow End which has an inlet, but no outlet ports. No calculations are performed by this element.

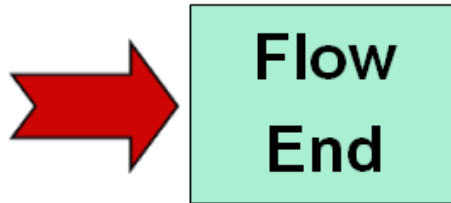


Figure 2-4: Flow End element diagram.

There are no independent variables, dependent conditions, or input parameters for this element.

2.2.5 Heat Exchanger Element

The Heat Exchanger element provides for the transfer of enthalpy between two non-mixing flow paths of different temperature. The element models a countercurrent heat exchanger with a user-defined effectiveness.

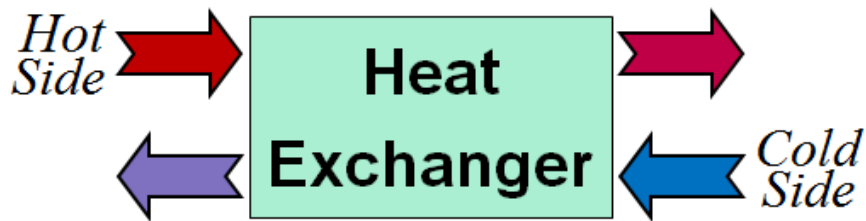


Figure 2-5: Heat Exchanger element diagram.

There is no mass exchange between the hot and cold side flow paths. The pressure drop in each flow path is a user input, and the enthalpy changes in each flow are inferred from energy conservation

$$\dot{m}_{Hot,In} = \dot{m}_{Hot,Out} \quad ; \quad \dot{m}_{Cold,In} = \dot{m}_{Cold,Out} \quad (2-6)$$

$$C_{Hot} = \dot{m}_{Hot} \cdot c_{p,Hot} \quad ; \quad C_{Cold} = \dot{m}_{Cold} \cdot c_{p,Cold} \quad (2-7)$$

$$P_{T,Hot,Out} = P_{T,Hot,Inlet} \cdot (PR_{Hot}) \quad ; \quad P_{T,Cold,Out} = P_{T,Cold,Inlet} \cdot (PR_{Cold}) \quad (2-8)$$

where c_p is the specific heat capacity of the flow, and C is the total heat capacity rate.

The exit temperatures of the two streams depend on whether the hot or cold side flow has a higher heat capacity rate C . If the cold side has higher heat capacity rate, then the hot flow will not have enough energy to raise the cold side exit temperature to the hot side inlet temperature - even if the exchanger effectiveness (ε) is 100%.

If $C_{Cold} > C_{Hot}$:

$$T_{T,Cold,Out} = T_{T,Cold,In} + \varepsilon \cdot (T_{T,Hot,In} - T_{T,Cold,In}) \left(\frac{C_{Hot}}{C_{Cold}} \right) \quad (2-9)$$

Else, if $C_{Hot} > C_{Cold}$:

$$T_{T,Cold,Out} = T_{T,Cold,In} + \varepsilon \cdot (T_{T,Hot,In} - T_{T,Cold,In}) \quad (2-10)$$

The hot side exit temperature is determined by the amount of heat transfer required to achieve the calculated cold side exit temperature. The exit enthalpy of the hot side can therefore be calculated by knowing the total enthalpy change in the cold side.

$$h_{T,Hot,Out} = h_{T,Hot,In} + \left(h_{T,Cold,Out} - h_{T,Cold,In} \right) \left(\frac{\dot{m}_{Cold}}{\dot{m}_{Hot}} \right) \quad (2-11)$$

The hot side exit temperature is determined by calling the 'setTotal_hp' function using the known exit enthalpy and pressure to find equilibrium conditions.

There are no independent variables or dependent conditions for this element.

Parameters: Hot side and cold side pressure ratios, effectiveness.

2.2.6 Splitter Element

The Splitter element allows for a flow to be divided into two different streams. The composition, pressure, and temperature are constant through the element.



Figure 2-6: Splitter element diagram.

The ratio of the exit mass flows is termed the bypass ratio, $BPR = \dot{m}_2 / \dot{m}_1$ and is a parameter that is set by the user. Keeping the pressure, temperature, and composition constant guarantees that energy is conserved in the splitter.

$$\dot{m}_{Inlet} = \dot{m}_{Out,1} + \dot{m}_{Out,2} \quad (2-12)$$

$$\dot{m}_{Out,1} = \frac{\dot{m}_{Inlet}}{1 + BPR} \quad (2-13)$$

There are no independent variables or dependent conditions for this element.

Parameters: Bypass ratio.

2.2.7 Shaft Element

The Shaft element is designed for use with gas turbine engine models and performs many functions that are not utilized in this work. For example, every compressor and turbine element in a gas turbine engine has a shaft output port that must be linked to avoid errors in running NPSS.

There are no independent variables, dependent conditions, or input parameters for this element.

2.2.8 Turbine Element

The Turbine element is used for the expansion of and extraction of work from gaseous flows based on a user input pressure ratio and isentropic efficiency. The element performs a number of calculations designed for use with gas turbine engines which are not utilized in this work.

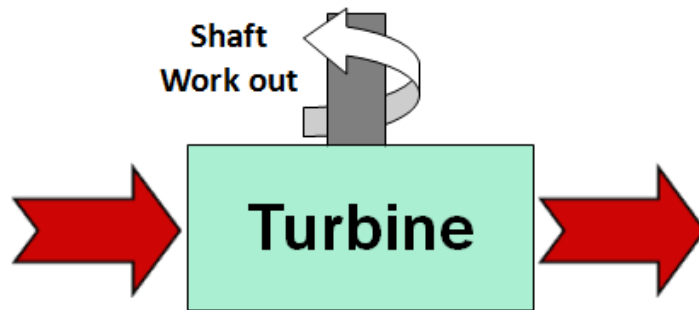


Figure 2-7: Turbine element diagram.

The Turbine element assigns the inlet mass flow and initial composition to the outlet flow and determines the outlet pressure based on the pressure ratio across the turbine which is a parameter. The ideal exit enthalpy based on isentropic conditions, h_s , is determined using the NPSS command 'setTotalSP'³ to determine the conditions in a fluid fixed at the inlet entropy state and at the known exit pressure. The actual exit enthalpy is determined using the definition of the isentropic efficiency [34] which is a parameter. The exit state is defined using the known exit pressure and enthalpy by the NPSS command 'setTotal_hP'.

³ setTotalSP performs a constant entropy, constant pressure equilibrium calculation

$$P_{T,Out} = P_{T,Inlet} / P.R. \quad (2-14)$$

$$h_{T,Out} = h_{T,Inlet} - (h_s - h_{T,Inlet}) \cdot \eta_s \quad (2-15)$$

where η_s is the isentropic efficiency and h_T is the total specific enthalpy. As stated, h_s is determined by equilibrium at known entropy and pressure, and similarly the exit temperature is determined by equilibrium at known enthalpy and pressure.

There are no independent variables or dependent conditions for this element.

Parameters: Pressure ratio, isentropic efficiency.

2.3 Customized Components

2.3.1 Compressor Element

The Compressor element is used for the compression of gaseous flows based on a user-input pressure ratio and efficiency. This element is modeled after the standard NPSS compressor element but has additional modes of operation to simulate isothermal and polytropic compression processes. Much of the standard element's gas turbine-specific functionality has been removed for simplicity.

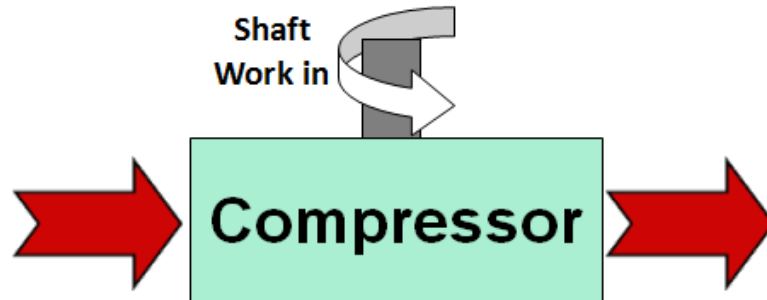


Figure 2-8: Compressor element diagram.

The element assigns the inlet mass flow and composition to the outlet flow and determines the outlet pressure based on the assigned pressure ratio.

$$P_{T,Out} = P_{T,Inlet} \cdot (P.R.) \quad (2-16)$$

“ADIABATIC” Operation:

When the operation mode flag is set to “ADIABATIC”, the ideal exit enthalpy based on isentropic conditions, h_s , is determined using the NPSS command ‘setTotalSP’ to determine the conditions in a fluid with a known inlet entropy state and a known exit pressure. As in the turbine, the actual exit enthalpy is determined using the definition of the isentropic efficiency [34]:

$$h_{T,Out} = \frac{h_s - h_{T,Inlet}}{\eta_s} + h_{T,Inlet} \quad (2-17)$$

where η_s is the isentropic efficiency and h_T is the total specific enthalpy. The exit state is determined from equilibrium at the known exit pressure and enthalpy using the NPSS command ‘setTotal_hP’. As stated, h_s is determined by the known entropy and pressure. The power input to the compressor is calculated using the enthalpy change from inlet to exit:

$$\dot{W} = \dot{m} \cdot (h_{T,Out} - h_{T,Inlet}) \quad (2-18)$$

“ISOTHERMAL” Operation:

When the operation mode flag is set to “ISOTHERMAL”, the element calculates the work input and outlet conditions based on isothermal rather than adiabatic assumptions.

The work required is calculated via the standard equation for isothermal compression [35] and a user-input isothermal compression efficiency:

$$\dot{W} = \frac{1}{\eta_{isoth}} \dot{m} R T_{T,In} \ln \left(\frac{P_{T,Inlet}}{P_{T,Outlet}} \right) \quad (2-19)$$

where R is the specific gas constant and η_{isoth} is the isothermal efficiency. The specific gas constant is determined by dividing the universal gas constant by the molecular weight of the mixture. The latter is given by the NPSS Flowstation variable ‘MW’. The heat rejection during the compression process is calculated as the enthalpy difference between the inlet and outlet streams minus the compression work:

$$\dot{Q} = \dot{m} \cdot (h_{T,Out} - h_{T,Inlet}) - \dot{W} \quad (2-20)$$

“POLYTROPIC” Operation:

When the operation mode flag is set to “POLYTROPIC”, the element calculates the work input and outlet conditions based on the assumption that pressure and volume obey the following relation [34] where n does not necessarily equal the specific heat ratio γ :

$$P \cdot V^n = \text{Constant} = P_{In} \cdot V_{In}^n \quad (2-21)$$

This leads to the following relationship between temperature and pressure ratio for an ideal gas:

$$T_{T,Out} = T_{T,In} \cdot \left(\frac{P_{T,Out}}{P_{T,Inlet}} \right)^{\frac{n-1}{n}} \quad (2-22)$$

The exit state is set in NPSS using the ‘setTotalTP’ function. The compression work associated with a polytropic process with efficiency, η_{poly} is given by [34]:

$$\dot{W} = -\frac{1}{\eta_{poly}} \left(\frac{n}{n-1} \right) \cdot \dot{m} R T_{T,In} \left(\frac{P_{T,Out}}{P_{T,Inlet}} \right)^{\frac{n-1}{n}} \quad (2-23)$$

The heat rejection during the compression process is calculated as the enthalpy difference between the inlet and outlet streams minus the compression work.

There are no independent variables or dependent conditions for this element.

Parameters: Pressure ratio, efficiency, operation mode flag, polytropic exponent.

2.3.2 Flow Copy Element

The Flow Copy element was developed for the current work as a means for analytical comparison of parallel flow processes. This is not a physical component in the system, and it explicitly does not conserve mass and energy. The element outputs two copies of the inlet stream by assigning all inlet properties (mass flow, composition, pressure, temperature, etc.) to both outlet streams. .

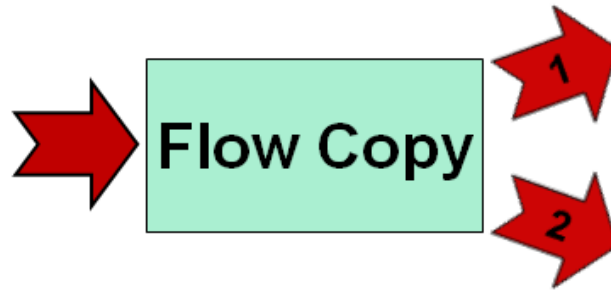


Figure 2-9: Flow Copy element diagram.

The primary purpose of this element is to create identical flows that can be used to compare alternate flow processes. This work uses it to compare the work required for different compression processes.

There are no independent variables, dependent conditions, or input parameters for this element.

2.3.3 Flow Start Element

NPSS comes packaged with a Flow Start element, but the standard element is tailored for gas turbine engines and is not easily adapted to flows of hydrogen, steam, and others. For this reason, a modified Flow Start element was developed (based closely on an NPSS model developed at UC-Irvine [30]) that easily accepts any specified species as an assigned parameter.

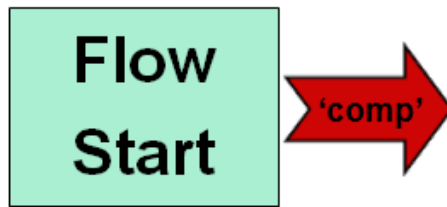


Figure 2-10: Flow Start element diagram.

The element initiates a stream by assigning mass flow, temperature, and pressure to it.

The outlet stream is a pure species, designated as the string parameter 'comp' (abbreviated from composition).

There are no independent variables or dependent conditions for this element.

Parameters: Outlet temperature, pressure, mass flow rate, and flow composition.

2.3.4 Fuel Seeder Element

The Fuel Seeder element was developed for the earlier work on the base system [2]. The element simulates the fluidized flow of aluminum powder suspended in hydrogen gas that feeds fuel to the combustor.

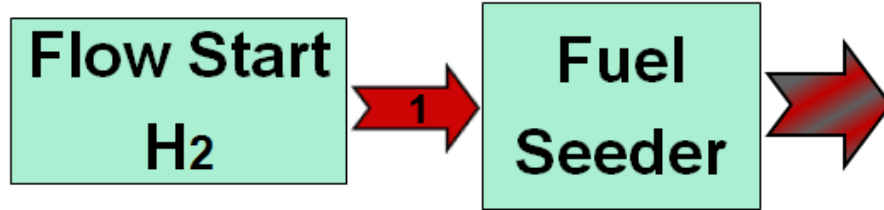


Figure 2-11: Fuel Seeder element diagram.

The Seeder element is ‘hard coded’ to add a specified flow of aluminum to the fluidization gas (H_2) and the physical process by which the metal powder becomes entrained in the flow is not modeled. The losses associated with this process are represented by specifying the pressure ratio across the Seeder. The degree of entrainment is specified using the entrainment ratio k_{seed} .

$$\dot{m}_{AL,Out} = k_{seed} \cdot \dot{m}_{Inlet} \quad (2-24)$$

$$\dot{m}_{Out} = (1 + k_{seed}) \cdot \dot{m}_{Inlet} \quad (2-25)$$

$$P_{T,Out} = P_{T,Inlet} \cdot (P.R.) \quad (2-26)$$

The temperature of the component is assumed constant and equal to the temperature of the incoming gas flow. Strictly speaking, mass is not conserved in this component because the mass flow out is greater than the mass flow in. However, this is because aluminum in the real physical fuel seeder being modeled is contained within the seeder and exits as it is entrained in the gas flow.

There are no independent variables or dependent conditions for this element.

Parameters: Entrainment ratio, pressure ratio.

2.3.5 Liquid Pump Element

The Liquid Pump element was developed as a simple way to increase the pressure of a liquid flow with known density. This element is not suitable for flows with a significant fraction of gaseous components. The element allows a simple calculation of the work required to pump a flow of water.

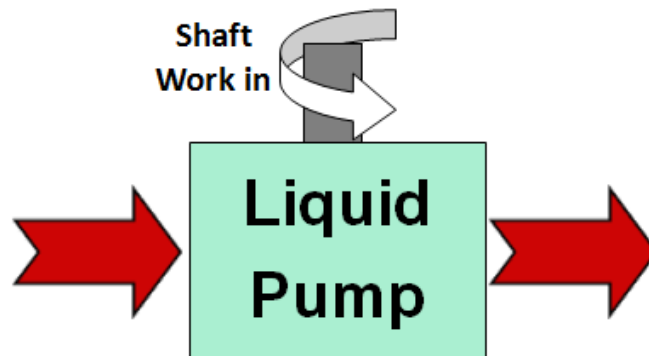


Figure 2-12: Liquid Pump element diagram.

This element uses the simple calculation of pump head to increase the pressure of an incoming stream of liquid flow and calculate the work input required for the process. The temperature is assumed to be constant and the outlet pressure is determined by a user input pressure ratio. The density of the flow is also a user input parameter. While this is a potential source of error, most liquids are virtually incompressible (i.e. they have very large bulk moduli) and this is far preferable to using the NPSS Flowstation value 'rhot' for density which is very sensitive to even trace amounts ($<<1\%$) of gaseous constituents.

$$P_{T,Out} = P_{T,Inlet} \cdot (P.R.) \quad (2-27)$$

$$Head = \frac{P_{T,Out} - P_{T,Inlet}}{\rho \cdot g} \quad (2-28)$$

$$\dot{W} = -\frac{\dot{m} \cdot g \cdot Head}{\eta_{pump}} \quad (2-29)$$

In these expressions, ρ is the density of the liquid, P.R. is the pump pressure ratio, and η_{pump} is the pump efficiency.

There are no independent variables or dependent conditions for this element.

Parameters: Pressure ratio, liquid density, pump efficiency.

2.3.6 Loop Start Element

The Loop Start element was originally developed for the earlier work on the base system [2]. It is required to address difficulties associated with flows that loop through the system (i.e. components that are recursively dependent on their own solutions).

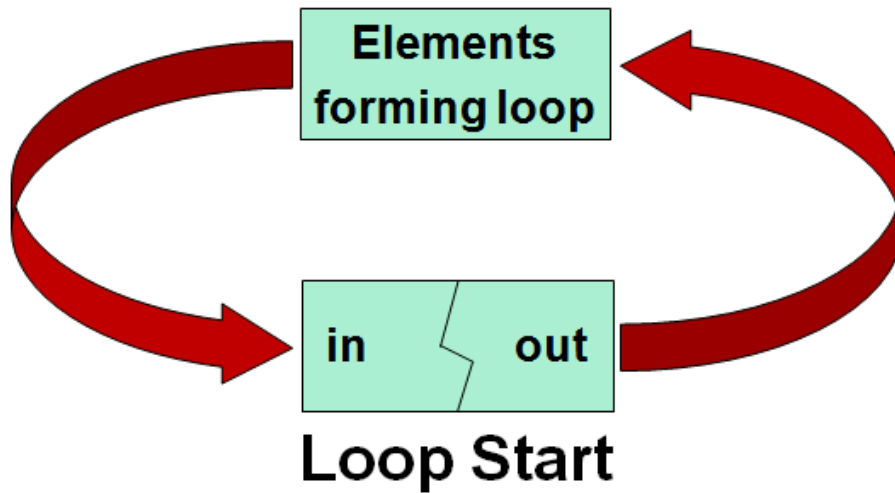


Figure 2-13: Loop Start element diagram.

The original element matched pressure, temperature, and weight flow but assumed a pure species output. The current work has expanded the loop element to also match up to three species' mass fractions in the flow. Unlike a typical element, the Loop Start does not perform operations on the inlet flow and pass the 'updated' flow to the outlet. Rather, the Loop Start acts more like a Flow Start and Flow End with several variables and conditions designed to simulate a simple passage of flow in the converged system. In the converged state, the inlet and outlet conditions are identical. To achieve this, the outlet conditions are treated as independent variables, and matching of the inlet and outlet states constitutes the dependent conditions.

Independents, Dependents, and Parameters:

Independent variables:

- Outlet flow total temperature, $T_{T,Out}$
- Outlet flow total pressure, $P_{T,Out}$
- Outlet mass flow rate, \dot{m}_{Out}
- Outlet species mass fractions
 - $Y_{1,out}$, $Y_{2,out}$, $Y_{3,out}$

Dependent conditions:

- Total temperature, $T_{T,Out} = T_{T,In}$
- Total Pressure, $P_{T,Out} = P_{T,In}$
- Mass flow, $\dot{m}_{Out} = \dot{m}_{In}$
- Species mass fractions
 - $Y_{1,Out} = Y_{1,In}$; $Y_{2,Out} = Y_{2,In}$; $Y_{3,Out} = Y_{3,In}$

The only parameters necessary to define a Flow Loop element are the initial estimates of the six independent variables. Poor estimates may prevent the solver from converging. This is only a slight limitation because the dependent conditions of this element converge relatively easy due to the simple correlation of matching input and output parameters.

2.3.7 Mixture Start Element

The Mixture Start element is partly adapted from similar work at the University of California-Irvine [30]. The element is designed to produce an output mixture stream at a specified temperature and pressure. The outlet flow is created from two inlet streams.

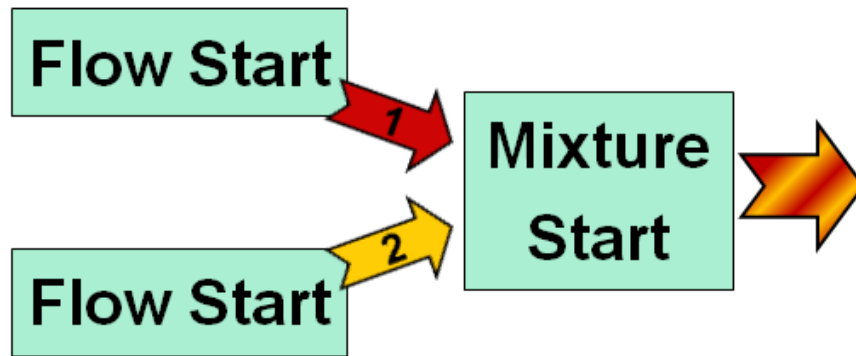


Figure 2-14: Mixture Start element diagram.

Because the temperature and pressure of the mixture are specified, a Mixture Start element is only suitable for starting a known state mixture flow with the two inlet flows coming from Flow Start elements (which produce pure species flows). For example, inlet flows of hydrogen peroxide and water can produce a flow at some desired concentration of an H_2O_2 solution. This element is not appropriate for mixing flows of unknown states because energy conservation will not be satisfied.

The Mixture Start element copies the two inlet flows and sums the mass flows and assures the proper mass fractions in the outlet flow:

$$\dot{m}_{Out} = \dot{m}_{In-1} + \dot{m}_{In-2} \quad (2-30)$$

$$Y_{species,Out} = \frac{Y_{species,In-1} \cdot \dot{m}_{In-1} + Y_{species,In-2} \cdot \dot{m}_{In-2}}{\dot{m}_{Out}} \quad (2-31)$$

There are no independent variables or dependent conditions for this element.

Parameters: Outlet temperature and outlet pressure.

2.3.8 Separator Element

The Separator element was originally developed for the earlier work on the base system [2]. This component divides an incoming mixture stream into two outlet streams of different composition. The degree of separation is determined by the values of the input parameters. In this work, the component is used to divide an incoming stream of steam, hydrogen, and alumina into an alumina stream and a steam/hydrogen stream.



Figure 2-15: Separator element diagram.

The original element was hard coded to accept only flows of steam, hydrogen, and alumina. The element has since been improved and expanded to accept any species specified by the user and to accept up to five different flow species at a time. In addition,

the original element had three outlet streams where the steam/hydrogen stream was split in two. This feature was removed from the model because not every application requires a split stream, and the outlet streams can be further divided by another Splitter element if desired. Overall, these changes have made the Separator element more generally applicable to a variety of situations.

The Separator requires inputs for the five flow species, their molecular weights (needed to calculate the molar flow rate), and the separation efficiency of each species. The separation efficiency is the ratio of the mass flow of the species in the second outlet to the mass flow of that species at the inlet. The user must also specify the pressure ratio across the component.

$$\eta_i = \frac{\dot{m}_{i,Out-2}}{\dot{m}_{i,Inlet}} \quad (2-32)$$

$$P_{T,Out-1} = P_{T,Out-2} = (P.R.) \cdot P_{T,Inlet} \quad (2-33)$$

The work required to separate a flow into its pure species is assumed to be equal to the reversible work of mixing the pure flows [36].

$$W_{Rev} = -R_u T \sum_i n_i \cdot \ln(X_i) \quad (2-34)$$

The subscript i denotes the different species in the mixture. Substituting the molar flow rate, \dot{n} , for the number of moles, n , will yield the work rate for a continuous process.

Because the flows exiting the separator are not completely separated into pure components, the power consumed by the Separator is determined by taking the difference between the power required to completely separate the inlet flow and the power required to completely separate the two outlet flows.

$$\dot{W}_{Separation} = R_u T \left[\left(\sum_i \dot{n}_i \cdot \ln(X_i) \right)_{Inlet} - \left(\sum_i \dot{n}_i \cdot \ln(X_i) \right)_{Outlet-1} - \left(\sum_i \dot{n}_i \cdot \ln(X_i) \right)_{Outlet-2} \right] \quad (2-35)$$

While this represents the ideal, ‘best case’ scenario for the power required, it is the best estimate available that does not require detailed modeling of the particle-laden flow passing through the separator. Implementing such a detailed model would not be practical in the NPSS framework.

Since there is no mechanism in the Separator for adding or removing work externally, the only way to satisfy conservation of energy is to extract the separation work from the flow. Therefore, the enthalpy of the exiting flows must equal the inlet enthalpy less the separation work.

$$(\dot{m} \cdot h)_{Out-1} + (\dot{m} \cdot h)_{Out-2} = (\dot{m} \cdot h)_{Inlet} - \dot{W}_{Separation} \quad (2-36)$$

This is accomplished by setting the two outlet flow temperatures equal to the temperature of the mixture that satisfies this enthalpy condition at the known exit pressure. The relationship between temperature and enthalpy of these complex mixtures is determined by calling CEA using the built in NPSS commands.

There are no independent variables or dependent conditions for this element.

Parameters: Pressure ratio.

Species name, molecular weight, and separation efficiency for each of five species.

2.3.9 Solid-Oxide Fuel Cell Element

A new element was developed to represent the SOFC. The mass transport in the model is based on an existing SOFC element developed at the University of California-Irvine [30]. More sophisticated and accurate models of SOFC electrochemistry have been incorporated based on work done at the University of Maryland and Colorado School of Mines [19] [33] [32].

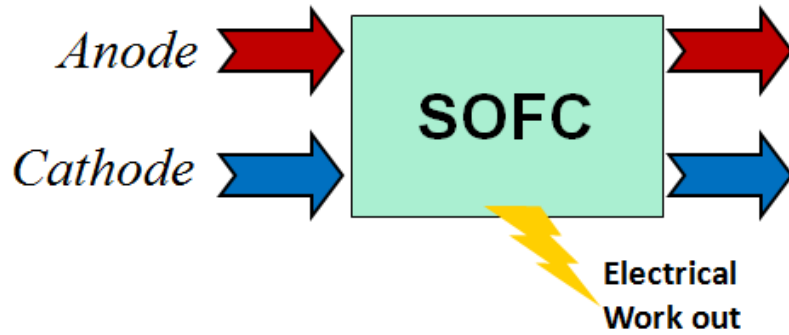


Figure 2-16: SOFC element diagram.

Chemistry, Mass Transfer, and Energy Balance:

The chemistry of the process is represented very simply using an input parameter: H_2 utilization. H_2 utilization is the fraction of the hydrogen gas in the anode flow that is consumed by the chemical reaction. This fraction of H_2 is removed from the anode flow and an equal number of moles of H_2O are added. One half this number of moles of O_2 is removed from the cathode side flow. This assures that elemental hydrogen and oxygen are conserved and that the appropriate chemistry (Eq. 2-36) is modeled.



$$\Delta n_{H_2, anode} = -\Delta n_{H_2O, anode} = \frac{1}{2} \Delta n_{O_2, cathode} \quad (2-38)$$

$$\dot{m}_{out, Anode} = \dot{m}_{in, Anode} - \dot{m}_{H_2, reacted} + \dot{m}_{H_2O, produced} \quad (2-39)$$

$$\dot{m}_{out,Cathode} = \dot{m}_{in,Cathode} - \dot{m}_{O_2,reacted} \quad (2-40)$$

An energy balance is performed to determine the operating temperature of the fuel cell. Temperature is adjusted as an independent variable to satisfy the condition that the difference in enthalpy between the inlet and outlet flows must equal the energy converted to electricity plus the energy lost to the environment via heat transfer. This can be expressed:

$$\dot{W}_{Elec} = (\dot{m}_{out} \cdot H_{out} - \dot{m}_{in} \cdot H_{in}) + \dot{Q} \quad (2-41)$$

In this work \dot{Q} is zero, and the fuel cell is operating adiabatically. The solver converges to the temperature which satisfies Eq. 2-41. Ordinarily this has the effect of raising the cell temperature above ambient except in the case of very large heat losses. An additional assumption is made that the entire fuel cell is operates at uniform temperature, absent any spatial temperature gradients. A higher fidelity model would need to account for local temperature variations within the SOFC, but because both anode and cathode flows will enter the cell hot it is reasonable to assume that temperature gradients will be minimized.

Electrochemistry:

Unless otherwise noted, all equations in this section are referenced from Solid Oxide Fuel Cells Using Syngas by Kee, Zhu, and Jackson [19]. The fuel cell voltage is determined by subtracting several overpotentials from the reversible potential:

$$E_{cell} = E_{rev} - \eta_{ohm} - \eta_{act,a} - \eta_{act,c} - \eta_{conc,a} - \eta_{conc,c} \quad (2-42)$$

The reversible potential is determined using the Nernst equation and the partial pressures in the anode and cathode flows:

$$E_{rev} = -\frac{\Delta G^0}{nF} + \frac{RT}{nF} \ln \left(\frac{P_{H_2,a} \cdot P_{O_2,c}}{P_{H_2O,a}} \right) \quad (2-43)$$

$$\Delta G^0 = \mu_{H_2O,a}^0 - \mu_{H_2,a}^0 - \frac{1}{2} \mu_{O_2,c}^0 \quad (2-44)$$

The standard state change in Gibbs free energy for the reaction (ΔG^0) is determined by computing the change in standard state chemical potentials of each species in the reaction using JANAF polynomials (to account for variations with temperature). The partial pressures of H_2 , O_2 , and H_2O are taken *after* the mass transfer described above (i.e. the pressures are taken at the exit).

The ohmic overpotential accounts for the voltage drop across the cell as a result of electrical resistance:

$$\eta_{ohm} = iR = \frac{iL}{\sigma_0} \quad (2-45)$$

$$\sigma_0 = \frac{\sigma_0^0}{T} \exp \left(\frac{-E_a}{RT} \right) \quad (2-46)$$

where L is the thickness of the electrolyte, i is the current density, and σ_0 is the conductivity of the electrolyte. It increases with temperature due to the exponential term which is also a function of an activation energy parameter, E_a .

The activation overpotentials at the anode and cathode account for the loss of potential resulting from the energy required to initiate chemical reaction at the anode and cathode. The calculation is based on the Butler-Volmer equation. For the anode, this is given by:

$$i = i_{0,a} \left[\exp\left(\frac{\alpha_a F \eta_{act,a}}{RT}\right) - \exp\left(\frac{\alpha_c F \eta_{act,a}}{-RT}\right) \right] \quad (2-47)$$

where i_0 is the exchange current, and α_a and α_c are symmetry parameters. Because there is no closed form expression that enables one to solve for η_{act} directly, the solver varies η_{act} as an independent variable until the equation above is satisfied. Using the methods described by Zhu and Kee [32] and Zhu et al. [33], the anode exchange current is given by:

$$i_{0,a} = i_{H2}^* \frac{\left(\frac{P_{H2}}{P_{H2}^*}\right)^{1/4} (P_{H2O})^{3/4}}{1 + \left(\frac{P_{H2}}{P_{H2}^*}\right)^{1/2}} \quad (2-48)$$

$$P_{H2}^* = \frac{A_{Des} \Gamma^2 \sqrt{2\pi RT W_{H2}}}{\gamma_0} \exp\left(-\frac{E_{des}}{RT}\right) \quad (2-49)$$

$$i_{H2}^* = i_{H2,ref}^* \exp\left[-\frac{E_{H2}}{R} \left(\frac{1}{T} - \frac{1}{T_{ref}}\right)\right] \quad (2-50)$$

where P_{H2}^* is a function of hydrogen adsorption and desorption rates, and A_{Des} , Γ , γ_0 , E_{Des} , $i_{H2,ref}^*$, and E_{H2} are fit parameters. Partial pressures are taken at the anode exit.

Similarly, the activation overpotential at the cathode is found by:

$$i = i_{0,c} \left[\exp\left(\frac{\alpha_a F \eta_{act,c}}{RT}\right) - \exp\left(\frac{\alpha_c F \eta_{act,c}}{-RT}\right) \right] \quad (2-51)$$

$$i_{0,c} = i_{O2}^* \frac{\left(\frac{P_{O2}}{P_{O2}^*}\right)^{1/4}}{1 + \left(\frac{P_{O2}}{P_{O2}^*}\right)^{1/2}} \quad (2-52)$$

$$P_{O_2}^* = A_{O_2} \exp\left(-\frac{E_{O_2}}{RT}\right) \quad (2-53)$$

$$i_{O_2}^* = i_{O_2,ref}^* \exp\left[-\frac{E_{O_2}}{R} \left(\frac{1}{T} - \frac{1}{T_{ref}}\right)\right] \quad (2-54)$$

Partial pressures are taken at the cathode exit.

The concentration overpotentials account for the loss of potential due to depletion of the supply of reactants at the reaction sites: As the reaction proceeds faster (i.e. the current is higher), the reactants are consumed faster than they can be replaced via diffusion. The following equations give concentration overpotentials at the anode and cathode as functions of current and diffusion coefficients:

$$\eta_{conc,a} = -\frac{RT}{2F} \ln \left[\frac{1 - \frac{RT\delta_a i}{2FD_{H_2,eff,a}P_{H_2,a}}}{1 + \frac{RT\delta_a i}{2FD_{H_2O,eff,a}P_{H_2O,a}}} \right] \quad (2-55)$$

$$\eta_{conc,c} = -\frac{RT}{4F} \ln \left[1 - \frac{RT\delta_c i \cdot (1 - X_{O_2,c})}{4FD_{O_2,eff,c}P_{O_2,c}} \right] \quad (2-56)$$

where δ is the thickness of anode or cathode, and $D_{k,eff}$ is the effective diffusion coefficient of species K in the mixture at the anode or cathode. The effective binary diffusion coefficient through the porous anode or cathode is given by Eq. (2-56) as a function of the porosity (ϕ) and tortuosity (τ) of the anode/cathode.

$$D_{KL}^{eff} = \frac{\phi}{\tau} D_{KL} \quad (2-57)$$

While mixture averaged diffusion coefficients can be found using Eq. (2-57), in the present work the anode and cathode flows have two gaseous constituents each so binary

coefficients are sufficient. The temperature and pressure dependence of the binary diffusion coefficients is represented using curve fits to data from Cantera. The method of finding the appropriate diffusion coefficients is taken from Zhu and Kee [31]:

$$D_{K,eff} = \frac{1 - Y_K}{\sum_{L \neq K} \frac{X_L}{D_{KL}^{eff}}} \quad (2-58)$$

Independents, Dependents, and Parameters:

Independent variables:

- Fuel cell temperature, T_{cell}
- Anode activation loss, $\eta_{act,anode}$
- Cathode activation loss, $\eta_{act,cathode}$

Dependent conditions:

- Enthalpy change, conservation of energy

$$\bullet \quad \dot{W}_{Elec} = (\dot{m}_{out} \cdot H_{out} - \dot{m}_{in} \cdot H_{in}) + \dot{Q}$$

- Anode activation

$$\bullet \quad i = i_{0,a} \left[\exp\left(\frac{\alpha_a F \eta_{act,a}}{RT}\right) - \exp\left(\frac{\alpha_c F \eta_{act,a}}{-RT}\right) \right]$$

- Cathode activation

$$\bullet \quad i = i_{0,c} \left[\exp\left(\frac{\alpha_a F \eta_{act,c}}{RT}\right) - \exp\left(\frac{\alpha_c F \eta_{act,c}}{-RT}\right) \right]$$

Table 2-1: Fuel cell model parameters (Adapted from [32] [33]).

Parameter	Symbol	Value	Units
Electrons transferred	n	2	
Gas constant	R	8.314	J/K-mol
Heat transfer rate	\dot{Q}	0	BTU/lb
Binary diffusion coefficient	D_{H_2,H_2O}	.915	cm ² /s
Binary diffusion coefficient	D_{O_2,H_2O}	.282	cm ² /s
Diff. reference temperature	$T_{ref,diff}$	307	K
Electrolyte properties			
Thickness	L_{elec}	30	μm
Ion conductivity	σ_0^0	3.6e5	K/cm-Ω
Activation energy	E_a	80	kJ/mol
Anode properties			
Thickness	δ_a	1800	μm
Porosity	ϕ	0.3	
Tortuosity	τ	6	
Anodic symmetry factor	α_a	1.5	
Cathodic symmetry factor	α_c	.5	
Apparent activation energy	$E_{H_2}^*$	120	kJ/mol
Exchange current factor	$i_{H_2,ref}^*$	4.25	A/cm ²
Reference temperature	$T_{ref,act}$	1073	K
Desorption pre-exponential	A_{des}	5.59e15	m ² /mol-s
Desorption activation energy	E_{des}	88.12	kJ/mol
Surface site density	Γ	2.6e-5	mol/m ²
Sticking probability	γ_0	0.01	
Cathode properties			
Thickness	δ_c	50	μm
Porosity	ϕ	0.3	
Tortuosity	τ	5	
Anodic symmetry factor	α_a	1.5	
Cathodic symmetry factor	α_c	.5	
Apparent activation energy	$E_{O_2}^*$	130	kJ/mol
Exchange current factor	$i_{O_2,ref}^*$	1.2	A/cm ²
Arrhenius activation energy	E_{O_2}	200	kJ/mol
Arrhenius pre-exponential	A_{O_2}	4.9e8	Atm

2.3.10 Water Mixer Element

The Water Mixer element was developed to mix two streams of liquid water. It is only suitable for flows that are nearly pure liquid water and has been developed to circumvent the problems that many standard NPSS components have when dealing with liquid water. For example, a similar mixing of gaseous flows could be handled by a Bleed element, but experience has shown that liquid water often causes those elements to return errors.

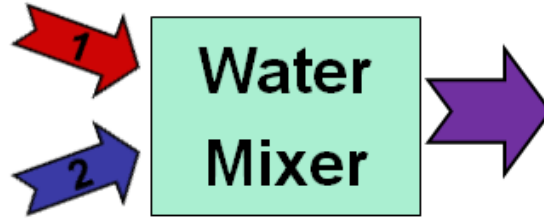


Figure 2-17: Water Mixer element diagram.

The element operates on the basic assumptions that the heat capacity of both inlet flows is constant and the same. This assumption is reasonable for inlet flows at normal liquid water temperatures and composed of greater than 99% liquid water by mass. The particular value of the heat capacity is not important as long as it is the same for the two inlet streams. Based on this assumption, the outlet temperature is determined by performing a weighted average of the inlet stream temperatures.

$$P_{T,Out} = P_{T,Inlet,1} \quad (2-59)$$

$$T_{T,Out} = \frac{T_{T,Inlet,1} \cdot \dot{m}_{Inlet,1} + T_{T,Inlet,2} \cdot \dot{m}_{Inlet,2}}{\dot{m}_{Inlet,1} + \dot{m}_{Inlet,2}} \quad (2-60)$$

$$\dot{m}_{Out} = \dot{m}_{Inlet,1} + \dot{m}_{Inlet,2} \quad (2-61)$$

There are no independent variables, dependent conditions, or input parameters for this element.

Chapter 3: System Models

3.1 System Modeling in NPSS

Using the numerous standard and user-defined elements described in the previous chapter, any number of system models can be created by linking together the proper components. The fluid output port of any component is easily linked to a fluid input port using the NPSS ‘linkPorts’ command. A fluid port is a data structure within a component which stores values for a fully defined flow state. The structure defines mass flow temperature, pressure, enthalpy, entropy, molecular weight, etc. at a given flow location. Linking ports between components is the numerical means by which a fluid stream passes through the system.

The ease of linking components is what makes NPSS a relatively fast and easy environment for developing system models and investigating various systems and configurations. Because NPSS supports a number of thermodynamics packages, each system model must declare which package is to be used for all components. In all of the system modeling presented here, the ‘CEA’ package is used which requires a full chemical equilibrium calculation at each flow location.

NPSS models of four different systems have been developed. The first is the Hybrid Aluminum Combustor system which is an update of earlier work on this problem [2]. The current model is more complete and more fully accounts for the work input required for the pumps and compressors necessary to keep the cycle running. The second model incorporates a solid-oxide fuel cell operating adiabatically downstream of the turbine to

represent a HAC-SOFC hybrid system. The goal is to analyze the effects of the SOFC on the base system and how that translates to vehicle performance. Using this model with the SOFC hydrogen utilization set to 0% is thermodynamically identical to using the base HAC system. The third and fourth systems are presented only for comparison. The third system uses hydrogen peroxide to oxidize the aluminum directly in the combustor. The fourth system uses a liquid hydrocarbon instead of aluminum as the fuel.

3.2 Hybrid Aluminum Combustor Model

The Hybrid Aluminum Combustor (HAC) model is the full system simulation of the base aluminum combusting Rankine cycle system illustrated in Figure 1-5. As stated, this system has been investigated in earlier work [2], but the current iteration fully accounts for water pumps and gas compressors needed to move water and combustion products into and out of the system (which would be operating at some depth below the surface). The NPSS block diagram of the numerical implementation of the system is presented in Figure 3-1.

In the figure, each NPSS component is shown with the element type and element name. Components shown with dashed line boundaries represent ‘non-physical’ NPSS elements, meaning they don’t exist as physical components of the HAC system but they are used in NPSS for this analysis. Elements with input or output shaft work are shown with a rotating shaft symbol, and the condenser is illustrated with heat rejection, \dot{Q} .

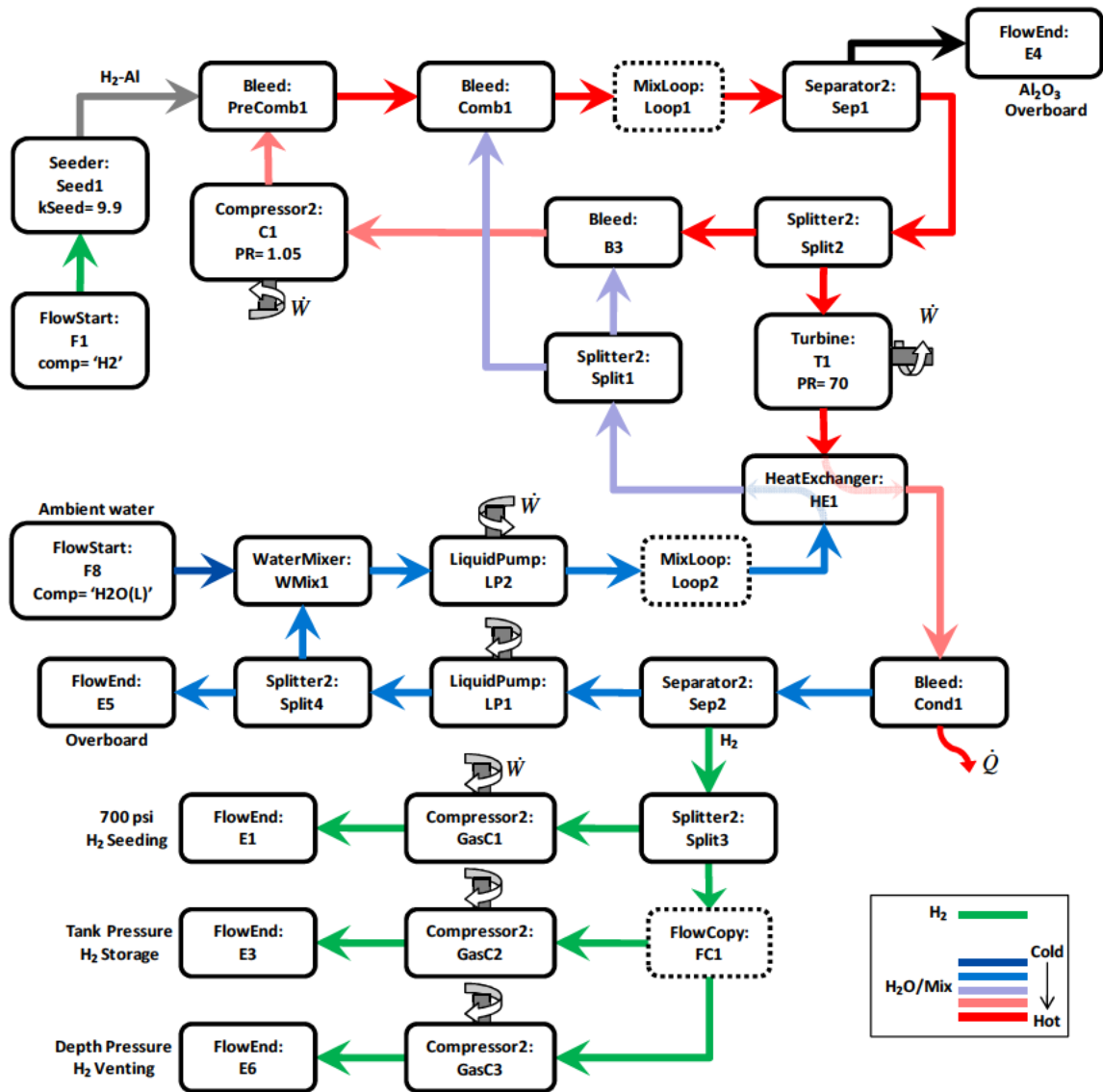


Figure 3-1: NPSS model of HAC system.

In this model, the thermodynamics package considers the following subset of chemical species: gaseous water "H₂O", aluminum cubic crystal "AL(cr)", liquid water "H₂O(L)", gaseous hydrogen "H₂", α aluminum oxide "AL₂O₃(a)", liquid hydrogen peroxide "H₂O₂(L)", gaseous oxygen "O₂", hydroxide molecule "OH", atomic hydrogen "H", and atomic aluminum "AL".

NPSS will execute components in the order in which they are instantiated, which makes the order in which components are created critical to the ability of a model to run.

Because the system is composed of two intertwining closed flow loops, two Loop Start elements (Loop1 and Loop2) are required to proceed toward a solution. Loop1 enables the model to estimate the combustor exit conditions (which are recursively dependent on themselves via the steam recirculation loop), and Loop2 enables the model to estimate the feed water conditions (which are recursively dependent via the heat exchanger).

The component order of execution for this model is presented in Appendix C. Complete lists of the independent variables and dependent conditions for the model are also found in Appendix C.

3.3 HAC-SOFC Model

The HAC-SOFC model represents the full analyzed system with aluminum combustion in steam, a fuel cell to consume hydrogen, and compression of the excess hydrogen. The HAC system portion of this model is identical to that described in the previous section. The SOFC component model is inserted immediately downstream of the turbine, and a supporting feed loop is added to supply oxidizer to the cathode. The SOFC operates adiabatically. The diagram of the full system and a close up of the SOFC and oxidizer loop can be found in Figure 3-2 and Figure 3-3, respectively.

The figures follow the same format as Figure 3-1 where dashed line boundaries represent ‘non-physical’ NPSS elements, rotating shaft symbols indicate shaft work, and heat

rejection is illustrated as a wavy red arrow. Because the oxidizer feed path is a loop, a third ‘non-physical’ MixLoop element (Loop3) is required. The HAC-SOFC model uses the same thermodynamics package as the HAC model with the same chemical species considered (see Section “3.2 Hybrid Aluminum Combustor Model”).

The component order of execution for this model is presented in Appendix D. Complete lists of the independent variables and dependent conditions for the model are also found in Appendix D.

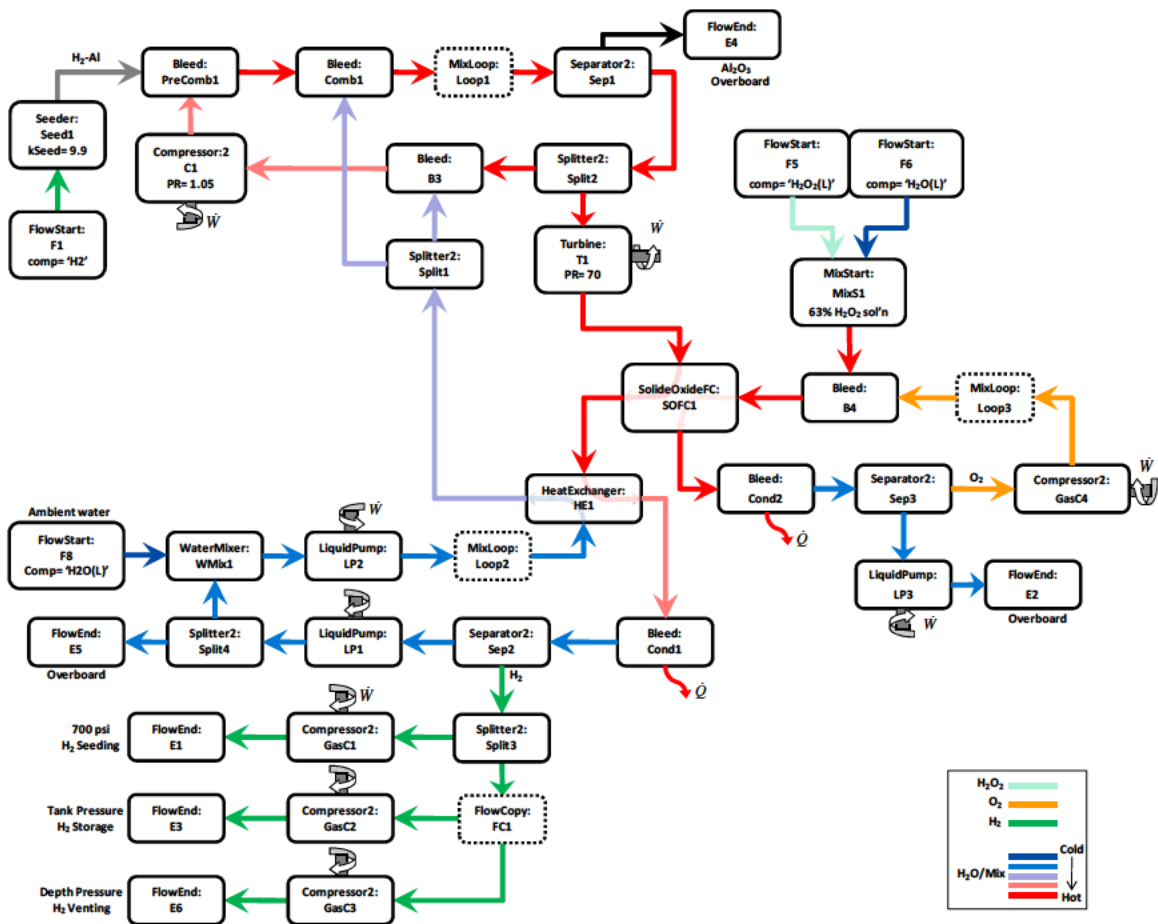


Figure 3-2: NPSS model of HAC-SOFC system.

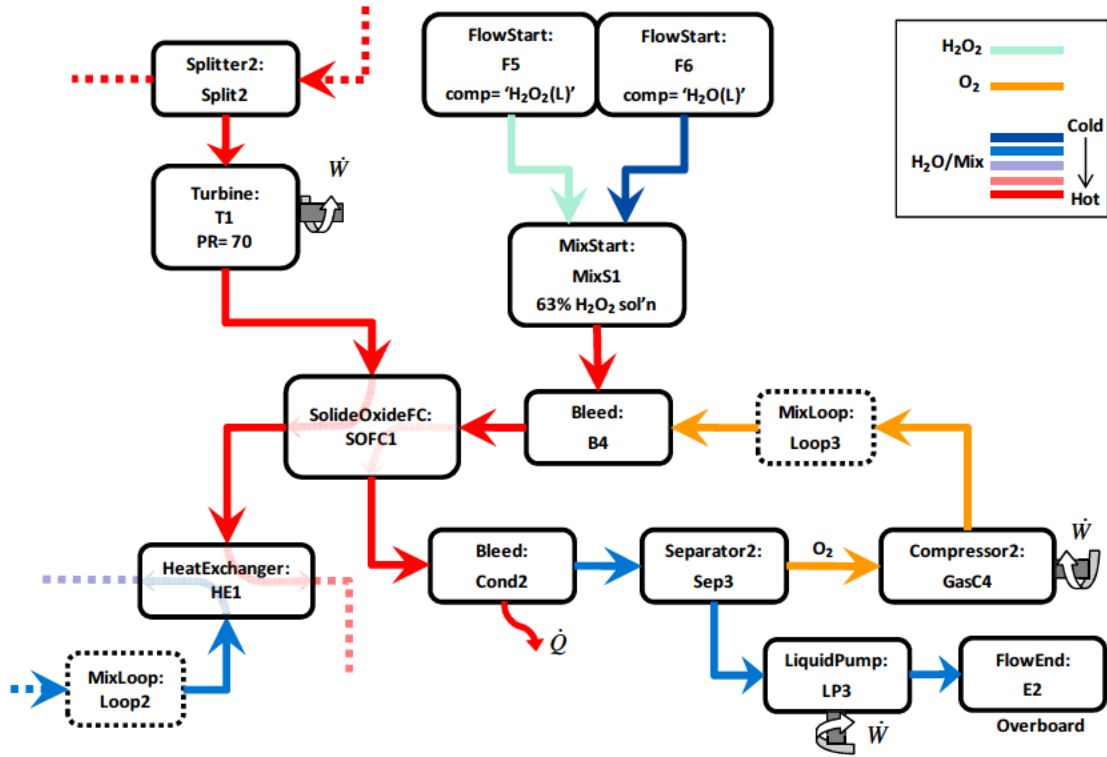
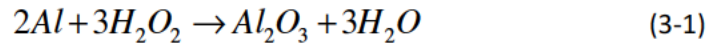


Figure 3-3: NPSS model of HAC-SOFC system (detail of SOFC).

3.4 Aluminum-H₂O₂ Combustor Model

The Aluminum-H₂O₂ Combustor model was developed to analyze the performance of a system comparable to the HAC-SOFC where the H₂O₂ is reacted directly with the aluminum. This system injects the hydrogen peroxide directly into the combustor. Instead of the aluminum-steam reaction, the combustor utilizes the following reaction:



This is the same net reaction as the HAC-SOFC system when all H₂ produced in the combustor is consumed in the fuel cell. The reaction produces no gasses except steam which will be condensed. Therefore, the only compression necessary is of the recycled hydrogen for aluminum seeding. Also, because the reaction is not with the steam, no

recirculation loop is required. Eliminating the fuel cell, recirculation loop, and multiple compressors, gives a much simpler system. However, the Separator element ‘Sep1’ is still required to remove the alumina from the flow stream. The diagram of the NPSS system model for this configuration is presented in Figure 3-4.

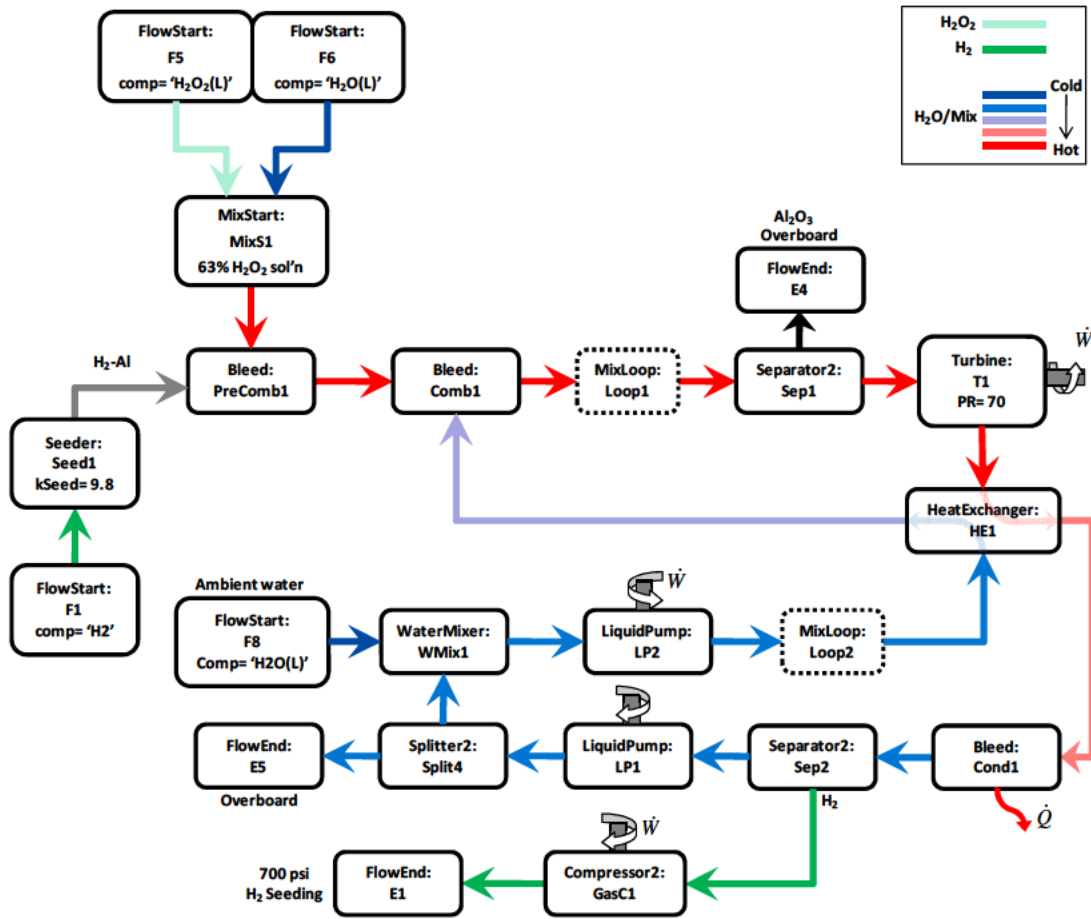


Figure 3-4: NPSS model of Aluminum-H₂O₂ Combustor system.

All component names are consistent with the comparable component of the HAC-SOFC model. Because the model has multiple flow loops, two MixLoop elements are still required. However, Figure 3-4 clearly shows that the overall system is much simpler than the HAC-SOFC. The Aluminum-H₂O₂ Combustor model again uses the same

thermodynamics package as the HAC and HAC-SOFC models with the same chemical species considered (see Section “3.2 Hybrid Aluminum Combustor Model”).

The component order of execution for this model is presented in Appendix E. Complete lists of the independent variables and dependent conditions for the model are also found in Appendix E.

3.5 Hydrocarbon Fueled Combustor Model

The Hydrocarbon Fueled Combustor model was developed to analyze the performance of a system comparable to the HAC-SOFC where a standard hydrocarbon fuel is used instead of aluminum. This system reacts a hydrocarbon fuel (iso-octane) with the hydrogen peroxide. Similar to the Aluminum-H₂O₂ Combustor model, no recirculation loop is required. However, the hydrocarbon reaction produces carbon dioxide which needs to be compressed. Separator element ‘Sep1’ is no longer required because there are no solid products to remove from the stream. Separator element ‘Sep2’ separates the gaseous combustion products (primarily CO₂; no H₂ in this system) so they can be compressed by Compressor element ‘GasC1’. The diagram of the NPSS system model can be found in Figure 3-5.

All component names are consistent with the comparable component in the other models. The Hydrocarbon Fuel Combustor model uses a similar thermodynamics package to the other models, but with different chemical species considered. In this model, the CEA thermodynamics package is used and it considers the following subset of chemical

The diagram illustrates the CO₂ capture system for a 100 MW power plant. It shows the flow of various components and streams. Key components include FlowStart (F5, F6, F9, F8), MixStart (MixS1), Bleed (PreComb1, Comb1, Cond1), MixLoop (Loop1, Loop2), Turbine (T1), HeatExchanger (HE1), WaterMixer (WMix1), LiquidPump (LP1, LP2), Separator2 (Sep2), FlowCopy (FC1), Compressor2 (GasC2, GasC3), and FlowEnd (E5, E3, E6). The diagram also shows the flow of H₂O₂, CO₂, C₈H₁₈, and H₂O/Mix. A legend indicates the color coding for these streams: H₂O₂ (light green), CO₂ (green), C₈H₁₈ (brown), and H₂O/Mix (blue for cold, red for hot). The diagram is labeled 'Figure 10. CO₂ capture system for a 100 MW power plant'.

64

The component order of execution for this model is presented in Appendix F. Complete lists of the independent variables and dependent conditions for the model are also found in Appendix F.

Chapter 4: Analysis Methods

4.1 Scaling Methodology

4.1.1 Challenges and Objectives

Incorporating a fuel cell into the base Hybrid Aluminum Combustor (HAC) system has obvious benefits as far as overall efficiency of the system is concerned simply because a portion of the power will be produced by a more efficient subsystem (the fuel cell) than the basic Rankine power cycle. However, for the UUV application overall thermodynamic efficiency is not necessarily an important metric of performance. As discussed previously, maximum range is achieved by increasing the system's volumetric energy density (that is, the useable energy stored per unit volume). Therefore, a high efficiency system with low energy density is not an effective solution for this application.

Using energy density as the measure of performance presents a challenge at this level of analysis. Because the majority of the thermodynamic analysis is independent of physical dimensions, there is not a simple and accurate method for correlating a physical mass and volume with a particular system with a given power output. However, it is crucial to accurately predict the volume of the mechanical system and the fuel cell in order to estimate the overall energy density. It is also important to accurately predict the mass if one wants to estimate neutral buoyancy energy density. Sections "4.1.2 HAC Scaling" and "4.1.3 SOFC Scaling" explain the methodology employed to estimate the mass and volume of the HAC and SOFC portions of the system.

4.1.2 HAC Scaling

General Component Scaling:

The methodology used for scaling the HAC system is loosely based on the procedure used in scaling aircraft engines [37] and is grounded in simple underlying principles. The fundamental assumptions are as follows:

1. Each component is cylindrical ($V_{comp} = \pi D^2 L / 4$)
2. Flow velocity through a component is constant
 - Cross sectional area will scale linearly with mass flow rate ($\pi D^2 / 4 \propto \dot{m}$)
3. Residence time through a component is constant
 - Component length (L) is constant

Based on these assumptions, the following is true,

$$\frac{V_{comp}}{V_{comp,ref}} = \left(\frac{\pi D^2 L}{4} \right) \left(\frac{4}{\pi D_{ref}^2 L_{ref}} \right) = \left(\frac{\pi D^2 / 4}{\pi D_{ref}^2 / 4} \right) \cdot \left(\frac{L}{L_{ref}} \right) \quad (4-1)$$

$$V_{comp} = V_{comp,ref} \left(\frac{\dot{m}}{\dot{m}_{ref}} \right) \quad (4-2)$$

By making the additional assumption that overall density of the system

($\rho_{HAC} = M_{HAC} / V_{HAC}$) remains constant as volume increases (an assumption that is approximately true for long thin-walled pressure vessels), it is reasonable to assume that system mass scales linearly with the volume. From these assumptions, it follows that:

$$M_{comp} = M_{comp,ref} \left(\frac{\dot{m}}{\dot{m}_{ref}} \right) \quad (4-3)$$

The mass flow rate (\dot{m}) used for scaling is always the total mass flow through the component.

The current research focuses on estimating volumetric energy density so component *volume* estimates are most important. However, estimating neutral buoyancy energy density is also very important. Therefore, future work will need equally accurate estimates of component *mass* which may require more detailed assumptions about the scaling of density.

Heat Exchanger Scaling:

The scaling described in previous section is used for all HAC component types except the heat exchanger. In addition to the mass flow through the heat exchanger, its volume will also depend on the required effectiveness. For this analysis, the component is treated as a simple straight-tube, counter-current heat exchanger as shown in Figure 4-1. The relevant assumptions for scaling are as follows:

1. The heat exchanger is cylindrical ($V_{HE} = \pi D^2 L / 4$)
2. Flow velocity through the exchanger is constant
 - Cross sectional area scales linearly with mass flow rate
 - $\pi D^2 / 4 \propto \dot{m}_{Hot} + \dot{m}_{Cold}$
3. The convective heat transfer coefficient (h) is a constant
 - This is a major assumption that is equivalent to assuming that the flow through the component is fully developed. Future work should account for the spatial dependence of h .

4. Heat transfer surface area is proportional to mass flow ($A \propto \dot{m}_{Hot}$)
 - Accomplished by increasing the number, not the size, of the hot side flow passages
5. Specific heat capacity (c_p) of each stream is constant through the exchanger

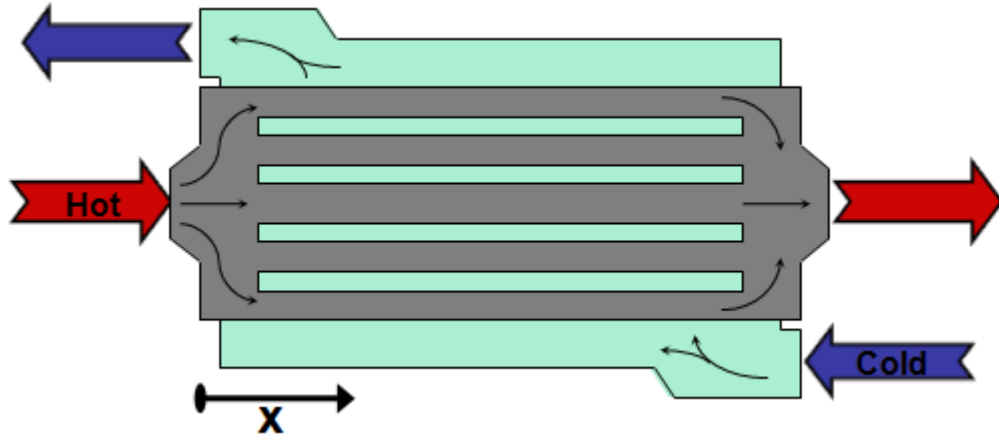


Figure 4-1: Straight-tube, counter-current heat exchanger.

Based on the standard forced convective heat transfer equation (Eq. 4-4) and assumptions 3 and 4 above, it can easily be shown that heat transfer per unit mass is proportional to the temperature difference between the hot and cold streams (ΔT_{H-C}) at that axial location (Eq. 4-6).

$$\dot{Q} = h \cdot A \cdot \Delta T_{H-C} \quad (4-4)$$

$$A = c_0 \cdot \dot{m}_{Hot} \quad (4-5)$$

$$\dot{Q} = h \cdot c_0 \cdot \dot{m}_{Hot} \cdot \Delta T_{H-C} \rightarrow \frac{\dot{Q}(x)}{\dot{m}_{Hot}} \propto \Delta T_{H-C}(x) \quad (4-6)$$

$$\dot{Q}(x) = \dot{Q}_{H \rightarrow C}(x) = -\dot{Q}_{C \rightarrow H}(x) \quad (4-7)$$

The axial location 'x' will be considered as measured from the hot side inlet, as shown in Figure 4-1. This implies that the temperature of both streams will *decrease* with

increasing 'x' even though the cold side flow of course gets warmer along its own flow direction. The heat transfer, \dot{Q} , is defined as the transfer of heat from the hot stream to the cold stream. The transfer rate when referenced from cold to hot will therefore be defined as $-\dot{Q}$, as shown in Eq. 4-7.

Making the additional assumption of constant specific heat for each stream (#5 listed previously) allows the formulation of the integral equations shown as Eq. 4-8 and 4-9. These equations define the temperature profile in each channel given known boundary conditions. An additional boundary condition can be determined for a known heat exchanger effectiveness, ε , based on the definition of effectiveness (Eq. 4-10). The definition can be rearranged to solve for the cold flow exit temperature (Eq. 4-12).

$$\frac{1}{\Delta x} \int_{x_1}^{x_2} \dot{Q}_{C \rightarrow H} dx = -\frac{1}{\Delta x} \int_{x_1}^{x_2} \dot{Q} \cdot dx = \dot{m}_{Hot} \cdot C_{p,Hot} \cdot [T_{Hot}(x_2) - T_{Hot}(x_1)] \quad (4-8)$$

$$\frac{1}{\Delta x} \int_{x_1}^{x_2} \dot{Q}_{H \rightarrow C} dx = \frac{1}{\Delta x} \int_{x_1}^{x_2} \dot{Q} \cdot dx = \dot{m}_{Cold} \cdot C_{p,Cold} \cdot [T_{Cold}(x_1) - T_{Cold}(x_2)] \quad (4-9)$$

$$\varepsilon = \left(\frac{T_{Cold,Out} - T_{Cold,In}}{T_{Hot,In} - T_{Cold,In}} \right) \left(\frac{1}{C_{Ratio}} \right) \quad (4-10)$$

$$C_{Ratio} = \left(\frac{\dot{m}_{Hot} \cdot C_{p,Hot}}{\dot{m}_{Cold} \cdot C_{p,Cold}} \right) \quad (4-11)$$

$$T_{Cold} \Big|_{x=0} = T_{Cold,Out} = T_{Cold,In} + \varepsilon \cdot C_{Ratio} (T_{Hot,In} - T_{Cold,In}) \quad (4-12)$$

Given both temperature states at $x=0$, the equations can be numerically integrated from $x=0 \rightarrow L$ using the simplest finite difference approximation (assuming \dot{Q} is constant over the short span Δx), as described in Eq. 4-13 and 4-14. The value of the length, L , must be iteratively solved for until the calculated $T_{Cold}(x=L)$ equals the known value. By

repeating this process for a range of heat capacity ratios and exchanger effectiveness values, the family of curves depicted in Figure 4-2 was produced from which the length ratio between two known states can be derived. The Matlab code which performs these calculations is attached in Appendix B.

$$T_{Hot}(x + \Delta x) = T_{Hot}(x) + c_1 \cdot \Delta T_{H-C}(x) \quad (4-13)$$

$$\rightarrow c_1 = (-h \cdot c_0) / (C_{p,Hot})$$

$$T_{Cold}(x + \Delta x) = T_{Cold}(x) + [T_{Hot}(x + \Delta x) - T_{Hot}(x)] \cdot C_{Ratio} \quad (4-14)$$

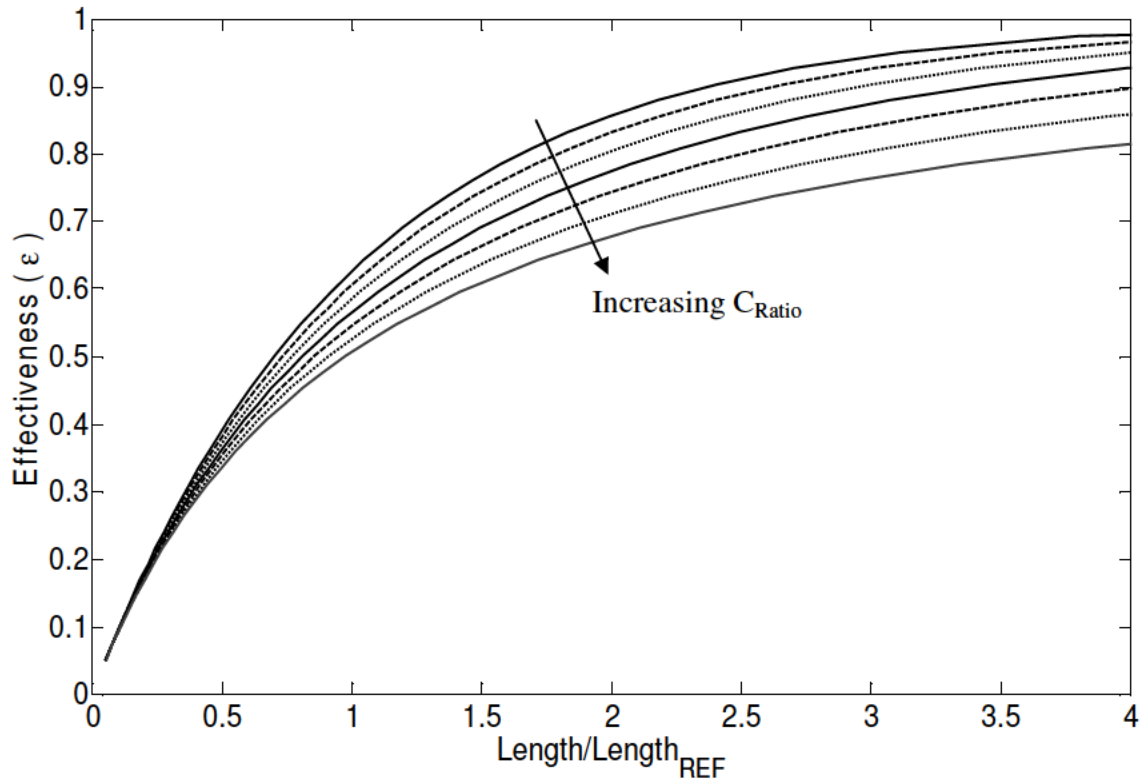


Figure 4-2: Heat exchanger effectiveness v. length.

Given these assumptions about how the length and diameter of the heat exchanger will vary, the non-linear scaling can be described as follows:

$$V_{HE} = V_{HE,ref} \left(\frac{\dot{m}}{\dot{m}_{ref}} \right) \cdot \left(\frac{L(\epsilon, C_{Ratio})}{L(\epsilon_{ref}, C_{Ratio,ref})} \right) \quad (4-15)$$

$$M_{HE} = M_{HE,ref} \left(\frac{\dot{m}}{\dot{m}_{ref}} \right) \cdot \left(\frac{L(\epsilon, C_{Ratio})}{L(\epsilon_{ref}, C_{Ratio,ref})} \right) \quad (4-16)$$

The mass flow is the combined hot and cold side flows, and the length ratios can be interpolated from the tabulated results of the Matlab code.

Overall HAC Scaling:

The individual component scaling is applied to the overall HAC system through simple estimates of the original size of each component relative to the whole system. That is to say, an estimate is made for the volume fraction that each component (and its associated equipment and fittings) contributes to the system as a whole. These estimates are based on the mass flow through each component and the relative sizes of different types of components compared to one another. The actual estimates used for the HAC scaling are summarized in the last column of Table 4-1 below.

Table 4-1: Components with reference mass flow and volume fraction.

<i>Element Type</i>	<i>Name</i>	\dot{m}_{ref} (lb/s)	<i>Vol. Fraction</i>
Bleed (combustor)	Comb1	0.1838	15.0%
Bleed (condenser)	Cond1	0.1257	8.0%
Bleed (pre-combustor)	PreComb1	0.0648	5.0%
Compressor2	C1	0.0324	2.5%
HeatEx	HE1	0.2549	25.0%
Compressor2	GasC1	0.0030	1.0%
Compressor2	GasC2	0.0033	1.0%
LiquidPump	LP1	0.1292	10.0%
Seeder	Seed1	0.0324	2.5%
Separator2	Sep1	0.1838	10.0%
Separator2	Sep2	0.1257	10.0%
Turbine	T1	0.1257	10.0%

The reference mass, volume, and mass flows used for scaling are all drawn from earlier work by Penn State ARL [6]. To determine the factor by which the total system volume is scaled, the calculated scale of each component is weighted by reference volume fraction to estimate the contribution to the whole. A simplified example of this process is shown in Table 4-2.

Table 4-2: Sample calculation of scaling.

<i>Element Type</i>	\dot{m}_{ref} (lb/s)	Volume Fraction	\dot{m} (lb/s)	Mass Scaling	Length Scaling	
Seeder	0.05	5%	0.07	1.40	-	0.07
LiquidPump	0.15	10%	0.16	1.07	-	0.11
Bleed	0.20	20%	0.23	1.15	-	0.23
Turbine	0.20	15%	0.23	1.15	-	0.17
HeatEx	0.40	30%	0.50	1.25	1.35*	0.51
Separator2	0.20	15%	0.23	1.15	-	0.17
Compressor	0.05	5%	0.06	1.20	-	0.06
* Reference: $C_{Ratio}=0.5$, $Eff=0.5$ New: $C_{Ratio}=0.45$, $Eff=0.6$						1.32

4.1.3 SOFC Scaling

The scaling of the fuel cell is a much simpler process than the HAC system scaling. The NPSS model calculates the number of cells required to produce the electrical power necessary for the desired operating conditions. Based on input values for the mass and volume of an individual cell [38], the mass and volume of the SOFC stack can be easily approximated. Although this approach neglects additional factors that could arise in the case of a very large stack, it should yield a good approximation for the size of the fuel cell stack in use here. A large stack, for example, may require proportionally more structural support or proportionally less insulation, but the net effect is expected to be small. It is additionally assumed the size of the pumps and associated piping for the fuel

cell will scale linearly with the size of the stack itself. Based on previous work estimating SOFC size in UUVs [38], the size of the SOFC system is assumed to be 3 times the size of the stack alone. This is an estimate and can be refined as more detailed information becomes available. Therefore, the volume and mass of the SOFC system are given by:

$$V_{SOFC} = \left(\frac{V_{SOFC}}{V_{Stack}} \right) \cdot N_{cell} \cdot V_{cell} = \left(\frac{V_{SOFC}}{V_{Stack}} \right) \cdot \left(\frac{P_{SOFC}}{P_{cell}} \right) \cdot V_{cell} \quad (4-17)$$

$$M_{SOFC} = \left(\frac{M_{SOFC}}{M_{Stack}} \right) \cdot N_{cell} \cdot M_{cell} = \left(\frac{M_{SOFC}}{M_{Stack}} \right) \cdot \left(\frac{P_{SOFC}}{P_{cell}} \right) \cdot M_{cell} \quad (4-18)$$

where V_{SOFC}/V_{Stack} and M_{SOFC}/M_{Stack} are the ratios of SOFC system volume and mass to the volume and mass of the stack alone, assumed to ≈ 3 in each case.

4.2 Performance Metrics

4.2.1 Power, Mass, Volume

The total power of the HAC-SOFC hybrid system is the sum of the power output of its two parts. The mass of the system is the sum of the HAC and SOFC components along with the reactants (aluminum and hydrogen peroxide). The volume of the system is the sum of the volumes of the HAC, SOFC, reactants, and excess H₂ storage tank. Note that these are essentially initial mass values because the entire mass of reactants is considered and the H₂ storage volume is reserved but treated as having no mass.

$$P_{sys} = P_{HAC} + P_{SOFC} \quad (4-19)$$

$$M_{sys} = M_{HAC} + M_{SOFC} + M_{reactants} \quad (4-20)$$

$$V_{sys} = V_{HAC} + V_{SOFC} + V_{reactants} + V_{H_2, storage} \quad (4-21)$$

4.2.2 Reactant Storage

The fixed internal volume of the UUV power section must be appropriately divided between the HAC, SOFC, reactants, and H₂ storage. For the simple case where the excess H₂ is vented overboard and not stored, the calculation is simple:

$$V_{reactants} = V_{sys} - V_{HAC} - V_{SOFC} \quad (4-22)$$

The situation becomes somewhat more complicated when reactants and hydrogen storage must both be accounted for. In this situation, the volume previously reserved for reactants must be split between reactants and waste hydrogen storage (Eq. 4-23). Additional information is needed to determine how this volume is allocated between the two.

The mass of H₂ stored is the product of the H₂ flow rate into the storage volume and the run time of the vehicle, Δt (Eq. 4-24). This leads to the intuitive conclusion that the ratio of H₂ mass to reactant mass will be the ratio of the two mass flows (Eq. 4-25). Similarly, the ratio of the volumes can be derived by including the ratio of the densities (Eq. 4-26).

$$V_{reactants} + V_{H_2, storage} = V_{sys} - V_{HAC} - V_{SOFC} \quad (4-23)$$

$$M_{H_2} = \dot{m}_{H_2, Storage} \cdot \Delta t = \dot{m}_{H_2, Storage} \cdot \left(\frac{M_{reactants}}{\dot{m}_{reactants}} \right) \quad (4-24)$$

$$\frac{M_{H_2}}{M_{reactants}} = \frac{\dot{m}_{H_2, Storage}}{\dot{m}_{reactants}} \quad (4-25)$$

$$\frac{V_{H_2, storage}}{V_{reactants}} = \left(\frac{\rho_{effective}}{\rho_{H_2}} \right) \cdot \left(\frac{\dot{m}_{H_2, Storage}}{\dot{m}_{reactants}} \right) \quad (4-26)$$

By substituting Eq. 4-26 into Eq. 4-23 and rearranging the terms, an expression can be derived for the reactant storage volume that only contains known quantities (Eq. 4-27).

The reactant mass, hydrogen mass, and hydrogen volume can then all be easily calculated using the effective reactant density, Eq. 4-25, and Eq. 4-23, respectively.

$$V_{reactants} = \frac{V_{sys} - V_{HAC} - V_{SOFC}}{1 + \left(\frac{\rho_{effective}}{\rho_{H2}} \right) \cdot \left(\frac{\dot{m}_{H2,Storage}}{\dot{m}_{reactants}} \right)} \quad (4-27)$$

$$M_{reactants} = \rho_{effective} \cdot V_{reactants} \quad (4-28)$$

The density of the stored H₂ can be calculated by assuming it can be approximated as an ideal gas (Eq. 4-29). Because the mass and volume of reactants discussed above refers to the combination of aluminum powder and hydrogen peroxide used in the system, the effective density of the combined reactants must be determined to properly use Eq. 4-26, 4-27, and 4-28. As such, the weighted average density of the reactants can be found as shown in Eq. 4-30.

$$\rho_{H2} = \frac{P_{Storage}}{R_{H2} \cdot T_{Storage}} \quad (4-29)$$

$$\rho_{effective} = \frac{M_{reactants}}{V_{reactants}} = \frac{\dot{m}_{reactants}}{\dot{V}_{reactants}} = \frac{\dot{m}_{AL} + \dot{m}_{peroxide}}{\left(\dot{m}_{AL} / \rho_{AL} \right) + \left(\dot{m}_{peroxide} / \rho_{peroxide} \right)} \quad (4-30)$$

4.2.3 Energy Density

The volumetric energy density of a system is defined as the useable energy storage per unit volume. That is to say, the amount of energy from the reactants converted to useable electric or mechanical work divided by system volume. The useable energy storage (E_S) is the total chemical energy storage - the reaction specific enthalpy of the reactants - multiplied by the overall conversion efficiency (Eq. 4-31). Rewriting the product of efficiency and reaction enthalpy as the ratio of system power output to reactant flow ratio

gives the alternate expression in Eq. 4-32. Note that this expression is equivalent to stating $\Delta E = P \cdot \Delta t$, which should hold true for any constant power process.

$$E_S = (\eta_0 \cdot \Delta H_{reactants}) \cdot M_{reactants} \quad (4-31)$$

$$E_S = \left(\frac{P_{sys}}{\dot{m}_{reactants}} \right) \cdot M_{reactants} = (P_{HAC} + P_{SOFC}) \frac{M_{reactants}}{\dot{m}_{reactants}} \quad (4-32)$$

Once the stored energy is known, the volumetric energy density (ED_V) and gravimetric energy density (ED_M) can be calculated as shown in Eq. 4-33 and 4-34.

$$ED_V = \frac{E_S}{V_{sys}} = (P_{HAC} + P_{SOFC}) \frac{M_{reactants}}{V_{sys} \cdot \dot{m}_{reactants}} \quad (4-33)$$

$$ED_M = \frac{E_S}{M_{sys}} = (P_{HAC} + P_{SOFC}) \frac{M_{reactants}}{M_{sys} \cdot \dot{m}_{reactants}} \quad (4-34)$$

Another potentially important performance parameter is the neutrally buoyant energy density. This accounts for the added volume of empty space required for a denser than water system to be made neutrally buoyant. This requires making the overall system density equal to the density of water (Eq. 4-35). Calculating the energy density using the neutrally buoyant volume yields Eq. 4-36. Substituting Eq. 4-35 into 4-36 gives Eq. 4-37 which shows that the neutrally buoyant energy density is simply the product of the gravimetric energy density and the density of water (Eq. 4-37).

$$\frac{M_{sys}}{V_{sys,NB}} = \rho_{water} \quad \rightarrow \quad V_{sys,NB} = \frac{M_{sys}}{\rho_{water}} \quad (4-35)$$

$$ED_{V,NB} = \frac{E_S}{V_{sys,NB}} = \left[(P_{HAC} + P_{SOFC}) \frac{M_{reactants}}{M_{sys} \cdot \dot{m}_{reactants}} \right] \cdot \rho_{water} \quad (4-36)$$

$$ED_{V,NB} = ED_M \cdot \rho_{water} \quad (4-37)$$

Chapter 5: Model Performance Results

5.1 Objectives

Using the NPSS system models described previously, the volumetric energy density (which is proportional to range) of each system can be predicted over a wide range of operating conditions. Ultimately, this will allow a comparison between the proposed configurations and existing technologies such as batteries and fuel cells.

5.2 HAC System Performance

The HAC system model (see Figure 3-1) was first examined for an initial operating condition corresponding to an earlier analysis of the system performed by Hamilton Sundstrand [16]. Earlier work by Eagle [2] has shown that system performance at this operating condition can be improved by varying the aluminum fuel mass flow rate or the feed water mass flow rate while holding other parameters constant. By applying this methodology to the HS design point, the relationships between efficiency and mass flow (aluminum or feed water) can be investigated.

For the variation of aluminum mass flow, the design space is explored over a range of operating points representing the full range of conditions that can match the design point conditions. In physical terms, below a certain fuel mass flow rate the turbine exhaust lacks the enthalpy to heat the feed water to the target temperature (limited by $\epsilon \leq 1$). Above a certain fuel mass flow, there is not enough feed water to adequately cool the recirculation steam loop. The operation of the system is varied by the increases or decreases in the aluminum flow rate. This is accomplished in NPSS by slowly marching

away from the design point solution by perturbing the mass flow of aluminum, using the most recently calculated solution as the initial condition, and then converging to a new solution. This method is effective assuming large discontinuities are not present within the solution space. In this simulation, the recirculation mass flow is scaled to the fuel flow to allow complete stoichiometric combustion, but all other design values are held as fixed parameters including the feed water mass flow rate. Overall efficiency is defined as the ratio of net power output to the net power released by complete reaction of the fuel. Figure 5-1 shows the results of this analysis. Mass flow is normalized by the initial value.

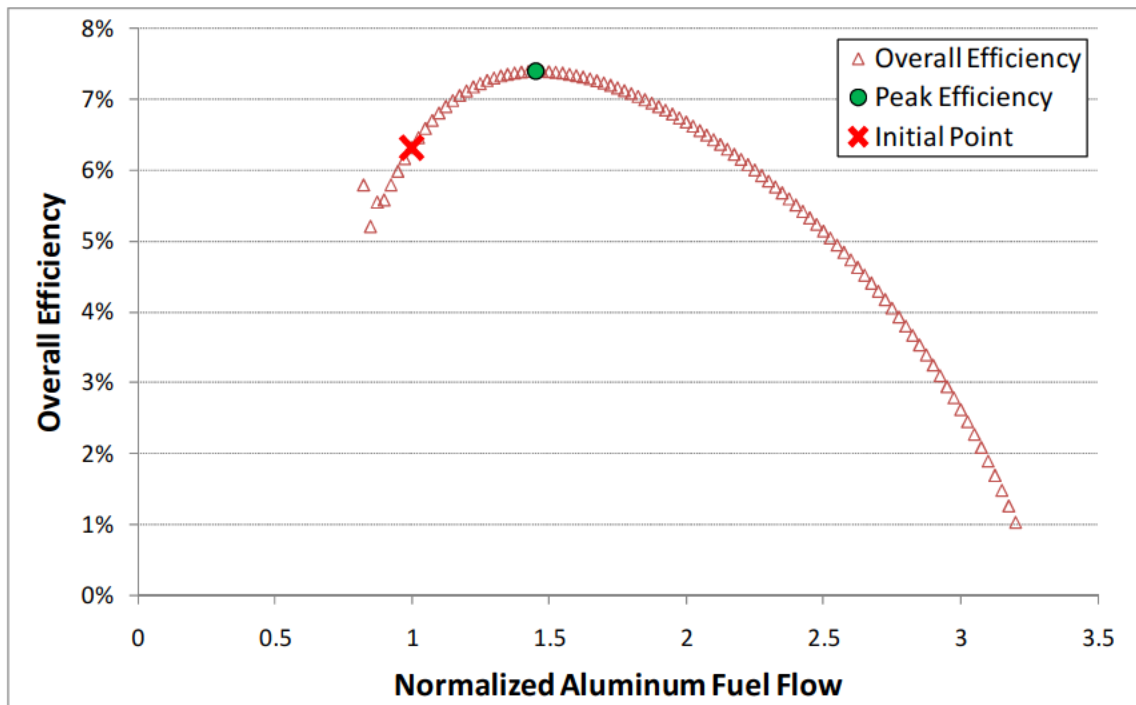


Figure 5-1: HAC efficiency v. aluminum flow rate.

There is a clear peak in efficiency at increased aluminum flow rate. As fuel mass flow is increased, combustion temperatures and hydrogen mass fraction increase which improves turbine efficiency. However, at the same time recirculation steam flow increases requiring increased steam compression work, and heat exchanger effectiveness decreases

allowing more heat to escape the system. These competing effects result in the peak seen in the figure.

For the variation of feed water mass flow, the design space is similarly explored over the full range of operating points for which a converged solution exists. The water flow is limited on the low end by the minimum required to cool the recirculation loop to the target temperature. Water flow reaches a maximum where the excess water cools the system so much that the turbine exit flow lacks the enthalpy to raise the feed water temperature to the proper value within the heat exchanger. Figure 5-2 illustrates the effect of feed water flow variation. A peak in efficiency occurs at reduced water flow rate.

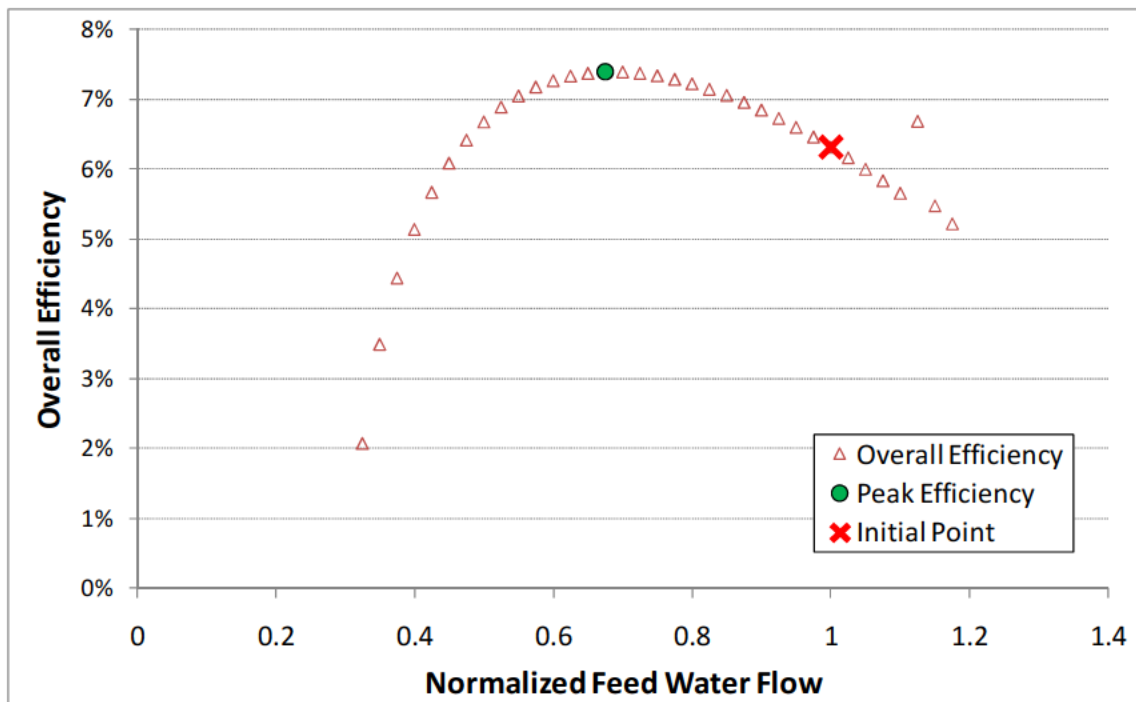


Figure 5-2: HAC efficiency v. feed water flow rate.

These results are essentially a reproduction of the previous work by Eagle [2], but with the important addition of hydrogen compression losses which reduce efficiency.

Including hydrogen compression work greatly increases the accuracy of the simulations.

Also upon further inspection, there are additional conclusions that can be drawn from these results beyond what was presented in that work. It has been observed that for a given set of conditions, the peak efficiency conditions for the fuel and water variation simulations have the exactly the same efficiency and also the same heat exchanger effectiveness, splitter bypass ratios, flow composition, and temperatures throughout the system. That is to say, the peaks correspond to essentially the same condition but with all mass flows proportionally scaled. Figure 5-3 re-plots the data for both parameter variations in terms of feed water-to-fuel ratio.

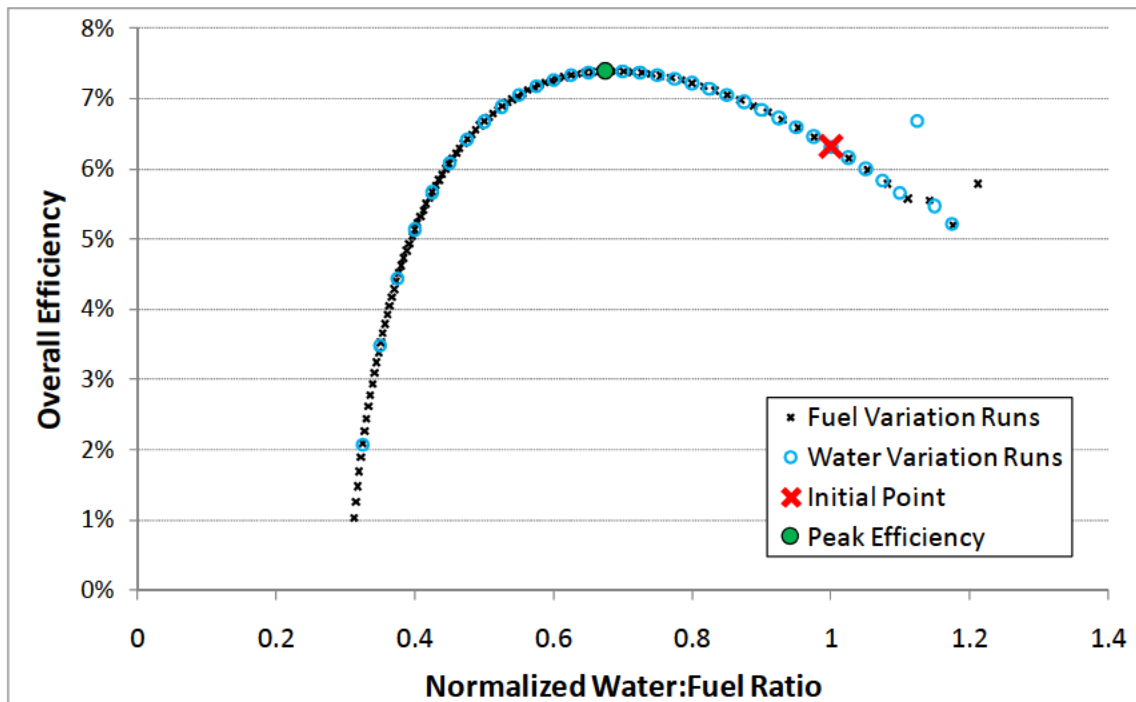


Figure 5-3: HAC efficiency v. water/fuel ratio.

The fact that both sets of data collapse to a single curve when plotted against the ratio shows that it is this ratio, and not either flow rate individually, that governs the efficiency of the HAC system. Optimal efficiency can be maintained by fixing this ratio and a desired power output can be obtained by properly scaling the fuel mass flow. In this manner, an optimized design point for any power output can be obtained.

5.3 HAC-SOFC Performance

5.3.1 Importance of Current Density

When adding the SOFC to the HAC system, it is important to determine an appropriate operating state for the fuel cell. The key parameter under the user's control is the cell current density. Most other operating parameters are fixed by the overall system operating state. Anode incoming flow composition and temperature will both have a strong impact on performance, but these values are controlled by the HAC operation.

The performance variation of the system as a function of current density can be analyzed by holding net system power output and percent hydrogen utilization fixed while current density varies. Figure 5-4 shows fuel cell voltage and power density as functions of current density at a system net power of 15 kW (assuming venting of excess H_2) with H_2 utilization at 53% (the reason for this percentage is explained in the following section). It is important to note that this is *NOT* directly analogous to a typical V-I fuel cell curve where temperature and inlet flow compositions are held constant. Inlet flow is determined by HAC operation, and SOFC temperature varies with inlet temperature and current density. It is also important to note that the curves would be different at different H_2 utilization percentages, but optimizing current density for each unique operating condition is beyond the scope of the current work.

An interesting feature of Figure 5-4 is the low reversible cell voltage, or open circuit voltage (OCV), of only 0.75 V which is well below typical values (> 1 V) for most SOFC arrangements [31] [32] [39]. An examination of Eq. 2-43 shows that this occurs because

the fraction of hydrogen in the anode flow is low (approx. 10% by mass compared to >50% in typical studies). The dependence of OCV on hydrogen and steam partial pressures at the anode drives the cell voltage down. This is consistent with other fuel cell modeling involving humidified anode flows [33].

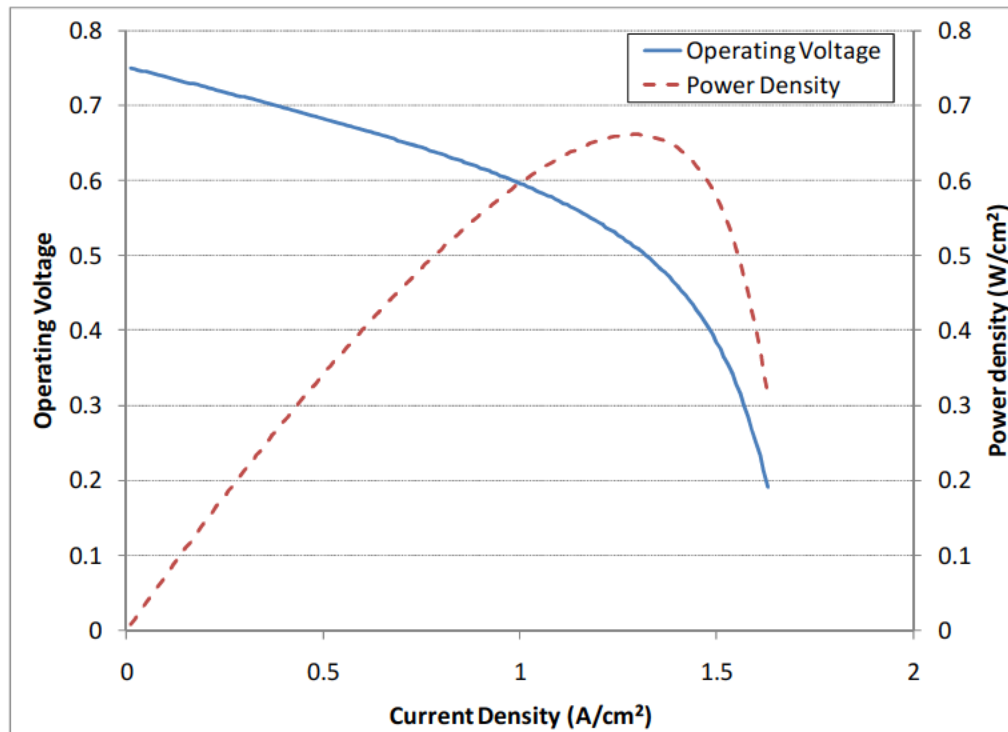


Figure 5-4: Voltage and power density v. current density ($P_{NET}=15$ kW, H_2 ut.=53%).

At first glance, it may seem that the SOFC should operate at peak power density which would result in the smallest possible fuel cell stack. However, Figure 5-5 reveals that this is not the case. The figure shows that energy density peaks at 0.44 A/cm^2 , well below the peak power density. The reason for this is made clear in Figure 5-6 which shows how the three largest components of net power change with current density. At very low current density, system energy density is very low because the SOFC stack is enormous and allows no room for fuel storage. However, as current density increases, the power output of the SOFC dips as the operating voltage begins to drop off. At very high current

density, the increased size of the HAC required to offset the SOFC power dip more than negates the volume saved by using a smaller stack. The best compromise between these effects is the peak exhibited in Figure 5-5. The fact that it occurs at such low current densities indicates that the size penalty associated with the HAC is quite large.

In all subsequent work, the current density will always be equal to the optimum value of 0.44 A/cm^2 . While this will not be optimal for all operating conditions, it is not practical to consider all possible operating conditions in this thesis.

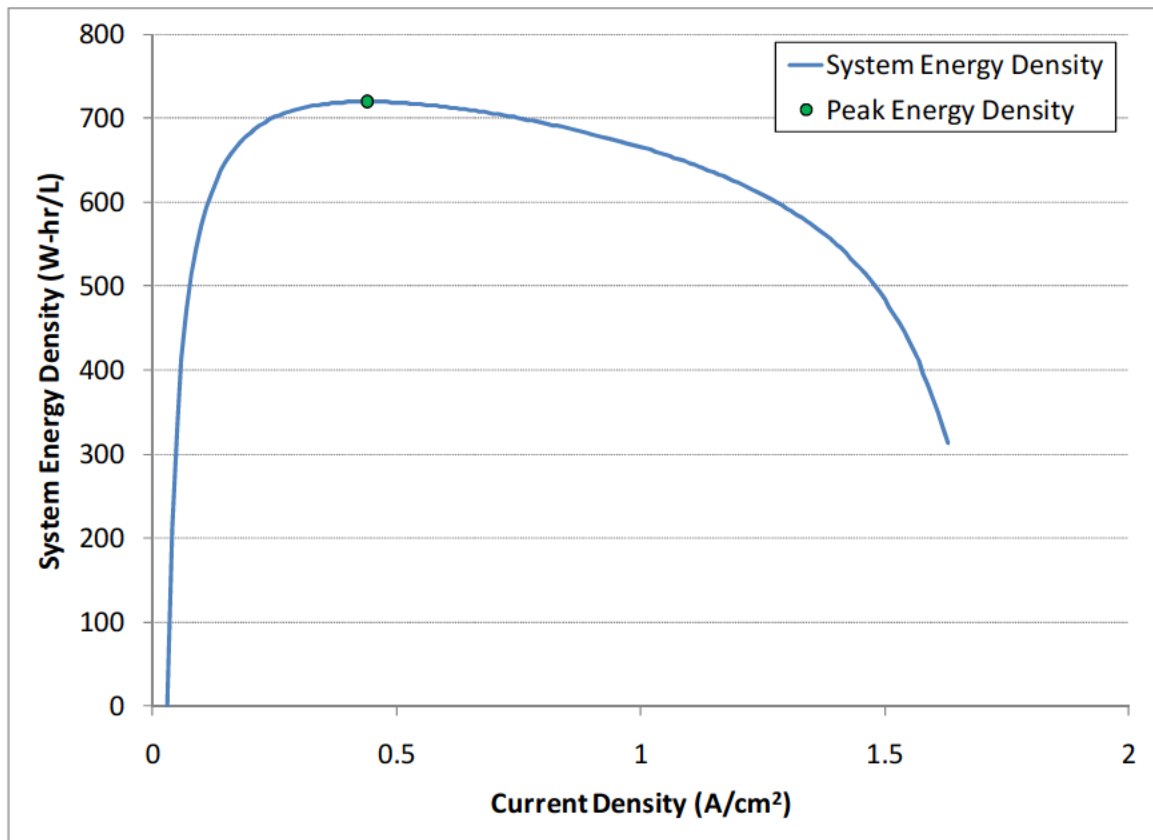


Figure 5-5: System energy density v. current density.

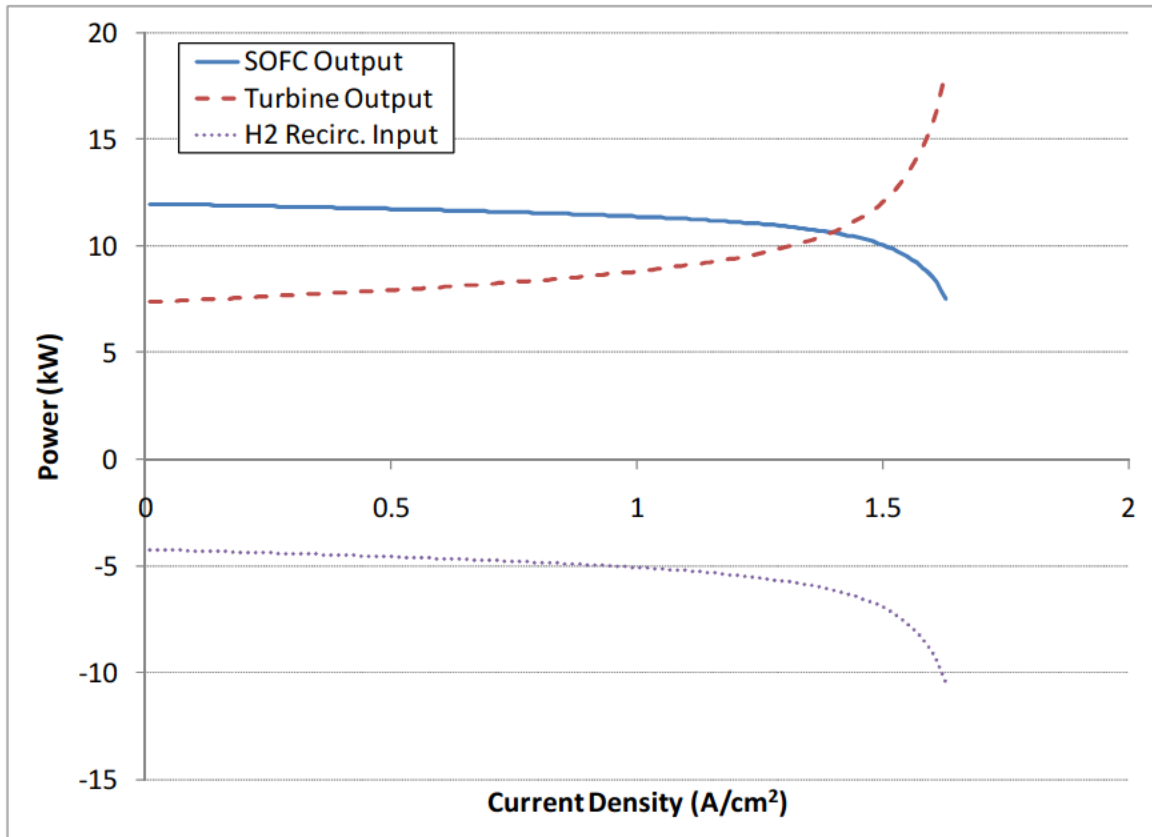


Figure 5-6: Components of power v. current density.

5.3.2 Effects of H_2 Utilization

The HAC-SOFC model (see Figure 3-2) was run over a variety of operating conditions using the optimized water-to-fuel ratio HAC system design point as a starting point. The NPSS model was initially run with the H_2 utilization set at 0% which corresponds to the case where the fuel cell is off or the base HAC system is operating without a fuel cell.

Running the model at 0% utilization gives identical results to those obtained by the HAC model without the fuel cell presented earlier in Section “5.2 HAC System Performance”.

Four “cases” have been analyzed and they are summarized as follows:

A. “No compression work”

- Net power of the system is calculated without accounting for disposal of the remaining H₂ gas
- No volume is allotted for H₂ storage

B. “H₂ venting”

- Net system power is calculated while assuming that all excess H₂ must be compressed to the local depth pressure in order to be dumped overboard
- No volume is allotted for H₂ storage

C. “H₂ storage”

- Net power is calculated assuming that all excess H₂ must be compressed to a specified pressure (1000 psi) and stored in an onboard containment vessel.
- Final volume of the stored H₂ is accounted for in the energy density calculations

D. “H₂ Seeding Tank”

- Net power is calculated assuming all H₂ is vented overboard
- No H₂ is recirculated for fuel seeding because it is assumed that the seeding H₂ is stored in a tank that is filled before the mission
- Initial volume of the stored H₂ is accounted for in the energy density calculations

The different methods of summing net power are described in Appendix D. It is important to note that Case A is not realistic in practice because something must be done with the hydrogen at the end of the cycle. The case is included in this analysis as a reference point of comparison to the earlier work done to model the HAC system. Neglecting the hydrogen compression all together is comparable to previous work by Hamilton Sundstrand [16], Penn State ARL [6], and Eagle [2]. This study has shown that the work required to compress the recycled hydrogen can amount to a large fraction of the total work output and therefore it must be included for an accurate accounting of system performance.

For each case, the system is initially run at 0% H₂ utilization for a 15 kW power requirement. The HAC system is scaled as required by varying the fuel mass flow (which in turn causes other flows in the system to be proportionally scaled). The NPSS model is then run for a series of incrementally higher H₂ utilizations up to the limit of 52.6% above which there would not be enough hydrogen remaining to supply the aluminum seeding system. Case D (feed H₂ storage) lacks this limitation and can simulate higher utilizations. The SOFC system is scaled as required for the necessary H₂ utilization and mass flows. Net power (as defined for the given case) is held constant at each iteration. For Case C (storage), net power will vary over the duration of a mission because the power required to store the hydrogen will increase as the storage tank fills and its pressure rises. Therefore for Case C, the net power at the end of the mission (where power output is lowest) is held constant. This will be discussed further in Section “5.3.4 Cost of H₂ Storage”.

The energy density v. H_2 utilization results for the four cases is presented in Figure 5-7. Clearly, if venting the hydrogen overboard is permissible, it is highly preferable to do so as seen for Case B (blue) in the figure. At low H_2 utilization, Case C (red) is not a viable option. The volume needed for the HAC, SOFC, and H_2 storage exceeds the allotted power section volume leaving no room for fuel. At 52.6% utilization, Cases B and C converge to a single point. This is because without any excess hydrogen, there is no difference between the two. Case D has inferior energy density performance because of large volume required to store the seeding hydrogen leaves little room for fuel. Recall that Case A is not realistic, and is provided for reference only.

Case B, with hydrogen venting, shows a peak in energy density at around 25% hydrogen utilization. As utilization increases, the HAC system shrinks and cycle efficiency increases. At the same time, the SOFC grows and the effective energy density of the stored reactants decreases due to the increased fraction of H_2O_2 . These competing factors result in the peak seen in the figure, which is 12% higher than full H_2 utilization (52.6%) and 24% higher than 0% utilization. It should be noted that operational factors may make operation at 25% utilization undesirable. The system would have the added complexity of the SOFC without eliminating H_2 venting or delivering a game changing performance improvement.

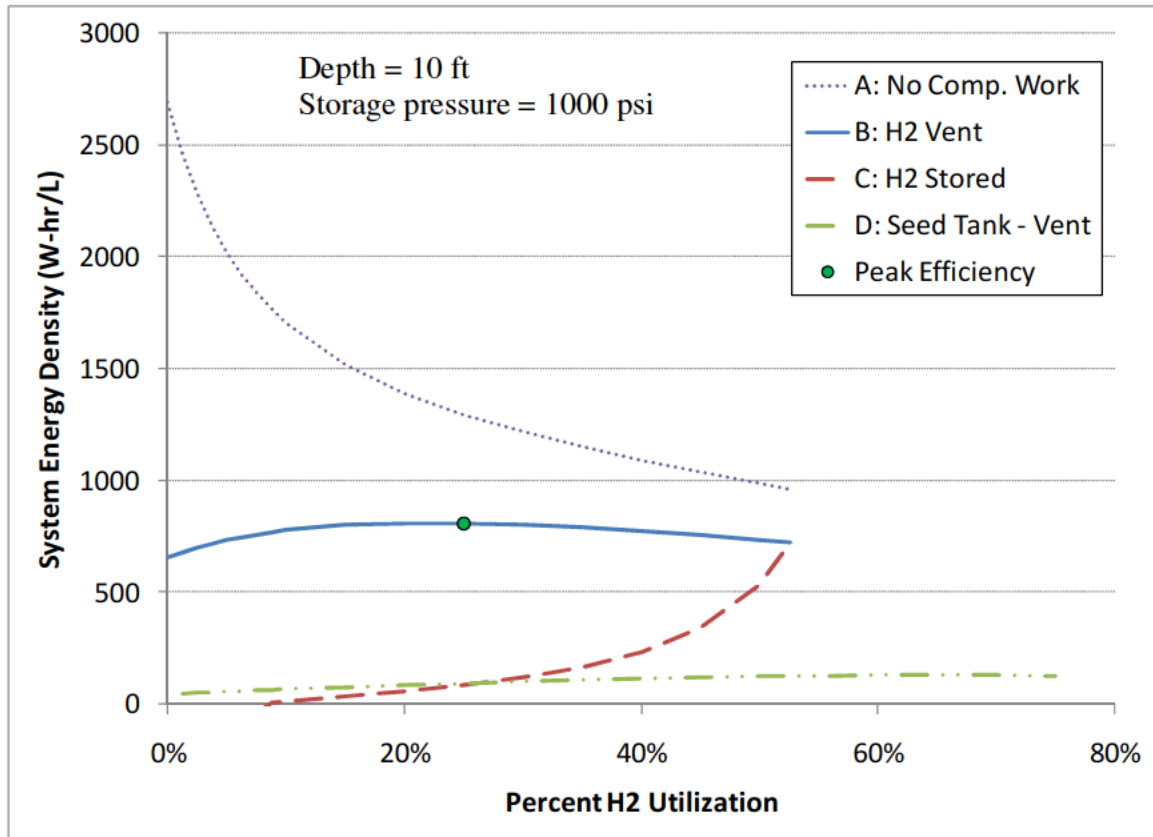


Figure 5-7: HAC-SOFC volumetric energy density v. hydrogen utilization.

5.3.3 Cost of H₂ Venting

Venting the residual hydrogen at the end of the cycle represents a performance penalty. The work required to adiabatically compress the hydrogen up to depth pressure reduces the net output of the system. This impact at a depth of 10 ft. is illustrated in Figure 5-8. The gross work production of the system is represented by red and blue bars for turbine and SOFC work, respectively. From this, the net losses must be subtracted to yield the net power. The losses are counted as H₂ ventilation work (in purple), H₂ recirculation work (in green), and water pump work (in orange). At high H₂ utilization, no work is required to vent because there is no excess hydrogen. With no SOFC (i.e. 0% utilization), the work to vent is quite large. In addition, because the hydrogen recirculation work is

roughly proportional to the turbine work, the losses in the system scale upward as turbine work increases leading fuel consumption to spiral upward and efficiency to plummet. This is evident in Figure 5-8 as the gross work at 0% utilization is several times higher than at 53% utilization for the same net power.

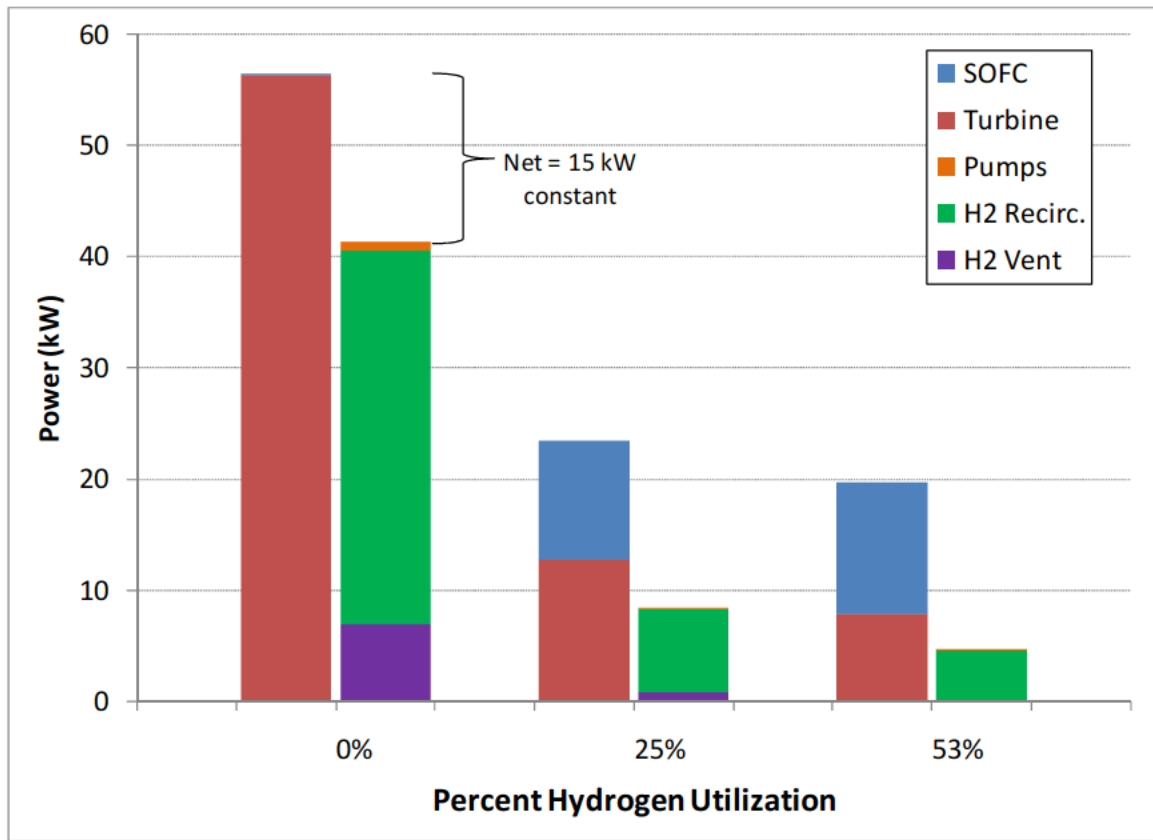


Figure 5-8: HAC-SOFC, with H₂ venting at 10 ft, components of net power output.

5.3.4 Cost of H₂ Storage

Storing the excess hydrogen is the alternative to venting, but this also incurs a significant performance penalty. Unlike venting, which requires compressing the hydrogen to a constant pressure (depth pressure) throughout the runtime of a mission, storage can be accomplished early in the mission with very little compression. The amount of work required increases as the storage tank fills to higher pressures. This variation over the

course of a mission is illustrated in Figure 5-9. Because the storage pressure to which the hydrogen must be compressed is constantly rising, the magnitude of the storage compression work also rises (shown as the red solid line). As this occurs, the net power of the system drops if the fuel flow rate is constant. It is apparent from the figure that near the end of the mission the penalty associated with hydrogen storage is very large.

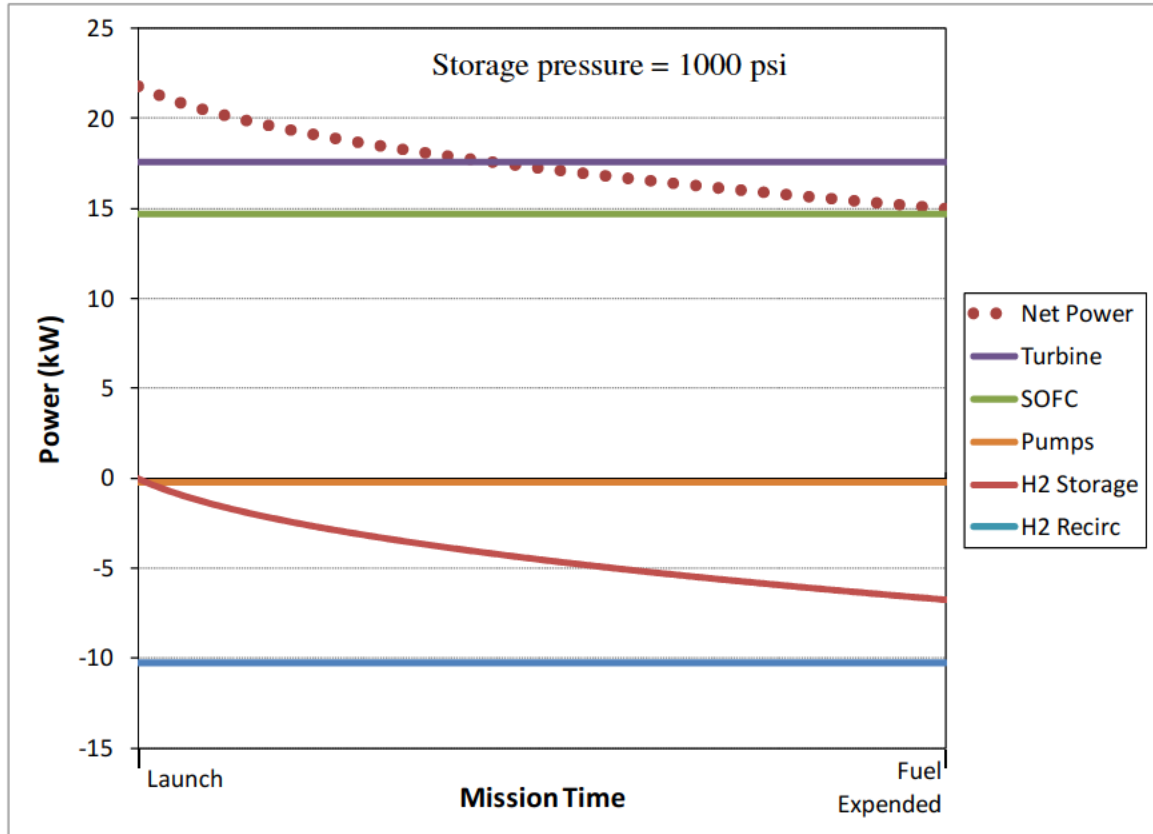


Figure 5-9: HAC-SOFC, with H₂ storage to 1000 psi, variation of net power v. time.

In addition to the work required for adiabatic compression, the stored hydrogen also negatively impacts system energy density due to the large amount of volume required for the storage tanks. These tanks displace fuel and greatly reduce the energy storage capacity of the vehicle. Figure 5-10 shows how as utilization gets lower, the fraction of interior volume reserved for fuel drops to nothing as the HAC, SOFC, and H₂ storage dominate.

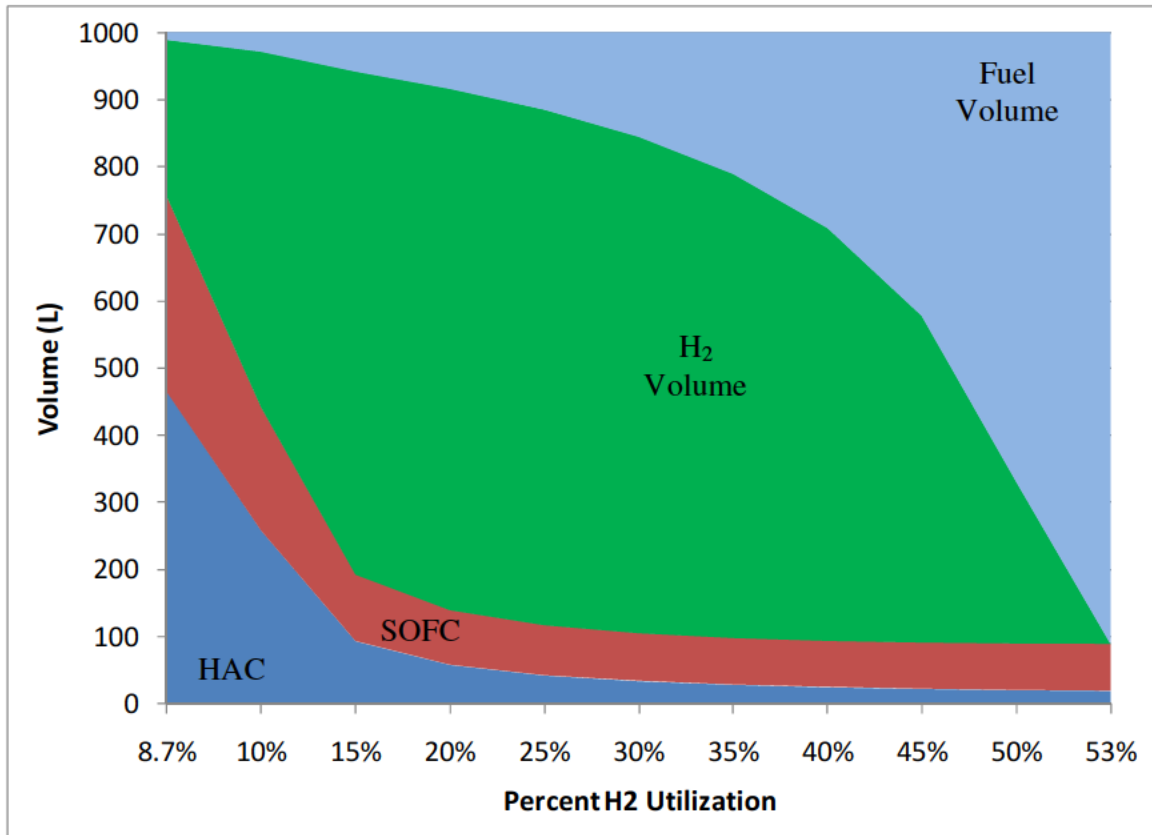


Figure 5-10: Hydrogen storage at 1000 psi volume v. H2 utilization.

5.3.5 Effect of Water-to-Fuel Ratio

The effect of feed water to fuel ratio was investigated for the HAC system in Section “5.2 HAC System Performance”. The effects on the HAC-SOFC system were examined by comparing the optimized ratio to the HS design ratio used as the starting point for that analysis. Figure 5-11 shows the results of this comparison at a depth of 10 ft. and hydrogen storage at 1000 psi. The optimized ratio delivers significantly improved performance over the HS ratio at low utilizations. This is a result of the expected improvement in HAC performance. For the HS ratio, energy density dips at 1-2% utilization as a result of poor SOFC operation due to low operating temperature. At higher utilizations the SOFC produces enough heat to sustain more efficient operation.

This dip is not seen for the optimized ratio because the anode flow into the SOFC is at a higher temperature. At full utilization, the difference between the two ratios is negligible.

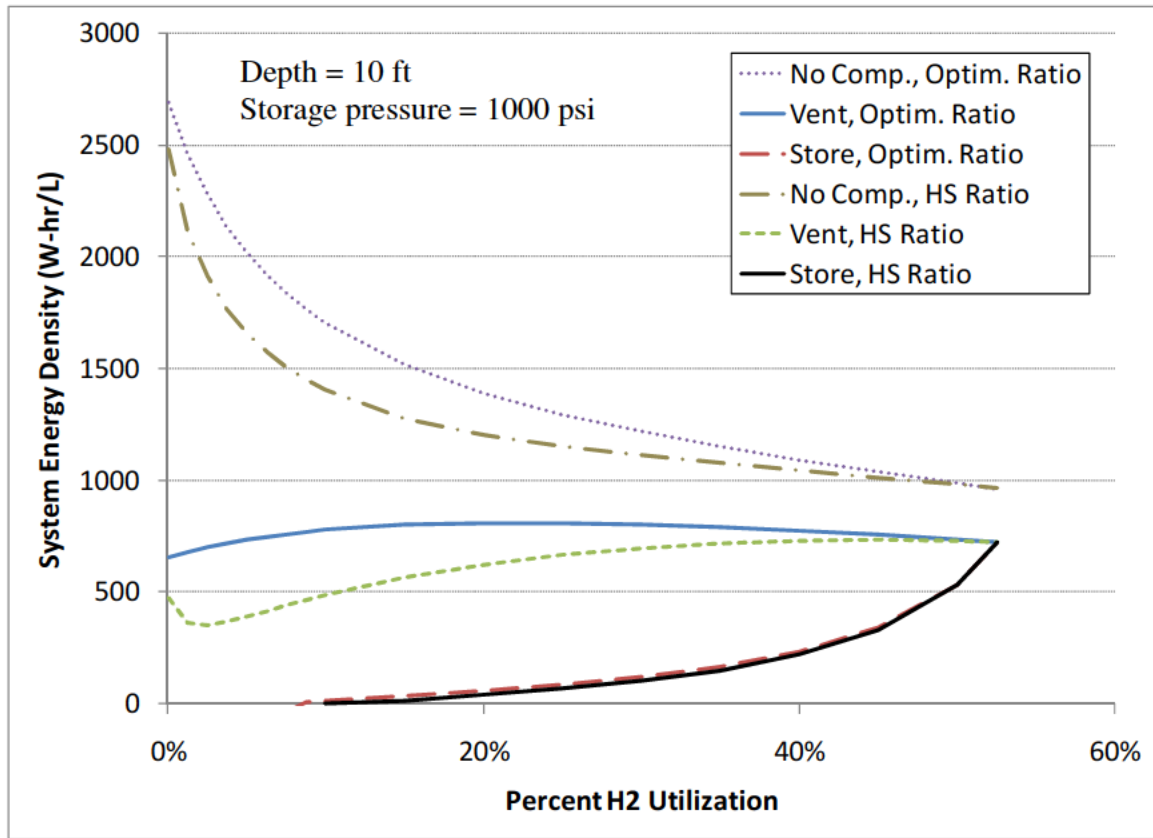


Figure 5-11: Comparison of optimized water-to-fuel ratio to HS value.

The influence of H₂ utilization on SOFC temperature is illustrated in Figure 5-12 for both water-to-fuel ratios. Temperature increases with utilization in both cases, but the temperature associated with the optimized ratio is always higher because the temperature of the incoming flow is higher. At low utilizations, the original water-to-fuel ratio leads to temperatures that are well below ordinary SOFC operating temperatures and the result is very poor SOFC performance. In contrast, the optimized ratio always produces temperatures > 700°C which allows efficient operation over the full range of H₂ utilizations. However, at ‘full’ utilization, the stack temperature exceeds 1100°C, a threshold beyond which cooling may be required. Therefore at high utilization, it may be

necessary to provide cooling or increase the water-to-fuel ratio to prevent the stack from overheating.

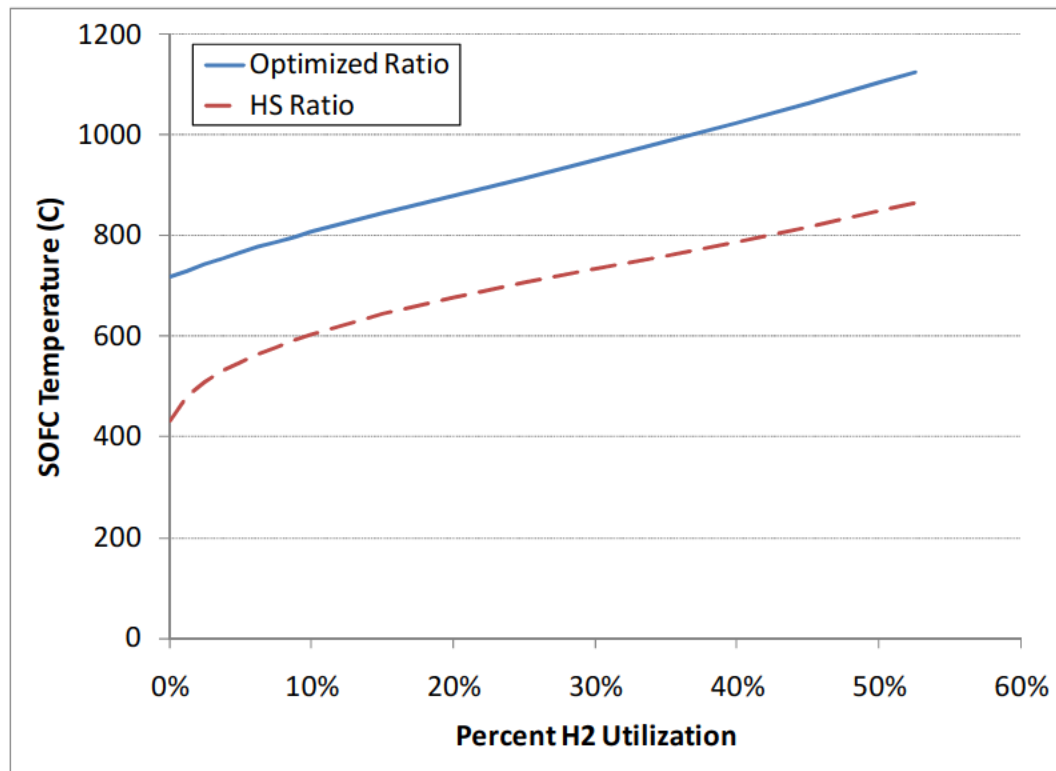


Figure 5-12: SOFC operating temperature v. hydrogen utilization.

5.3.6 Effect of Depth

The effects of increasing vehicle depth were analyzed for the HAC-SOFC with hydrogen venting and hydrogen storage using adiabatic compression. The results are shown in Figure 5-13. The red curve represents the H₂ storage case which was found to be essentially independent of depth. This is expected because storage work is not a function of depth and the work to pump in ambient water is small relative to other factors. The blue curve represents venting at a depth of 10 ft. and corresponds to the same condition as the blue curve in Figure 5-7. As depth is increased, the ambient water pressure around the vehicle increases. More work is required to raise the hydrogen pressure which causes

the system energy density to drop off steeply at greater depths. At 0% hydrogen utilization and 500 ft depth, the cycle is in fact not thermodynamically viable. The losses at this condition exceed the turbine power produced. At 53% utilization the system becomes nearly depth independent and the different depth curves converge. With no excess hydrogen, venting is not required so the ambient depth pressure is unimportant. What the figure clearly illustrates is the value of the fuel cell at greater depths. By neutralizing the impact of depth, the fuel cell improves performance and makes the vehicle far more versatile.

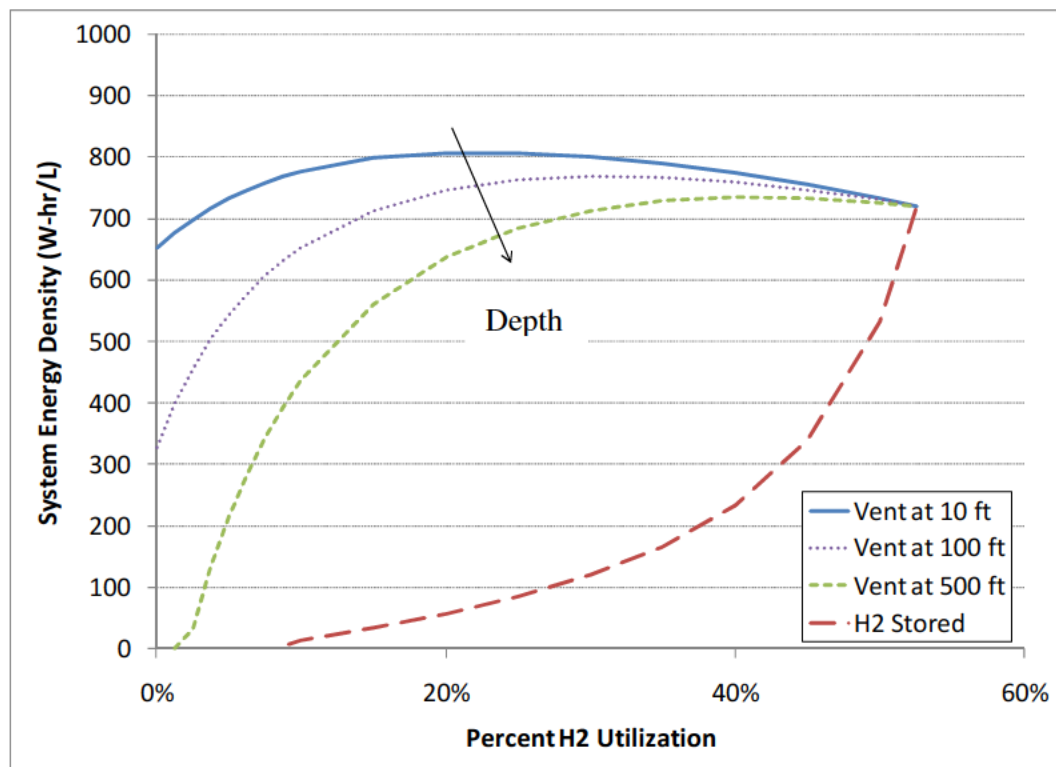


Figure 5-13: Variable vehicle depth, HAC-SOFC energy density.

5.3.7 Effect of Turbine Pressure Ratio

The effect of reducing turbine pressure ratio was investigated over the range of H₂ utilizations. Reducing the pressure ratio of course decreases the work out of the turbine,

but it also decreases the work required to compress the hydrogen by keeping its pressure higher leaving the turbine. Figure 5-14 shows the comparison between pressure ratios of 70, 50, and 30 across the turbine. Clearly, the reduced pressure ratio has a favorable impact on HAC performance. When excess hydrogen is vented, there is a significant performance advantage associated with decreased turbine pressure ratio at low H_2 utilization. This makes sense because the turbine and compressors have inefficiencies that make expanding and recompressing the hydrogen a wasteful process. The impact is minimized at high utilization where the amount of hydrogen to compress is small. The effect is difficult to discern on the figure when the hydrogen is stored instead of vented. This is because at low utilizations, where the impact is strongest, the energy density is very low due to a lack of fuel storage volume.

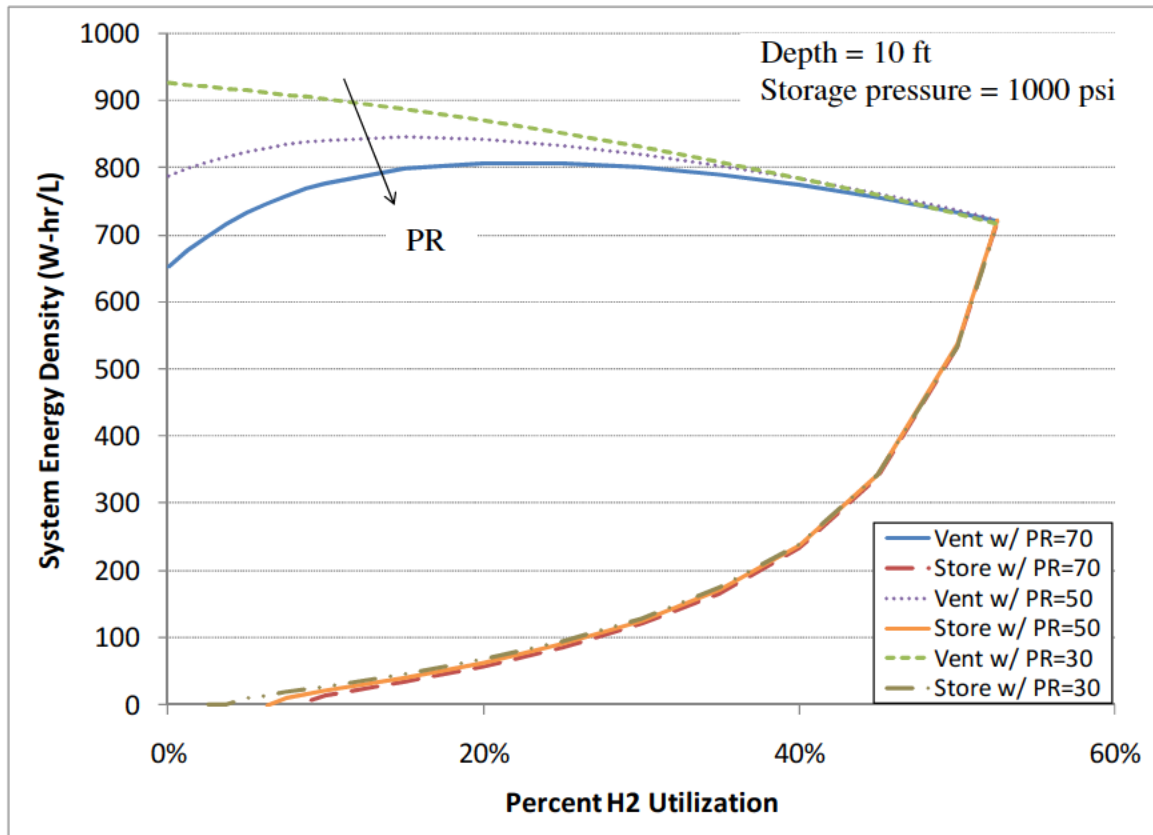


Figure 5-14: Effect of turbine pressure ratio on HAC-SOFC energy density.

5.3.8 Effect of Power Requirement

The system was also investigated for a range of net power requirements. The cases of hydrogen venting and hydrogen storage are treated in this analysis. The model is run at 5, 15, and 25 kW net output over the 0-53% utilization range. The results of this analysis are found in Figure 5-15. As expected, increasing the power output decreases system energy density. The baseline 15 kW output case is shown in blue and red, for venting and storing respectively. Clearly, reducing to 5 kW provides significant improvement and increasing to 25 kW incurs a significant penalty. In the model, this effect occurs because of the scaling of system components to meet the power demands. To produce more power, the components must all become larger which leaves less and less volume for fuel storage. Therefore, increased power system size and the consequent reduction in fuel storage is the primary factor driving down energy density.

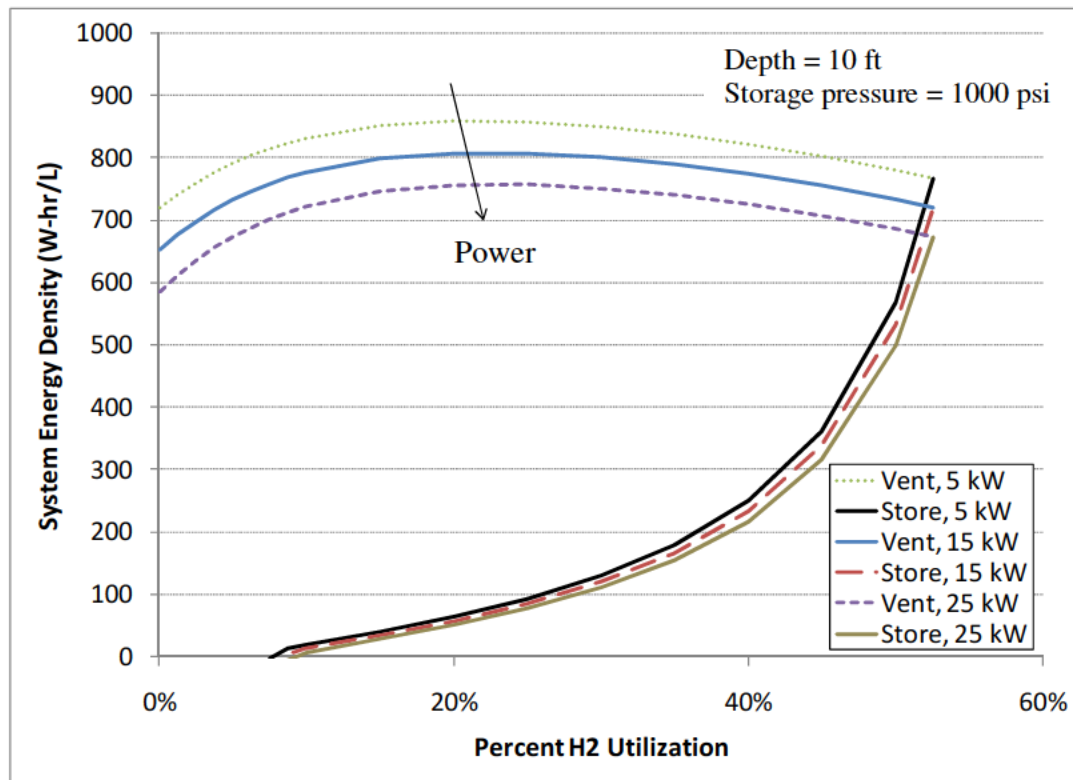


Figure 5-15: Variable power requirement, HAC-SOFC energy density.

5.3.9 Effects of Component Performance Improvements

The impact of various component improvements was investigated over the range of H₂ utilizations. Compressor efficiency, turbine efficiency, and aluminum seed ratio are separately improved by 10% of baseline values to determine the performance impact.

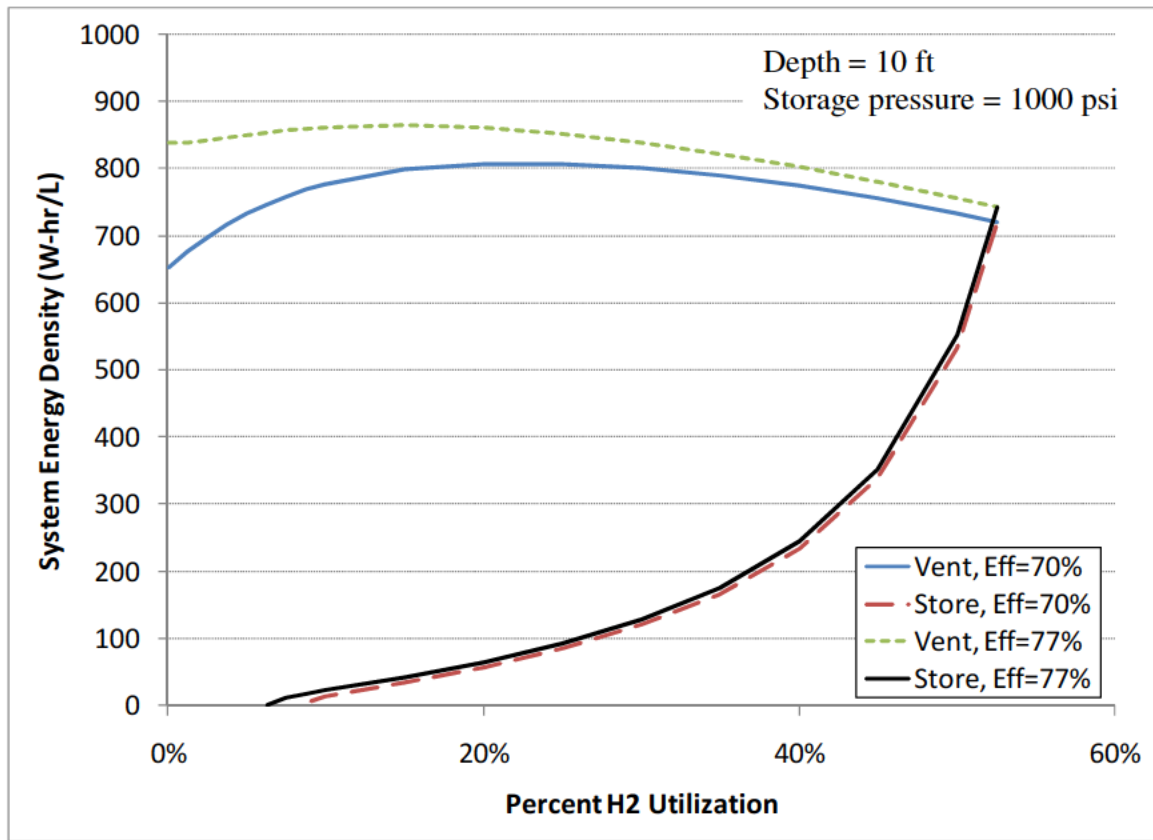


Figure 5-16: Improved compressor efficiency, HAC-SOFC energy density.

Figure 5-16 shows the results for compressor efficiency improvement. As expected, improving the efficiency provides a significant boost to energy density. The compressor improvement has its largest impact at low H₂ utilizations because there is more gas to compress at those conditions. In the figure it can be seen how for hydrogen venting the effect is smaller at high utilization, but the improvement is still significant even at 53% utilization. The improvement is still present, but less noticeable when hydrogen is stored.

As seen for reduced turbine pressure ratio in Figure 5-14, the effect at low utilization is hidden because the energy density is so poor to begin with.

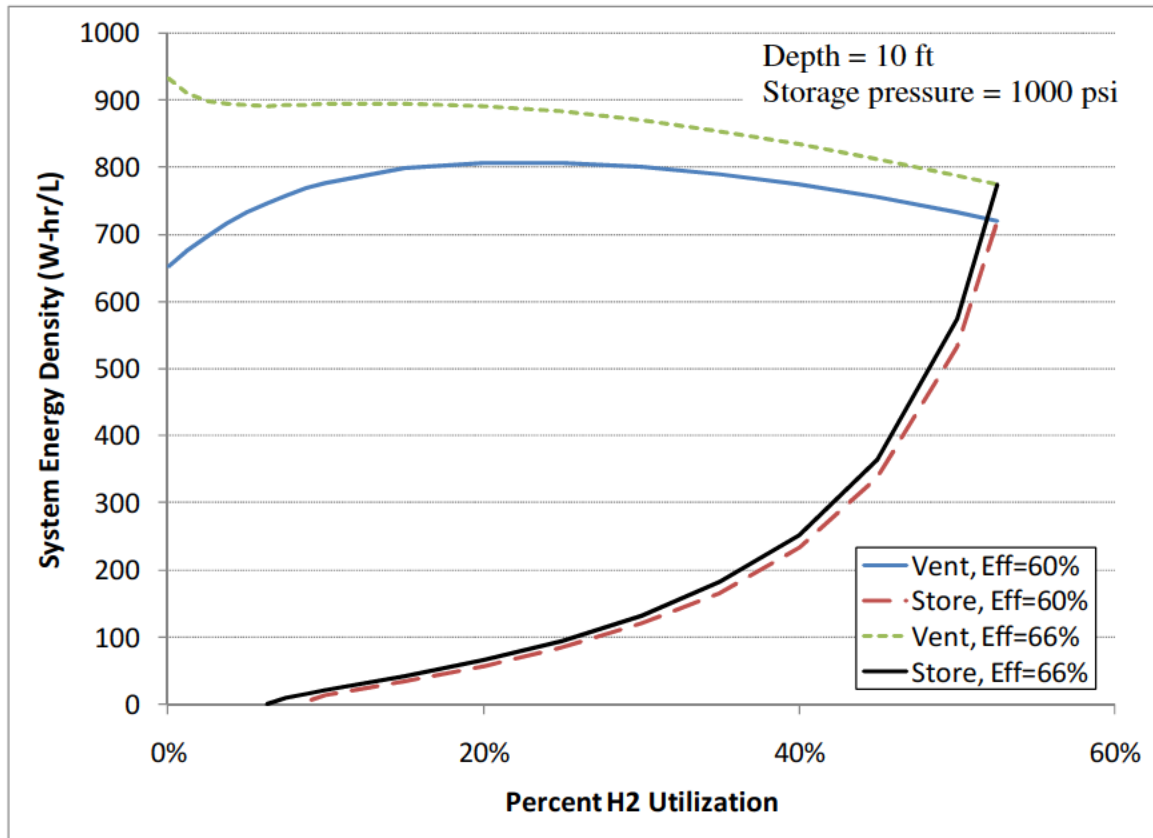


Figure 5-17: Improved turbine efficiency, HAC-SOFC energy density.

Figure 5-17 shows the results for turbine efficiency improvement. As with the compressor, improving the turbine provides a significant boost to energy density. Similarly, the impact is strongest at low utilizations. In contrast to the compressor improvement analysis, the relative improvement in energy density due to increased turbine efficiency drops off less strongly at high utilization. This owes to the differing roles of the turbine and compressors in the cycle. As stated above, as utilization rises the amount of hydrogen to compress decreases which is the primary driver for improvement seen in Figure 5-16. High utilization also decreases the total mass flow through the HAC portion of the system as the SOFC provides a larger fraction of the power. However, if

HAC mass flow is decreased by 50% (for example) at full utilization, the mass of hydrogen compressed will decrease by around 75%. This explains why more of the turbine improvement is retained at high utilization. Once again, improvements for the hydrogen storage case are more difficult to discern because energy densities are so low.

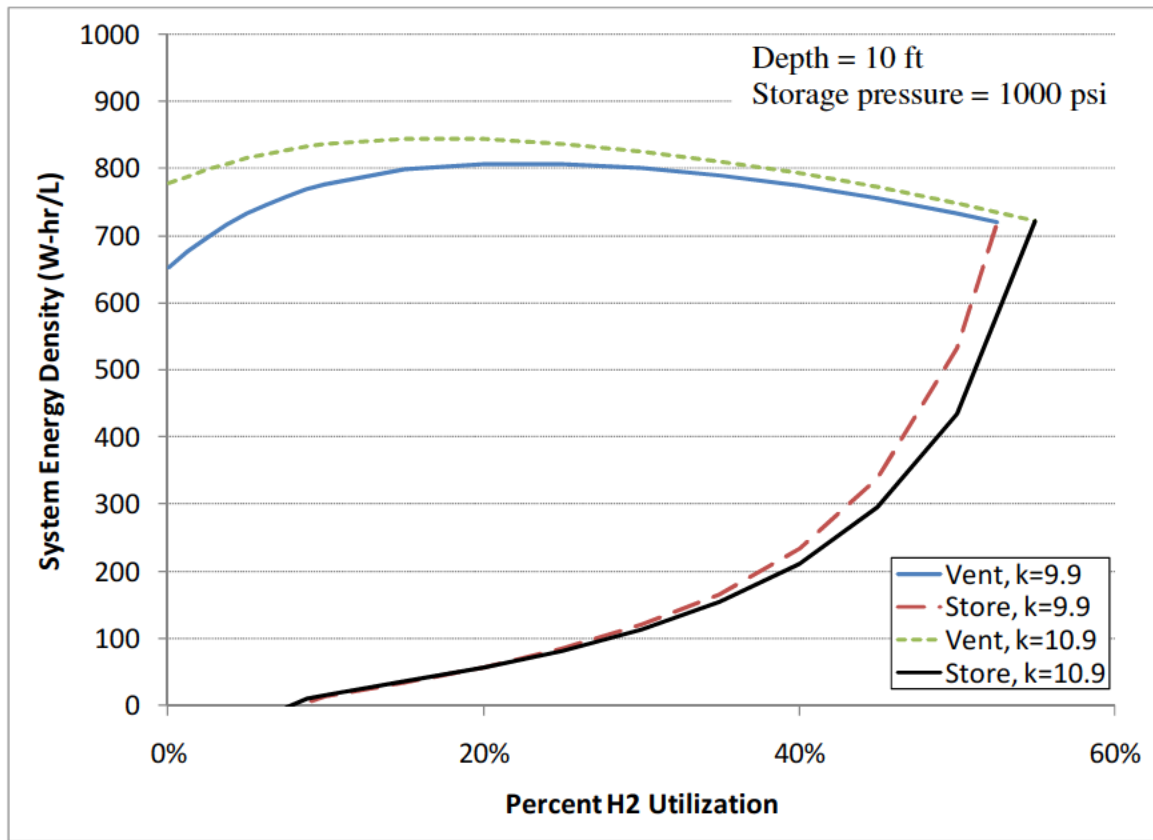


Figure 5-18: Improved seed ratio, HAC-SOFC energy density.

Increasing the seed ratio of the fuel seeder can also provide performance improvements, but it has a somewhat more complex effect on the system. As seen in Figure 5-18, increasing the seed ratio increases the maximum allowable H₂ utilization for sustained operation. Increased seed ratio essentially decreases the amount of seed hydrogen for the same amount of fuel which means that the hydrogen that must be recycled is a smaller fraction of the total. It is very important to note, however, that “full” utilization is a larger

fraction of the total at a higher seed ratio, but the actual amount of hydrogen consumed in the SOFC is the same (all other factors being equal).

In Figure 5-18, the improvement for the hydrogen venting case is obvious especially at low utilization. The improvement results from decreasing the amount of H_2 that must be recirculated, and therefore has less impact when the HAC portion of the system is smaller (i.e. at high H_2 utilization). Also, reducing the amount of seeding hydrogen degrades SOFC performance because the fraction of hydrogen in the anode flow is reduced. At first glance, it appears that energy density is decreased for the hydrogen storage case, but this is an artifact of plotting against utilization as a percentage and not an absolute value. In fact, there is little change in performance for the hydrogen storage case.

5.3.10 Effect of SOFC Scaling

There is a significant degree of uncertainty in the approximation that the SOFC support structure (piping, wiring, etc.) will scale as twice the volume of the SOFC stack alone. As such, it is appropriate to consider the effect of this approximation. The baseline assumption has been compared to the alternate cases of support structure scaling equal to stack volume and three times the stack volume. The results of this analysis are plotted in Figure 5-19. As expected, decreasing the scaling factor raises system energy density because more volume is available for fuel storage. There is no effect at 0% utilization because the SOFC is not present. The figure illustrates that the manner of SOFC scaling is important, but the sensitivity of the system energy density to this parameter is less than that of most other parameters studied in this work.

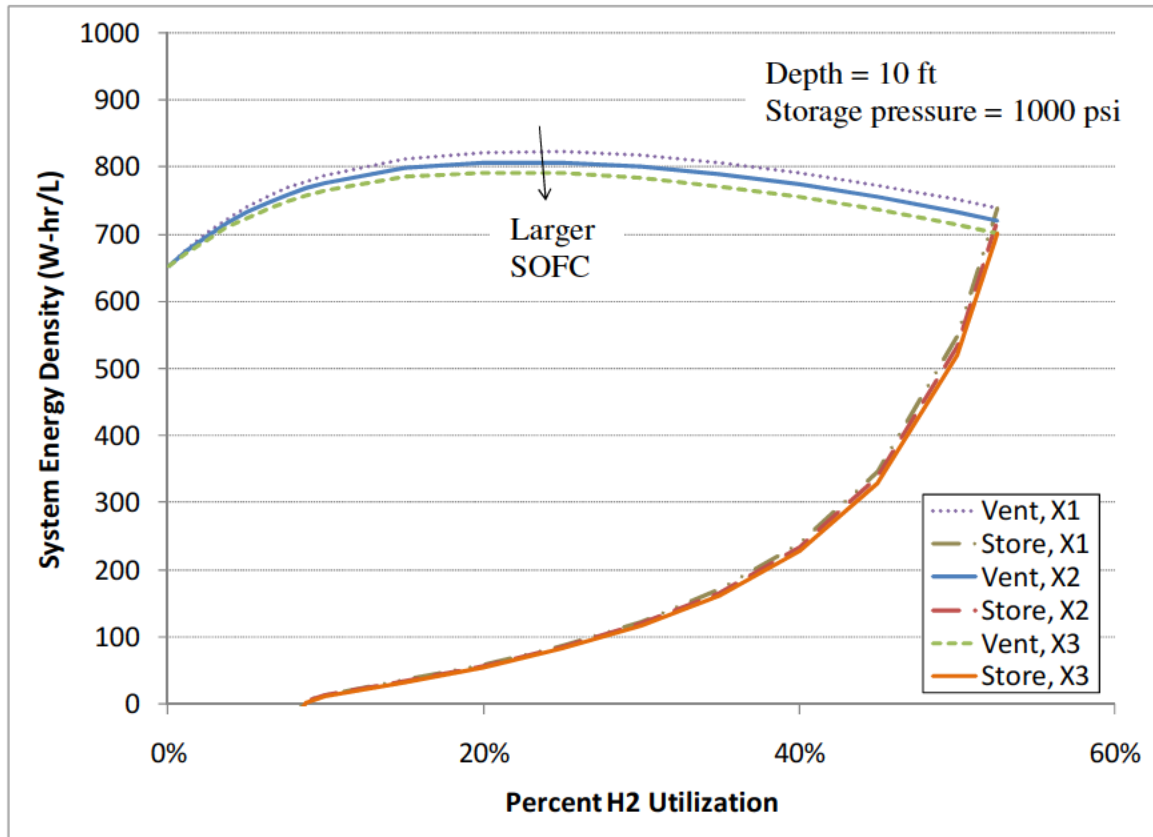


Figure 5-19: Variable SOFC scaling, HAC-SOFC energy density.

5.3.11 Effects of Heat Rejection During Compression

The present work has assumed adiabatic compression of the hydrogen gas. Of course, no compression process is truly adiabatic and it is possible that the compression would be better modeled assuming heat removal. This would have the effect of reducing the amount of work required to compress the hydrogen. Most real compressors are most closely approximated by a polytropic processes. However, the underwater environment is unique for the ample availability of cooling water, and therefore a nearly isothermal compression process could be possible. Figure 5-20 compares the energy densities of systems with adiabatic and isothermal compression. The adiabatic process is performed at 70% isentropic efficiency, and the isothermal process at 70% isothermal efficiency.

Clearly, the isothermal case performs much better than the adiabatic case. The pure HAC system (0% utilization) shows better than 150% energy density improvement when the hydrogen is vented. Additionally, the hydrogen storage case shows a positive energy density for the pure HAC system with isothermal compression. The improvement is less dramatic at full utilization, but there is still a 19% improvement in system energy density. This suggests that an optimum system design should operate the compressors as near to isothermal as possible.

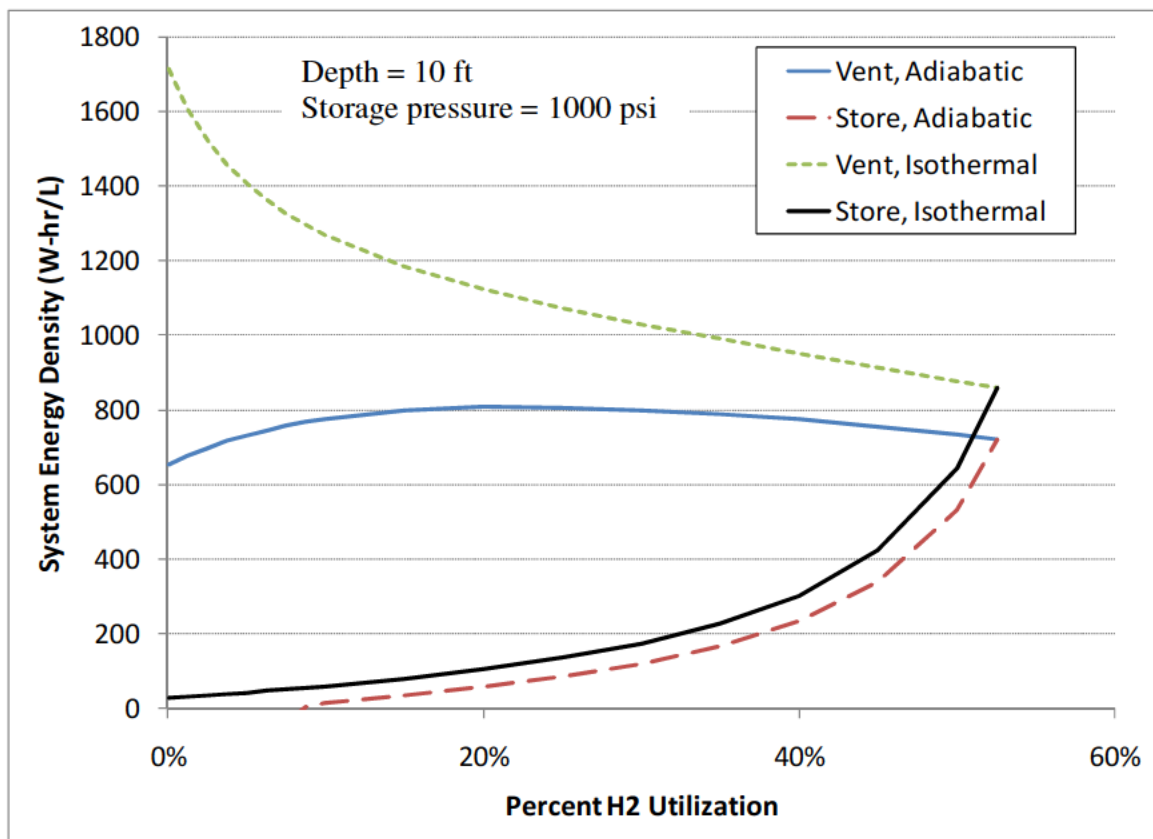


Figure 5-20: Adiabatic and isothermal compression, HAC-SOFC energy density.

5.3.12 Combined Performance Improvement

All of the improvements discussed above can be combined to give an idea of what kind of performance could be possible in this type of system as the relevant technologies are

advanced. The HAC-SOFC model was run for the low power, high efficiency condition detailed in Table 5-1.

Table 5-1: Baseline v. improvements comparison

	Baseline	Improved
Depth	10 ft	10 ft
Net Power	15 kW	5 kW
η_{Turbine}	60%	66%
PR_{Turbine}	70	30
$\eta_{\text{Compressor}}$	70%	77%
Compression	Adiabatic	Isothermal
k_{Seed}	9.9	10.9

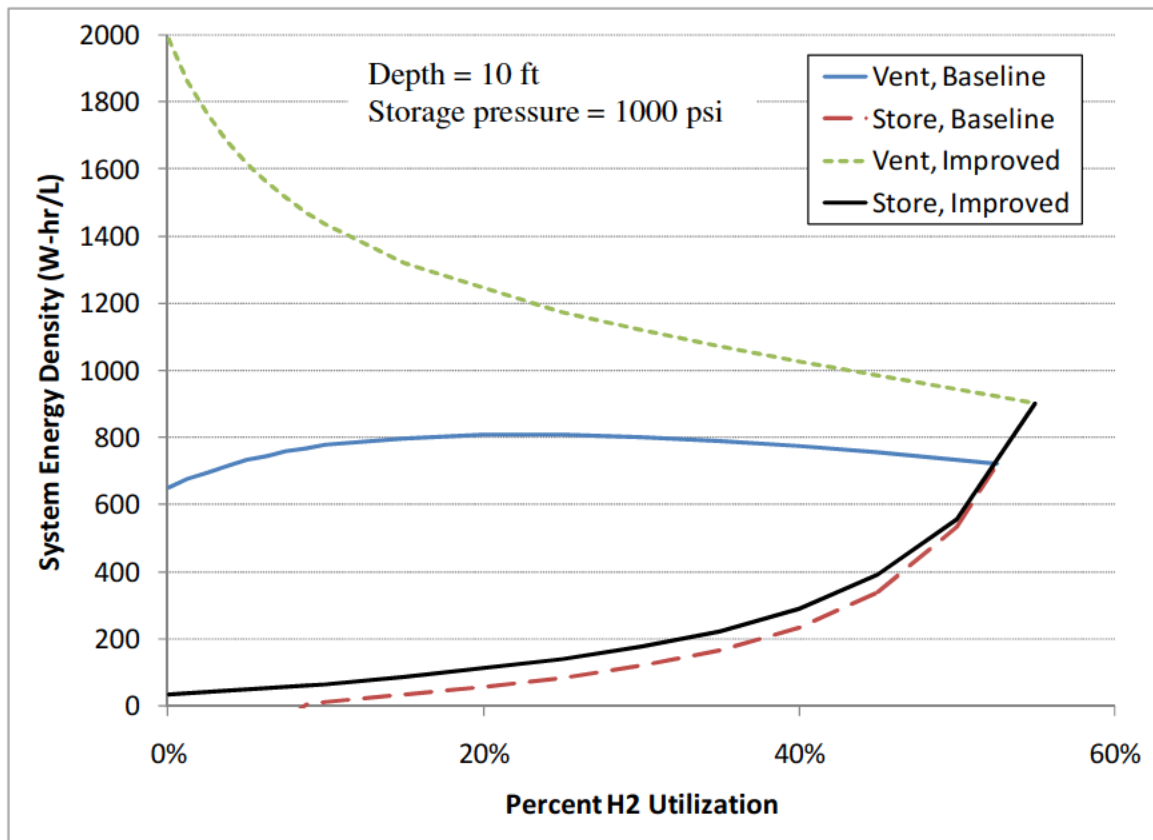


Figure 5-21: Combined improvements, HAC-SOFC energy density.

Figure 5-21 illustrates the results of the analysis. For the base HAC system with no SOFC, these improvements can provide a three-fold increase in energy density. At “full” utilization, a less dramatic but still highly valuable increase in energy density is possible

at over 25%. Note how adding the improvements fundamentally alters the shape of the H₂ venting curve. The baseline case improves initially as load is shifted to the SOFC and peaks at around 25% utilization. Full utilization performance exceeds the 0% utilization performance. In contrast, the improved case has consistently worse performance as utilization rises. This is because the improvements make the HAC system so efficient and energy dense that using an SOFC actually decreases performance. Of course, corresponding advances in fuel cell technology could potentially sway that balance back in favor of a hybrid system. Additionally, in the event that venting the hydrogen is not possible for mission related reasons, the hybrid system at full utilization still offers far superior performance to the hydrogen compression case.

5.4 Aluminum-H₂O₂ Combustor Performance

The aluminum with oxidizer system (see Figure 3-4) was analyzed at the same conditions as the HAC-SOFC system where applicable, with the additional constraint that the temperature leaving the combustor matches the same from the HAC-SOFC model. The power output is set equal to 15 kW and the fuel flow is scaled accordingly rather than trying to draw conclusions using the same aluminum flow in the different system. Because this system has no excess gaseous components to account for, the types of analysis used on the HAC-SOFC system are not relevant. The single operating point simulation results yielded the following:

$$ED_v = 457 \text{ W} \cdot \text{hr}/L$$

5.5 Hydrocarbon Fueled Combustor Performance

The hydrocarbon fueled system (see Figure 3-5) was analyzed using the same constraints as the aluminum-oxidizer system. The turbine power was set to 15 kW in order to give results analogous to the HAC, HAC-SOFC, and Al-H₂O₂ systems. Of course in this model, a gaseous byproduct is produced that must be handled as with the HAC system. In this case the gas is carbon dioxide instead of hydrogen, which is important because hydrogen requires much more work to compress on a per mass basis. The energy density of this system has been estimated for both a CO₂ storage case and a CO₂ venting case, much like the analysis of the HAC-SOFC system.

With CO₂ storage: $ED_v = 119 \text{ W} \cdot \text{hr}/L$

With CO₂ venting: $ED_v = 326 \text{ W} \cdot \text{hr}/L$

5.6 Performance Comparison

For reasons discussed in the previous chapters, the relative performance of various UUV power systems is best compared using the volumetric energy density. Figure 5-22 compares the energy density of the HAC, HAC-SOFC, Al-H₂O₂, and hydrocarbon combustor systems investigated in this work. The figure also includes energy density estimates for SOFC, lithium-ion, and alkaline battery systems for UUVs based on several references. The alkaline battery energy density value corresponds to the array of D cell batteries that has already been implemented in the Seahorse UUV [40]. The SOFC and Li-ion ‘error’ bars represent approximate ranges of what could be expected based on references [38] [41] [5]. The value represented for the HAC, HAC-SOFC, Al-H₂O₂, and hydrocarbon systems is the energy density using the baseline assumptions described

throughout this work. The lower value range bars indicate a potential 10% decrease in performance due to losses (piping, heat losses, etc.) that are beyond the scope of the present work. The upper value range bars for HAC and HAC-SOFC systems represent the performance based on the possible improvements described in Section “5.3.12 Combined Performance Improvement”.

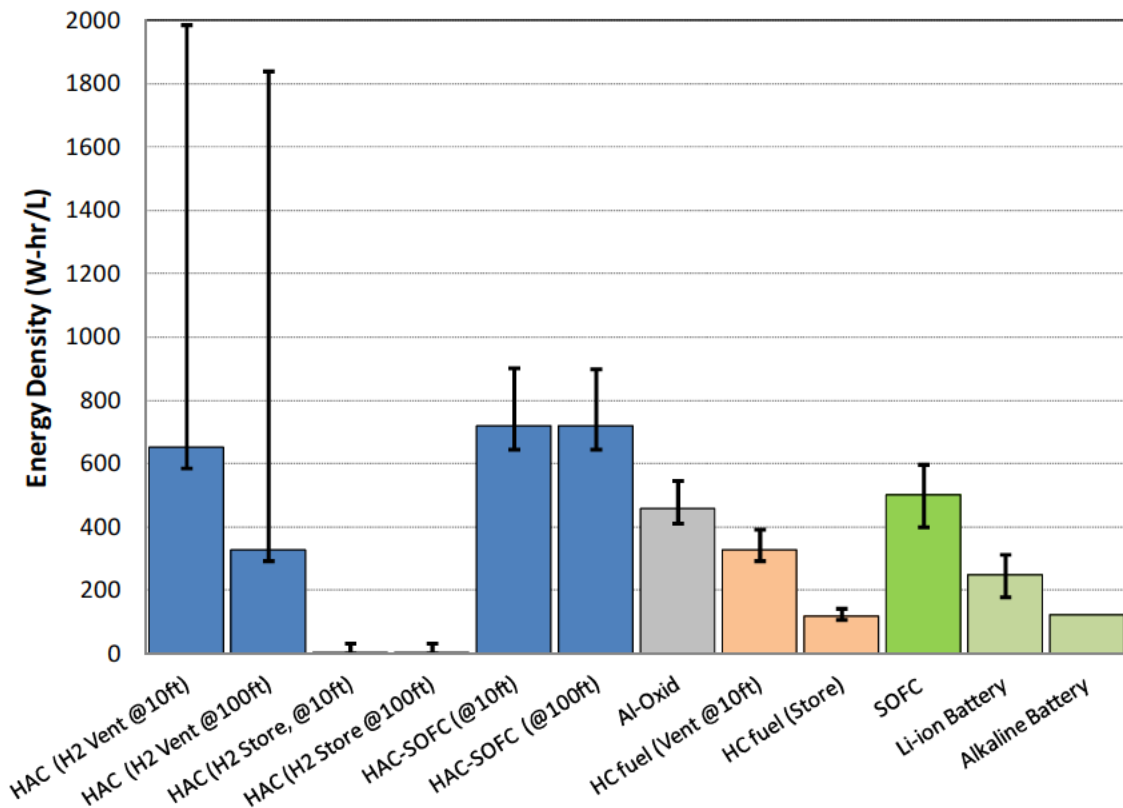


Figure 5-22: Bar graph of energy density of various technologies.

It is estimated that the HAC system with hydrogen venting can achieve at least a four-fold increase in energy density over the alkaline cells. This could increase to ten- or fifteen-fold with all of the improvements that have been discussed. The HAC system with hydrogen storage has extremely low energy density making it an undesirable option. The HAC-SOFC system that totally consumes the hydrogen gas (i.e. “full” utilization) could offer a five- to seven-fold increase in range over alkaline batteries. It is clear from Figure

5-22 that the choice between HAC with hydrogen venting and HAC-SOFC strongly depends on the level of advancement of the HAC components. It is also clear that if venting is not permitted, HAC-SOFC is far superior to HAC with hydrogen compression.

The Al-H₂O₂ and hydrocarbon combustor systems both offer relatively good performance. They could offer energy densities in the range of three to five times that of alkaline batteries. Developing an operational Al-H₂O₂ system would have most of the same challenges as an HAC system, but Al-H₂O₂ cannot likely reach the same levels of energy density as the HAC or HAC-SOFC could. A hydrocarbon fueled system may not offer the highest energy density increases but it would have the advantage of utilizing relatively well developed technologies.

Chapter 6: Conclusions and Future Work

6.1 Conclusions

A versatile and valuable tool for the thermodynamic analysis of unmanned undersea vehicle (UUV) propulsion systems has been developed using the NPSS framework. Building on earlier efforts to characterize the hybrid aluminum combustor (HAC) concept, a numerical model has been developed which is used to estimate performance over a wide range of operating conditions. The model has been expanded to fully account for important parasitic losses in the system, most importantly the work required to recycle the seeding hydrogen and to vent or store the excess hydrogen. Earlier efforts had neglected this work and therefore significantly overestimated the power output and efficiency of the HAC system cycle. Analysis of the improved HAC model has shown that the ratio of feed water to aluminum fuel is the key operating parameter for maximizing efficiency.

A scaling law was developed to approximate changes in the size of the HAC components. An efficient method for estimating the total volume of the HAC over a wide range of conditions was implemented by making basic assumptions about component operation. This volume estimation permits calculation of the volumetric energy density that is used to evaluate performance. This represents a significant advance over earlier analyses which only consider power output and efficiency.

A detailed NPSS model of a solid oxide fuel cell (SOFC) has also been developed and tested. The SOFC model incorporates a thorough accounting of electrochemical

processes including the Nernst potential and relevant overpotentials. The SOFC has been combined with the HAC to form a model of a proposed HAC-SOFC hybrid system. The versatility of the simulation tool has been demonstrated by evaluating a wide variety of system variations. An analysis of performance trends has demonstrated the effects of depth, turbine pressure ratio, power requirement, and various component efficiencies.

Running the model over a range of H_2 utilizations has revealed important information about optimizing the system. Specifically, it has revealed the strengths and liabilities of hydrogen venting, storage, and consumption in the fuel cell. One of the things we have learned from this modeling effort is that it is always more effective from a volumetric energy density standpoint to vent any excess hydrogen as opposed to storing it. This is because the hydrogen storage tanks displace large amounts of fuel. Therefore, when excess hydrogen is present one should always vent, not store, as long as stealth is not a priority. Likewise, consuming all of the excess hydrogen in the fuel cell of the HAC-SOFC is always more effective than storing it when venting is not permitted. Therefore, it can be definitively stated that when stealth is necessary the HAC-SOFC at “full” utilization is the best option. When stealth is not important, deciding between HAC with H_2 venting and HAC-SOFC depends on many factors. It has been shown that given the baseline assumptions, HAC-SOFC at approximately 25% hydrogen utilization offers the highest energy density. However, this has the drawback of increasing complexity without increasing stealth. Using the baseline assumptions, the HAC-SOFC at full utilization outperforms the HAC with hydrogen venting. It has also been shown that for the “improved” system HAC with venting is best. The biggest contributor is the ability to

perform the hydrogen compression isothermally which would more than double the HAC system energy density relative to the baseline version. A definitive answer requires further development of physical components to provide more confident estimates of parameters (e.g. turbine efficiency, seed ratio, etc.), but the tools developed in this work can provide guidance to that research and are easily adaptable to provide improved performance estimates with improved information.

Summary of key contributions:

- Demonstrated the utility of NPSS as a tool for predicting underwater propulsion system performance and addressing optimization questions.
- Developed methods for scaling component volumes that are useful for making system energy density estimates that are relevant to the underwater propulsion community.
- Developed a library of customized NPSS modules for underwater applications.
- Developed and demonstrated an NPSS module to represent a solid oxide fuel cell.
- Showed that a Rankine cycle power/energy system based on the combustion of aluminum powder in sea water can achieve energy densities 4 to 15 times better than current battery-based technologies if hydrogen venting is permissible.
- Showed that a power/energy system consisting of an aluminum-seawater combustion-powered Rankine cycle plus a fuel cell can achieve energy densities approximately 5 to 7 times greater than current battery-based technologies if hydrogen venting is not permissible.

- Showed that if hydrogen venting is not permissible, compressing and storing it on board is not practical and some other means must be developed to deal with it.
- Investigated the effect of fuel cell current density, vehicle depth, turbine pressure ratio, turbine efficiency, power requirement, and compressor efficiency on the performance of an aluminum-seawater Rankine cycle power system with integrated fuel cell.

6.2 Future Work

There are several areas for continuing work that can be addressed in the future. As discussed above, improved estimates of component performance in the future will allow the model to be refined for improved system performance calculations. Component data could potentially come from the building and testing hardware or from higher fidelity simulations. NPSS is capable of directly incorporating high fidelity models, or the models could be used to estimate performance and loss parameters.

The current work has focused on the simple volumetric energy density of negatively buoyant systems. Future work could focus on *neutral buoyancy* energy density, which accounts for the additional volume of empty space required to make the system neutrally buoyant. This may require refined estimates of how mass scales with system volume.

Different fuel cell types and configurations should be investigated. Including an SOFC immediately downstream from the turbine was an obvious choice due to the temperature. However, other options could certainly be viable. Low temperature fuel cells could be

installed downstream from the heat exchanger or they could operate directly from a recycled feed of hydrogen like the fuel seeder. Alkaline fuel cells in particular have been discussed, and preliminary work on incorporating an AFC has already begun.

All of the work presented here has been design point oriented analysis. To truly evaluate the suitability of a power system for UUV applications, off-design performance must be determined. The main impediment preventing this analysis is the lack of turbine and compressor map performance data. These maps are highly specific to a particular piece of hardware and are difficult to generalize. However, without that data it is impossible to do an accurate off-design analysis as flow rates, pressures, and temperatures vary at the turbine and compressors. Resolving this issue would allow immediate off-design calculations with only slight modifications to the existing models.

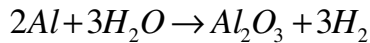
Work should also continue on developing and generalizing the NPSS design tool. There is a significant need in the UUV research community for efficient means of estimating system energy densities. Comparing the value of different systems is presently difficult due to the challenges associated with these estimates. A valuable and versatile research tool could be developed by expanding the current tool to easily accommodate these system level analyses for various types of heat engine and fuel cell arrangements.

Appendix A:

Fuel Energy Content Calculations

The energy content of fuel-oxidizers combinations (see Table 1-2 and Table 1-3) has been calculated using the balanced chemical reactions and the standard enthalpy of formation of reactants and products. An example calculation is shown below. The energy content of each reaction was calculated using this procedure.

Reaction:



Species name (phase)	Standard enthalpy of formation (kJ/mol)	MW (g/mol)	Density (kg/L)
Aluminum (solid)	0	26.98	2.7
Water (liquid)	-285.8	18.0153	1
Alumina (solid)	-1675.7	101.96	~ 4
Hydrogen (gas)	0	2.0159	8.99e-5 (@ STP)

Energy release of balanced reaction:

$$1 \cdot (-1675.7 \text{ kJ/mol}) + 3 \cdot (0 \text{ kJ/mol}) - 2 \cdot (0 \text{ kJ/mol}) - 3 \cdot (-285.8 \text{ kJ/mol}) = -818.3 \text{ kJ}$$

Per mole of aluminum:

$$(818.3 \text{ kJ}) / (2 \text{ moles}) = 409.15 \text{ kJ/mol}$$

Per mass of aluminum:

$$\frac{(409.15 \text{ kJ/mol})}{(26.98 \text{ g/mol})} \cdot \left(\frac{1 \text{ W} \cdot \text{hr}}{3.6 \text{ kJ}} \right) \cdot \left(\frac{1000 \text{ g}}{1 \text{ kg}} \right) = 4212.48 \text{ W} \cdot \text{hr/kg}$$

Per volume of aluminum:

$$(4212.48 \text{ W} \cdot \text{hr/kg}) \cdot (2.7 \text{ kg/L}) = 11373.7 \text{ W} \cdot \text{hr/L}$$

Appendix B:

Heat Exchanger Scaling Calculations

```

clear; clc;

% initial temperature values do not affect scaling
T_1i=600; T_2i=0;

% initial guess for the parameter, f
f= .001;

count1=0;
% loop through the calculation for different Cp ratios
for Cratio=.05:.15:.95
    count1=count1+1;
    count2=0;
    L= 1; % initial L value
    T1(1)= T_1i; % initial temperature value

    % loop through for different effectiveness
    for eff=.05:.0237:.999
        count2=count2+1;
        T2(1)= T_2i + eff*(T_1i-T_2i)*Cratio; % calculate exit T
        err= 1;

        while abs(err)>0.001
            L= L*(1+ 0.005*err/abs(err)); % iterate L to solve
            dx= L/5000;
            x= 0:dx:L;
            f= .001*(dx/.001); % scale f to the length discretization

            for i=1:(length(x)-1)
                dT(i)= T1(i)-T2(i);
                Q(i)= dT(i)*f;

                T1(i+1)= T1(i)-Q(i);
                T2(i+1)= T2(i)-Cratio*Q(i);
            end

            % calculate the error in exit T
            err= T2(length(x))-T_2i;
        end

        L_vctr(count1,count2)= L;
    end
end

```

Appendix C:

NPSS Details of HAC Model

Order of Execution:

Turbine Path:

1. Loop Start element: MixLoop 'Loop1'
2. Separator element: Separator2 'Sep1'
3. Splitter element: Splitter2 'Split2'
4. Turbine element: Turbine 'T1'

Fuel Feed Path:

5. Flow Start element: FlowStart2 'F1'
6. Fuel Seeder element: Seeder 'Seed1'

Inlet-to-Combustor Path:

7. Loop Start element: MixStart 'Loop2'
8. Heat Exchanger element: HeatExchanger 'HE1'
9. Splitter element: Splitter2 'Split1'
10. Bleed element: Bleed 'B3'
11. Compressor element: Compressor2 'C1'
12. Combustor type Bleed element: Bleed 'PreComb1'
13. Combustor type Bleed element: Bleed 'Comb1'

Water recycle loop:

14. Condenser type Bleed element: Bleed 'Cond1'
15. Separator element: Separator2 'Sep2'
16. Liquid Pump element: LiquidPump 'LP1'
17. Splitter element: Splitter2 'Split4'
18. Flow Start element: FlowStart2 'F8'

19. Water Mixer element: WaterMixer 'WMix1'

20. Liquid Pump element: LiquidPump 'LP2'

Hydrogen compression branch:

21. Splitter element: Splitter2 'Split3'

22. Compressor element: Compressor2 'GasC1'

23. Flow Copy element: FlowCopy 'FC1'

24. Compressor element: Compressor2 'GasC2'

25. Compressor element: Compressor2 'GasC3'

Additional elements:

26. Shaft element: Shaft 'Sh1'

27. Flow End elements: FlowEnd 'E1', 'E3', 'E4', 'E5', 'E6'

Independents:

Complete list of independent variables varied by the system:

Table C-1: HAC system independent variables.

	Variable name	Description	Controlled parameter
1.	Loop1.ind_Pt	Loop1 Exit total pressure, Pt	Loop1.Fl_O.Pt
2.	Loop1.ind_Tt	Loop1 Exit total temperature, Tt	Loop1.Fl_O.Tt
3.	Loop1.ind_W	Loop1 Exit mass flow, \dot{m}	Loop1.Fl_O.W
4.	Loop1.ind_fracOne	Loop1 Exit mass fraction, y_1	Loop1.Fl_O.getTotalComp("H2O")
5.	Loop1.ind_fracTwo	Loop1 Exit mass fraction, y_2	Loop1.Fl_O.getTotalComp("H2")
6.	Loop1.ind_fracThree	Loop1 Exit mass fraction, y_3	Loop1.Fl_O.getTotalComp("AL2O3(a)")
7.	Loop2.ind_fracOne	Loop2 Exit mass fraction, y_1	Loop2.Fl_O.getTotalComp("H2O(L)")
8.	Loop2.ind_fracTwo	Loop2 Exit mass fraction, y_2	Loop2.Fl_O.getTotalComp("AL2O3(a)")
9.	Loop2.ind_fracThree	Loop2 Exit mass fraction, y_3	Loop2.Fl_O.getTotalComp("H2")
10.	Cond_T	Cond1 Exit total temperature, Tt	Cond1.Fl_O.Tt
11.	ColdFlowSplit	Split1 Bypass ratio, BPR	Split1.BPR
12.	HotFlowSplit	Split2 Bypass ratio, BPR	Split2.BPR
13.	HeatEx_eff	HE1 Effectiveness, ϵ	HE1.eff
The following variable is only used if a power output is specified by a dependent condition. (see Dependents list)			
14.	AL_W	F1 Exit mass flow, \dot{m}	F1.Fl_O.W - Indirectly controls Al flow

Dependents:

Complete list of dependent conditions required by the system solver:

Table C-2: HAC system dependent conditions.

Condition name		Condition description/equation
1.	Loop1.dep_Pt	Inlet and outlet total pressure must be equal
		In element Loop1 : $Fl_I.Pt = Fl_O.Pt$
2.	Loop1.dep_Tt	Inlet and outlet total temperature must be equal
		In element Loop1 : $Fl_I.Tt = Fl_O.Tt$
3.	Loop1.dep_W	Inlet and outlet mass flow must be equal
		In element Loop1 : $Fl_I.W = Fl_O.W$
4.	Loop1.dep_fracOne	Inlet and outlet H ₂ O mass flow must be equal
		In element Loop1 : $Fl_I.getTotalComp("H2O") = Fl_O.getTotalComp("H2O")$
5.	Loop1.dep_fracTwo	Inlet and outlet H ₂ mass flow must be equal
		In element Loop1 : $Fl_I.getTotalComp("H2") = Fl_O.getTotalComp("H2")$
6.	Loop1.dep_SumFrac	Sum of mass fractions must equal 1
		In element Loop1 .Fl _ O : $getTotalComp("H2O") + getTotalComp("H2") + getTotalComp("AL2O3(a)") = 1$
7.	Loop2.dep_fracOne	Inlet and outlet liquid H ₂ O mass flow must be equal
		In element Loop2 : $Fl_I.getTotalComp("H2O(L)") = Fl_O.getTotalComp("H2O(L)")$
8.	Loop2.dep_fracTwo	Inlet and outlet Al ₂ O ₃ mass flow must be equal
		In element Loop2 : $Fl_I.getTotalComp("AL2O3(a)") = Fl_O.getTotalComp("AL2O3(a)")$
9.	Loop2.dep_SumFrac	Sum of mass fractions must equal 1
		In element Loop2 .Fl _ O : $getTotalComp("H2O") + getTotalComp("AL2O3(a)") + getTotalComp("H2") = 1$
10.	Loop2.dep_Tt	Inlet and outlet total temperature must be equal
		In element Loop2 : $Fl_I.Tt = Fl_O.Tt$

11.	CombSteam_W	Steam and aluminum mass flow into pre-combustor must be equal
		$C1.Fl_O.W \cdot C1.Fl_O.getTotalComp("H2O") =$ $Seed1.Fl_O.W \cdot \frac{k_{Seed}}{k_{Seed} + 1}$
12.	CombSteam_T	Steam flow into pre-combustor must match target temperature value
		$C1.Fl_O.Tt = \text{Target}$
13.	HEhot_T	Water flow out of the heat exchanger must match target temperature
		$HE1.Fl_O\ 2.Tt = \text{Target}$
The following conditions are used (one at a time only) if fuel flow is varied as an independent. (see Independents list)		
14.	Power0	Net power (not including any H ₂ compression)
		$T1.pwr + C1.pwr + LP1.pwr + LP2.pwr = (\text{Target Power})$
15.	Power2	Net power (including H ₂ seeding and storage compression)
		$T1.pwr + C1.pwr + LP1.pwr + LP2.pwr$ $+ GasC1.pwr + GasC2.pwr = (\text{Target Power})$
16.	Power4	Net power (including H ₂ seeding and venting compression)
		$T1.pwr + C1.pwr + LP1.pwr + LP2.pwr$ $+ GasC1.pwr + GasC3.pwr = (\text{Target Power})$
17.	Power6	Net power (including only H ₂ venting compression)
		$T1.pwr + C1.pwr + LP1.pwr + LP2.pwr$ $+ GasC2.pwr = (\text{Target Power})$

Appendix D:

NPSS Details of HAC-SOFC Model

Order of Execution:

The same order of execution used in the HAC model (see Appendix C) is used for the HAC-SOFC model with the addition of all new elements, in the order described below, inserted immediately following the Turbine ‘T1’ element (#4 in the HAC execution order). The HAC ordering resumes with the Flow Start ‘F1’ element, immediately following the new components.

Turbine Path:

1. Loop Start element: ‘Loop1’
2. Separator element: Separator2 ‘Sep1’
3. Splitter element: Splitter2 ‘Split2’
4. Turbine element: Turbine ‘T1’

SOFC Oxidizer Loop:

5. Flow Start element: FlowStart2 ‘F5’
6. Flow Start element: FlowStart2 ‘F6’
7. Mixture Start element: MixStart ‘MixS1’
8. Loop Start element: MixLoop ‘Loop3’
9. Bleed element: Bleed ‘B4’
10. SOFC element: SolidOxideFC ‘SOFC1’
11. Condenser type Bleed element: Bleed ‘Cond2’
12. Separator element: Separator2 ‘Sep3’
13. Compressor element: Compressor2 ‘GasC4’
14. Liquid Pump element: LiquidPump ‘LP3’

Fuel Feed Path:

15. Flow Start element: FlowStart2 'F1'

16. Fuel Seeder element: Seeder 'Seed1'

Inlet-to-Combustor Path:

17. Loop Start element: MixStart 'Loop2'

18. Heat Exchanger element: HeatExchanger 'HE1'

19. Splitter element: Splitter2 'Split1'

20. Bleed element: Bleed 'B3'

21. Compressor element: Compressor2 'C1'

22. Combustor type Bleed element: Bleed 'PreComb1'

23. Combustor type Bleed element: Bleed 'Comb1'

Water recycle loop:

24. Condenser type Bleed element: Bleed 'Cond1'

25. Separator element: Separator2 'Sep2'

26. Liquid Pump element: LiquidPump 'LP1'

27. Splitter element: Splitter2 'Split4'

28. Flow Start element: FlowStart2 'F8'

29. Water Mixer element: WaterMixer 'WMix1'

30. Liquid Pump element: LiquidPump 'LP2'

Hydrogen compression branch:

31. Splitter element: Splitter2 'Split3'

32. Compressor element: Compressor2 'GasC1'

33. Flow Copy element: FlowCopy 'FC1'

34. Compressor element: Compressor2 'GasC2'

35. Compressor element: Compressor2 'GasC3'

Additional elements:

36. Shaft element: Shaft 'Sh1'

37. Flow End elements: FlowEnd 'E1', 'E2', 'E3', 'E4', 'E5', 'E6'

Independents:

Complete list of independent variables varied by the system:

Table D-1: HAC-SOFC system independent variables.

	Variable name	Description	Controlled parameter
1.	Loop1.ind_Pt	Loop1 Exit total pressure, Pt	Loop1.Fl_O.Pt
2.	Loop1.ind_Tt	Loop1 Exit total temp., Tt	Loop1.Fl_O.Tt
3.	Loop1.ind_W	Loop1 Exit mass flow, \dot{m}	Loop1.Fl_O.W
4.	Loop1.ind_fracOne	Loop1 Exit mass fraction, y_1	Loop1.Fl_O.getTotalComp("H2O")
5.	Loop1.ind_fracTwo	Loop1 Exit mass fraction, y_2	Loop1.Fl_O.getTotalComp("H2")
6.	Loop1.ind_fracThree	Loop1 Exit mass fraction, y_3	Loop1.Fl_O.getTotalComp("AL2O3(a)")
7.	Loop2.ind_fracOne	Loop2 Exit mass fraction, y_1	Loop2.Fl_O.getTotalComp("H2O(L)")
8.	Loop2.ind_fracTwo	Loop2 Exit mass fraction, y_2	Loop2.Fl_O.getTotalComp("AL2O3(a)")
9.	Loop2.ind_fracThree	Loop2 Exit mass fraction, y_3	Loop2.Fl_O.getTotalComp("H2")
10.	Loop3.ind_W	Loop3 Exit mass flow, \dot{m}	Loop3.Fl_O.W
11.	Cond_T	Cond1 Exit total temp., Tt	Cond1.Fl_O.Tt
12.	ColdFlowSplit	Split1 Bypass ratio, BPR	Split1.BPR
13.	HotFlowSplit	Split2 Bypass ratio, BPR	Split2.BPR
14.	HeatEx_eff	HE1 Effectiveness, ϵ	HE1.eff
15.	SOFC1.CathodeActLoss	SOFC1 Cathode activation loss	SOFC1.voltLossActivCathode
16.	SOFC1.AnodeActLoss	SOFC1 Anode activation loss	SOFC1.voltLossActivAnode
17.	SOFC1.SOFC_T	SOFC1 Cell total temp., Tt	SOFC1.Temp
The following variable is only used if a power output is specified by a dependent condition. (see Dependents list)			
18.	AL_W	F1 Exit mass flow, \dot{m}	F1.Fl_O.W - Indirectly controls Al flow
19.	FC_h2ut	SOFC1 H ₂ utilization percent	SOFC1.pctH2util

Dependents:

Complete list of dependent conditions required by the system solver:

Table D-2: HAC-SOFC system dependent conditions.

Condition name		Condition description/equation
1.	Loop1.dep_Pt	Inlet and outlet total pressure must be equal
		In element Loop1 : $Fl_I.Pt = Fl_O.Pt$
2.	Loop1.dep_Tt	Inlet and outlet total temperature must be equal
		In element Loop1 : $Fl_I.Tt = Fl_O.Tt$
3.	Loop1.dep_W	Inlet and outlet mass flow must be equal
		In element Loop1 : $Fl_I.W = Fl_O.W$
4.	Loop1.dep_fracOne	Inlet and outlet H ₂ O mass flow must be equal
		In element Loop1 : $Fl_I.getTotalComp("H2O") = Fl_O.getTotalComp("H2O")$
5.	Loop1.dep_fracTwo	Inlet and outlet H ₂ mass flow must be equal
		In element Loop1 : $Fl_I.getTotalComp("H2") = Fl_O.getTotalComp("H2")$
6.	Loop1.dep_SumFrac	Sum of mass fractions must equal 1
		In element Loop1 .Fl _ O : $getTotalComp("H2O") + getTotalComp("H2") + getTotalComp("AL2O3(a)") = 1$
7.	Loop2.dep_fracOne	Inlet and outlet liquid H ₂ O mass flow must be equal
		In element Loop2 : $Fl_I.getTotalComp("H2O(L)") = Fl_O.getTotalComp("H2O(L)")$
8.	Loop2.dep_fracTwo	Inlet and outlet Al ₂ O ₃ mass flow must be equal
		In element Loop2 : $Fl_I.getTotalComp("AL2O3(a)") = Fl_O.getTotalComp("AL2O3(a)")$
9.	Loop2.dep_SumFrac	Sum of mass fractions must equal 1
		In element Loop2 .Fl _ O : $getTotalComp("H2O") + getTotalComp("AL2O3(a)") + getTotalComp("H2") = 1$
10.	Loop2.dep_Tt	Inlet and outlet total temperature must be equal
		In element Loop2 : $Fl_I.Tt = Fl_O.Tt$

11.	Loop3.dep_W	Inlet and outlet mass flow must be equal
		In element Loop3 : $Fl_{I.W} = Fl_{O.W}$
12.	CombSteam_W	Steam and aluminum mass flow into pre-combustor must be equal
		$C1.Fl_{O.W} \cdot C1.Fl_{O.getTotalComp}("H2O") =$ $Seed1.Fl_{O.W} \cdot \frac{k_{Seed}}{k_{Seed} + 1}$
13.	CombSteam_T	Steam flow into pre-combustor must match target temperature value
		$C1.Fl_{O.Tt} = Target$
14.	HEhot_T	Water flow out of the heat exchanger must match target temperature
		$HE1.Fl_{O.2.Tt} = Target$
15.	SOFC1.Cathode_i	Actual cathode current must equal value calculated from Eq. 2-50
		In element SOFC1: $iCalcCathode = iDens + iDensInternal$
16.	SOFC1.Anode_i	Actual anode current must equal value calculated from Eq. 2-46
		In element SOFC1: $iCalcAnode = iDens + iDensInternal$
17.	SOFC1.FC_ht	Energy conservation in terms of power output and enthalpy in/out
		In element SOFC1: $iTotal \cdot cellVoltOper =$ $(h_{anO} + h_{catO} - h_{anI} - h_{catI}) + qLoss$
The following conditions are used (one at a time only) if fuel flow is varied as an independent. (see Independents list)		
18.	Power0	Net power (not including any H ₂ compression)
		$SOFC1.pElec + T1.pwr + C1.pwr + LP1.pwr$ $+ LP2.pwr + LP3.pwr = (Target\ Power)$
19.	Power2	Net power (including H ₂ seeding and storage compression)
		$SOFC1.pElec + T1.pwr + C1.pwr + LP1.pwr + LP2.pwr$ $+ LP3.pwr + GasC1.pwr + GasC2.pwr = (Target\ Power)$
20.	Power4	Net power (including H ₂ seeding and venting compression)
		$SOFC1.pElec + T1.pwr + C1.pwr + LP1.pwr + LP2.pwr$ $+ LP3.pwr + GasC1.pwr + GasC3.pwr = (Target\ Power)$
21.	Power6	Net power (including only H ₂ venting compression)
		$SOFC1.pElec + T1.pwr + C1.pwr + LP1.pwr + LP2.pwr$ $+ LP3.pwr + GasC3.pwr = (Target\ Power)$

Appendix E:

NPSS Details of Aluminum-H₂O₂ Combustor Model

Order of Execution:

Turbine Path:

1. Loop Start element: MixLoop 'Loop1'
2. Separator element: Separator2 'Sep1'
3. Turbine element: Turbine 'T1'

Fuel Feed Path:

4. Flow Start element: FlowStart2 'F1'
5. Fuel Seeder element: Seeder 'Seed1'
6. Flow Start element: FlowStart2 'F5'
7. Flow Start element: FlowStart2 'F6'
8. Mixture Start element: MixStart 'MixS1'
9. Combustor type Bleed element: Bleed 'PreComb1'

Inlet-to-Combustor Path:

10. Loop Start element: MixStart 'Loop2'
11. Heat Exchanger element: HeatExchanger 'HE1'
12. Combustor type Bleed element: Bleed 'Comb1'

Water recycle loop:

13. Condenser type Bleed element: Bleed 'Cond1'
14. Separator element: Separator2 'Sep2'
15. Liquid Pump element: LiquidPump 'LP1'
16. Splitter element: Splitter2 'Split4'
17. Flow Start element: FlowStart2 'F8'
18. Water Mixer element: WaterMixer 'WMix1'

19. Liquid Pump element: LiquidPump 'LP2'

Hydrogen compression branch:

20. Compressor element: Compressor2 'GasC1'

Additional elements:

21. Shaft element: Shaft 'Sh1'

22. Flow End elements: FlowEnd 'E1', 'E4', 'E5'

Independents:

Complete list of independent variable varied by the system:

Table E-1: Aluminum-H₂O₂ Combustor system independent variables.

	Variable name	Description	Controlled parameter
1.	Loop1.ind_Pt	Loop1 Exit total pressure, Pt	Loop1.Fl_O.Pt
2.	Loop1.ind_Tt	Loop1 Exit total temp., Tt	Loop1.Fl_O.Tt
3.	Loop1.ind_W	Loop1 Exit mass flow, \dot{m}	Loop1.Fl_O.W
4.	Loop1.ind_fracOne	Loop1 Exit mass fraction, y_1	Loop1.Fl_O.getTotalComp("H2O")
5.	Loop1.ind_fracTwo	Loop1 Exit mass fraction, y_2	Loop1.Fl_O.getTotalComp("H2")
6.	Loop1.ind_fracThree	Loop1 Exit mass fraction, y_3	Loop1.Fl_O.getTotalComp("AL2O3(a)")
7.	Loop2.ind_fracOne	Loop2 Exit mass fraction, y_1	Loop2.Fl_O.getTotalComp("H2O(L)")
8.	Loop2.ind_fracTwo	Loop2 Exit mass fraction, y_2	Loop2.Fl_O.getTotalComp("AL2O3(a)")
9.	Loop2.ind_fracThree	Loop2 Exit mass fraction, y_3	Loop2.Fl_O.getTotalComp("H2")
10.	Cond_T	Cond1 Exit total temp., Tt	Cond1.Fl_O.Tt
11.	HeatEx_eff	HE1 Effectiveness, ϵ	HE1.eff
	The following variable is only used if a power output is specified by a dependent condition. (see Dependents list)		
12.	AL_W	F1 Exit mass flow, \dot{m}	F1.Fl_O.W - Indirectly controls Al flow

Dependents:

Complete list of dependent conditions required by the system solver:

Table E-2: Aluminum-H₂O₂ Combustor system dependent conditions.

Condition name		Condition description/equation
1.	Loop1.dep_Pt	Inlet and outlet total pressure must be equal
		In element Loop1 : $Fl_I.Pt = Fl_O.Pt$
2.	Loop1.dep_Tt	Inlet and outlet total temperature must be equal
		In element Loop1 : $Fl_I.Tt = Fl_O.Tt$
3.	Loop1.dep_W	Inlet and outlet mass flow must be equal
		In element Loop1 : $Fl_I.W = Fl_O.W$
4.	Loop1.dep_fracOne	Inlet and outlet H ₂ O mass flow must be equal
		In element Loop1 : $Fl_I.getTotalComp("H2O") = Fl_O.getTotalComp("H2O")$
5.	Loop1.dep_fracTwo	Inlet and outlet H ₂ mass flow must be equal
		In element Loop1 : $Fl_I.getTotalComp("H2") = Fl_O.getTotalComp("H2")$
6.	Loop1.dep_SumFrac	Sum of mass fractions must equal 1
		In element Loop1 .Fl _ O : $getTotalComp("H2O") + getTotalComp("H2") + getTotalComp("AL2O3(a)") = 1$
7.	Loop2.dep_fracOne	Inlet and outlet liquid H ₂ O mass flow must be equal
		In element Loop2 : $Fl_I.getTotalComp("H2O(L)") = Fl_O.getTotalComp("H2O(L)")$
8.	Loop2.dep_fracTwo	Inlet and outlet Al ₂ O ₃ mass flow must be equal
		In element Loop2 : $Fl_I.getTotalComp("AL2O3(a)") = Fl_O.getTotalComp("AL2O3(a)")$
9.	Loop2.dep_SumFrac	Sum of mass fractions must equal 1
		In element Loop2 .Fl _ O : $getTotalComp("H2O") + getTotalComp("AL2O3(a)") + getTotalComp("H2") = 1$
10.	Loop2.dep_Tt	Inlet and outlet total temperature must be equal
		In element Loop2 : $Fl_I.Tt = Fl_O.Tt$

11.	HEhot_T	Water flow out of the heat exchanger must match target temperature
		$HE1.Fl_O\ 2.Tt = \text{Target}$
The following conditions are used (one at a time only) if fuel flow is varied as an independent. (see Independents list)		
12.	Power0	Net power (not including any H ₂ compression)
		$T1.pwr + LP1.pwr + LP2.pwr = (\text{Target Power})$
13.	Power2	Net power (including H ₂ seeding and storage compression)
		$T1.pwr + LP1.pwr + LP2.pwr + GasCl.pwr = (\text{Target Power})$

Appendix F:

NPSS Details of Hydrocarbon Combustor Model

Order of Execution:

Turbine Path:

1. Loop Start element: MixLoop 'Loop1'
2. Turbine element: Turbine 'T1'

Fuel Feed Path:

3. Flow Start element: FlowStart2 'F9'
4. Flow Start element: FlowStart2 'F5'
5. Flow Start element: FlowStart2 'F6'
6. Mixture Start element: MixStart 'MixS1'
7. Combustor type Bleed element: Bleed 'PreComb1'

Inlet-to-Combustor Path:

8. Loop Start element: MixStart 'Loop2'
9. Heat Exchanger element: HeatExchanger 'HE1'
10. Combustor type Bleed element: Bleed 'Comb1'

Water recycle loop:

11. Condenser type Bleed element: Bleed 'Cond1'
12. Separator element: Separator2 'Sep2'
13. Liquid Pump element: LiquidPump 'LP1'
14. Splitter element: Splitter2 'Split4'
15. Flow Start element: FlowStart2 'F8'
16. Water Mixer element: WaterMixer 'WMix1'
17. Liquid Pump element: LiquidPump 'LP2'

CO₂ compression branch:

18. Flow Copy element: FlowCopy 'FC1'

19. Compressor element: Compressor2 'GasC2'

20. Compressor element: Compressor2 'GasC3'

Additional elements:

21. Shaft element: Shaft 'Sh1'

22. Flow End elements: FlowEnd 'E3', 'E5', 'E6'

Independents:

Complete list of independent variable varied by the system:

Table F-1: Hydrocarbon Fueled Combustor system independent variables.

	Variable name	Description	Controlled parameter
1.	Loop1.ind_Pt	Loop1 Exit total pressure, Pt	Loop1.Fl_O.Pt
2.	Loop1.ind_Tt	Loop1 Exit total temp., Tt	Loop1.Fl_O.Tt
3.	Loop1.ind_W	Loop1 Exit mass flow, \dot{m}	Loop1.Fl_O.W
4.	Loop1.ind_fracOne	Loop1 Exit mass fraction, y_1	Loop1.Fl_O.getTotalComp("H2O")
5.	Loop1.ind_fracTwo	Loop1 Exit mass fraction, y_2	Loop1.Fl_O.getTotalComp("CO2")
6.	Loop1.ind_fracThree	Loop1 Exit mass fraction, y_3	Loop1.Fl_O.getTotalComp("O2")
7.	Loop2.ind_fracOne	Loop2 Exit mass fraction, y_1	Loop2.Fl_O.getTotalComp("H2O(L)")
8.	Loop2.ind_fracTwo	Loop2 Exit mass fraction, y_2	Loop2.Fl_O.getTotalComp("CO2")
9.	Loop2.ind_fracThree	Loop2 Exit mass fraction, y_3	Loop2.Fl_O.getTotalComp("O2")
10.	Cond_T	Cond1 Exit total temp., Tt	Cond1.Fl_O.Tt
11.	HeatEx_eff	HE1 Effectiveness, ϵ	HE1.eff
The following variable is only used if a power output is specified by a dependent condition. (see Dependents list)			
12.	HC_W	F9 HC fuel mass flow, \dot{m}	F9.Fl_O.W

Dependents:

Complete list of dependent conditions required by the system solver:

Table F-2: Hydrocarbon Fueled Combustor system dependent conditions.

Condition name		Condition description/equation
1.	Loop1.dep_Pt	Inlet and outlet total pressure must be equal
		In element Loop1 : $Fl_I.Pt = Fl_O.Pt$
2.	Loop1.dep_Tt	Inlet and outlet total temperature must be equal
		In element Loop1 : $Fl_I.Tt = Fl_O.Tt$
3.	Loop1.dep_W	Inlet and outlet mass flow must be equal
		In element Loop1 : $Fl_I.W = Fl_O.W$
4.	Loop1.dep_fracOne	Inlet and outlet H ₂ O mass flow must be equal
		In element Loop1 : $Fl_I.getTo talComp (" H2O") = Fl_O.getTotal Comp (" H2O")$
5.	Loop1.dep_fracTwo	Inlet and outlet H ₂ mass flow must be equal
		In element Loop1 : $Fl_I.getTo talComp (" H2") = Fl_O.getTotal Comp (" H2")$
6.	Loop1.dep_SumFrac	Sum of mass fractions must equal 1
		In element Loop1 .Fl _ O : $getTotalComp("H2O") + getTotalComp("H2")$ $+ getTotalComp("AL2O3(a)") = 1$
7.	Loop2.dep_fracOne	Inlet and outlet liquid H ₂ O mass flow must be equal
		In element Loop2 : $Fl_I.getTtalComp("H2O(L)") =$ $Fl_O.getTotaComp("H2O(L)")$
8.	Loop2.dep_fracTwo	Inlet and outlet Al ₂ O ₃ mass flow must be equal
		In element Loop2 : $Fl_I.getTo talComp (" AL2O3(a)") =$ $Fl_O.getTotal Comp (" AL2O3(a)")$
9.	Loop2.dep_SumFrac	Sum of mass fractions must equal 1
		In element Loop2 .Fl _ O : $getTotalComp("H2O") + getTotalComp("AL2O3(a)")$ $+ getTotalComp("H2") = 1$
10.	Loop2.dep_Tt	Inlet and outlet total temperature must be equal
		In element Loop2 : $Fl_I.Tt = Fl_O.Tt$

11.	HEhot_T	Water flow out of the heat exchanger must match target temperature
		HE1 .Fl_O 2.Tt = Target
The following conditions are used (one at a time only) if fuel flow is varied as an independent. (see Independents list)		
12.	Power0	Net power (not including any CO ₂ compression)
		T1.pwr + LP1.pwr + LP2.pwr = (Target Power)
13.	Power2	Net power (including storage compression)
		T1.pwr + LP1.pwr + LP2.pwr + GasC 2.pwr = (Target Power)
14.	Power4	Net power (including venting compression)
		T1.pwr + LP1.pwr + LP 2.pwr + GasC 3.pwr = (Target Power)

Bibliography

1. "The Navy unmanned undersea vehicle (UUV) master plan," Department of the Navy Publication, 2004.
2. **Eagle, W.E.** "Modeling of a high energy density propulsion system based on the combustion of aluminum and steam," M.S. Thesis, University of Maryland, 2007.
3. **Greiner, L.** *Underwater missile propulsion*. Arlington, VA : Compass Publications, 1967.
4. *GlobalSecurity.org*. [Online] [Cited: April 4, 2011.]
<http://www.globalsecurity.org/military/library/budget/fy2001/dote/navy/01mk48adcap.html>.
5. **Lakemana, J.B., Rose, A., Pointon, K.D., Browning, D.J., Lovell, K.V., Waring, S.C., Horsfall, J.A.** "The direct borohydride fuel cell for UUV propulsion power," *Journal of Power Sources*, Vol.162, 2006, pp.765-772.
6. **Herr, J., Lowery, B., Kiely, D., Klanchar, M., Holmberg, W., Cawley, T.** "Aluminum combustion power system: System status and highlights," Powerpoint via E-mail correspondence, 2006.
7. *NAVSEA.Navy.mil*. [Online] [Cited: April 4, 2011.]
<http://www.navsea.navy.mil/nuwc/newport/auvd/Pages/MARV%20-%20Mid-Sized%20Autonomous%20Reconfigurable%20Vehicle.aspx>.
8. **Roy, G.** *Advances in chemical propulsion: Science to technology*. Boca Raton, FL : CRC Press, 2001.
9. **Eagle, W.E., Waters, D., Cadou, C.P.** "System modeling of a novel aluminum fueled UUV power system," to be published, 2011.
10. **Miller, T.F., Walter, J.L., Kiely, D.H.** "A next generation AUV energy system based on aluminum-seawater combustion," Workshop on Autonomous Underwater Vehicles, June 20-21, 2002.
11. **Fricke, H.D., Burr, J.W., Sobieniak, M.G.** "Fluidized powders - A new approach to storable missile fuels," 12th JANNAF Liquid Propulsion Meeting, 1970.
12. **Foote, J.P., Lineberry, J.T., Thompson, B.R., Winkelman, B.C.** "Investigation of aluminum particle combustion for underwater propulsion," 32nd Joint Propulsion Conference and Exhibit, Lake Buena Vista, FL. July 1-3, 1996.
13. **Swihart, M.T., Catoire, L.** "Thermochemistry of aluminum species for combustion modeling from Ab Initio molecular orbital calculations," *Combustion and Flame*, Vol.121, 2000, pp.210-222.
14. **Hopson, C.B.** "Space shuttle solid rocket motor slag expulsion mechanisms," 31st Joint Propulsion Conference, San Diego, CA. July 10-12, 2005.
15. **Kiely, D.H.** "Review of underwater thermal propulsion," 30th Joint Propulsion Conference, Indianapolis, IN. June 27, 1994.
16. **Hamilton-Sunstrand.** "Aluminum combustor systems analysis open vs closed cycle," E-mail correspondence with Joe Fontaine, 2006.
17. **Haynes, W.M., Lide, D.R., eds.** *CRC Handbook of Chemistry and Physics, 91st Edition*. Internet version, <http://www.hbcnpnetbase.com> : CRC Press, 2011.
18. **Li, Xianguo.** *Principles of Fuel Cells*. New York : Taylor & Francis Group, 2006.

19. **Kee, R.J., Zhu, H., Sukeshini, A.M., Jackson, G.S.** "Solid oxide fuel cells: Operating principles, current challenges, and the role of syngas," *Combustion Science & Technology*, Vol.180, No.6, 2008, pp.1207-1244.
20. **Steele, B.C.H., Heinzl, A.** "Materials for fuel-cell technologies," *Nature*, Vol.414, 2001, pp.345-352.
21. DOE (1994) "Handbook of methods for the analysis of the various parameters of the carbon dioxide system in sea water; version 2," A.G.Dickson & C.Goyet, eds., ORNL/CDIAC-74.
22. **Tremblay, J.P., Gemmen, R.S., and Bayless, D.J.** "The effect of coal syngas containing HCl on the performance of solid oxide fuel cells: Investigations into the effect of operational temperature and HCl concentration," *Journal of Power Sources*, Vol.169, 2007, pp.347-354.
23. **Mohtadi, R., Lee, W.K., Van Zee, J.W.** "Assessing durability of cathodes exposed to common air impurities," *Journal of Power Sources*, Vol.138, 2004, pp.216-225.
24. **McLean, G.F., Niet, T., Prince-Richard, S., Djilali, N.** "An assessment of alkaline fuel cell technology," *International Journal of Hydrogen Energy*, Vol.27, No.5, 2002, pp. 507-526.
25. **Smitha, B., Sridhar, S., Khan, A.A.** "Solid polymer electrolyte membranes for fuel cell applications -- a review," *Journal of Membrane Science*, Vol.259, 2005, pp.10-26.
26. **Hu, J.E., Pearlman, J.B., Jackson, G.S., Tesluk, C.J.** "Evaluating the impact of enhanced anode CO tolerance on performance of proton-exchange-membrane fuel cell systems fueled by liquid hydrocarbons," *Journal of Power Sources*, Vol.195, 2010, pp.1926-1935.
27. "NPSS user guide, software release 1.6.5," NASA Publication, 2008.
28. **McBride, B., Gordon, S.** "Computer Program for Calculation of Complex Chemical Equilibrium Compositions and Applications II. User's Manual and Program Description," NASA Publication RP-1311-P2, 1996.
29. **Wendt, J.F. (Ed.).** *Computational Fluid Dynamics, 3rd Edition*. Berlin : Springer, 2009.
30. **Pratt, J.** , NPSS modeling, University of California-Irvine National Fuel Cell Research Center, via E-mail correspondence with Tom Lavelle, 2008.
31. **Zhu, H., Kee, R.J.** "A general mathematical model for analyzing the performance of fuel-cell membrane-electrode assemblies," *Journal of Power Sources*, Vol.117, 2003, pp.61-74.
32. **Zhu, H., Kee, R.J.** "The influence of current collection on the performance of tubular anode-supported SOFC cells," *Journal of Power Sources*, Vol.169, 2007, pp.315-326.
33. **Zhu, H., Kee, R.J., Janardhanan, V.M., Deutschmann, O., Goodwin, D.G.** "Modeling elementary heterogeneous chemistry and electrochemistry in solid-oxide fuel cells," *Journal of the Electrochemical Society*, Vol.152, No.12, 2005, pp.A2427-A2440.
34. **Flack, R.D.** *Fundamentals of Jet Propulsion with Applications*. NY : Cambridge University Press, 2005.
35. **Gaskell, D.R.** *Introduction to the thermodynamics of materials, 4th ed.* NY : Taylor & Francis, 2003.
36. **O'Connell, J.P., Haile, J.M.** *Thermodynamics: Fundamentals for applications*. New York : Cambridge University Press, 2005.
37. **Raymer, D.P.** *Aircraft design: A conceptual approach*. Reston, VA : AIAA, 2006.

38. **Burke, A.A., Carreiro, L.G.** "System modeling of an air-independent solid oxide fuel cell system for unmanned undersea vehicles," *Journal of Power Sources*, Vol.158, 2006, pp.428-435.
39. **Kee, R.J., Zhu, H., and Goodwin, D.G.** "Solid oxide fuel cells with hydrocarbon fuels," *Proceedings of the Combustion Institute*, Vol.30, 2005, pp.2379-2404.
40. **Carapezza, E.** "Aluminum combustion program," Powerpoint via E-mail correspondence, 2006.
41. **Gitzendanner, R., Puglia, F., Martin, C., Carmen, D., Jones, E., Eaves, S.** "High power and high energy lithium-ion batteries for under-water applications," *Journal of Power Sources*, Vol.136, 2004, pp.416-418.